UNIVERSITY OF OKLAHOMA

GRADUATE COLLEGE

QUANTITATIVE SEISMIC INTERPRETATION AND MACHINE LEARNING

APPLICATIONS FOR SUBSURFACE CHARACTERIZATION AND MODELING

A DISSERTATION

SUBMITTED TO THE GRADUATE FACULTY

in partial fulfillment of the requirements for the

Degree of

DOCTOR OF PHILOSOPHY

By

ABIDIN BERK CAF
Norman, Oklahoma
2022

QUANTITATIVE SEISMIC INTERPRETATION AND MACHINE LEARNING

APPLICATIONS FOR SUBSURFACE CHARACTERIZATION AND MODELING

A DISSERTATION APPROVED FOR THE

SCHOOL OF GEOSCIENCES

BY THE COMMITTEE CONSISTING OF

Dr. Matthew J. Pranter, Chair

Dr. Kurt J. Marfurt

Dr. Heather Bedle

Dr. Brett M. Carpenter

Dr. Chandra Rai

"If one day, my words are against science, choose science."

Mustafa Kemal Atatürk

Acknowledgments

Table of Contents

List of Figures

List of Tables

Abstract

Quantitative seismic interpretation and geostatistical modeling methods have been widely used for subsurface reservoir characterization. However, the task becomes challenging due to the reservoir complexity and limited well control. To address these challenges, this research explores workflows that combine supervised machine learning, quantitative seismic interpretation, and seismic-constraining reservoir modeling methods to effectively reduce uncertainty in predicting multiscale subsurface heterogeneity. These workflows help mitigate the risks and uncertainties of exploring and developing potential reservoirs for hydrocarbon exploration and production or subsurface carbon sequestration. Techniques applied in this study integrate multiple sources of data to characterize complex reservoirs across different fields in north America. This dissertation presents three case studies combining new and traditional subsurface characterization techniques at different scales. The research starts with supervised machine learning, 3D seismic data, and well-log information to map the seismic scale diagenetic imprint and its corresponding reservoir quality on a Permian Basin reservoir. Then, I present a workflow that integrates core-derived petrophysical measurements, well logs, and pre-stack seismic data through supervised machine learning to map the seismic-scale spatial variability of petrophysically significant facies of a carbonate reservoir targeted for carbon geosequestration. Lastly, I present a seismic-constrained reservoir modeling and simulation workflow that combines the seismic-scale petrophysically defined facies information with well log and core data to map small-scale stratigraphic variability of petrophysical properties, CO_2 storage capacity, and subsurface fluid flow behavior for long-term carbon sequestration. The illustrated workflows showed that the subsurface properties, such as lithology and petrofacies information, could be extracted on a seismic scale with the help of

supervised machine learning. Additionally, this information can be used to better constrain reservoir models and reduce uncertainty where the well control is sparse.

Introduction

The effective exploitation of hydrocarbons and safe storage of CO_2, natural gas, or other fluids requires a robust reservoir characterization. An optimal subsurface characterization is crucial for better assessment of reservoirs by reducing the risk and uncertainty, ultimately helping the world's ever-growing energy demand and reaching net-zero emissions to combat global climate change.

Traditional 3D seismic interpretation augmented by seismic attribute analysis that comprise the reservoir to define stratal geometries, structure, and stratigraphic features in a depositional environment (Chopra and Marfurt, 2007; Brown, 2011). Quantitative seismic interpretation techniques such as impedance inversion, AVO, and rock physics modeling provide additional information and provide lithology, reservoir quality, and pore fluid content for siliciclastic reservoirs (Avseth et al., 2001; Chopra and Castagna, 2014). However, quantitative interpretation of carbonate reservoirs is complicated by complex pore systems (Wang, 1997), stiff rock matrices, and high interval velocities. (Palaz and Marfurt, 1997; Masaferro et al., 2004). Additionally, while seismic measures provide good lateral information, the vertical resolution is insufficient enough to evaluate small-scale heterogeneity and variability. To address this small-scale subsurface heterogeneity, multi-scale data from well logs, and core have been used to create reservoir models. Neuhaus et al. (2004) utilized abundant well control to create variograms and performed stochastic inversion and incorporated the results as input for further reservoir modeling. Pranter et al. (2004) demonstrated an integrated approach to identify heterogeneities within a complex Permian Basin carbonate reservoir. These studies commonly require good well control to

create robust, detailed geostatistical models. In this dissertation, I aim to utilize supervised machine learning workflows to provide more quantitative seismic interpretation results when there is limited well control. I will also explore workflows that integrate seismic-based property volumes with core and well log information to further constrain reservoir models for a robust reservoir characterization.

In Chapter 1, I use a combination of post-stack seismic inversion, probabilistic neural network (PNN), and supervised Bayesian classification to map the lithology variation and reservoir quality controlled by the regional reflux dolomitization in the Midland Basin Leonardian and Wichita formations.

In Chapter 2, I define core-derived petrophysics-based rock types (petrofacies) and create seismic elastic property volumes using pre-stack simultaneous inversion to train a supervised random forest classifier for seismic-scale prediction of 3D petrofacies and individual petrofacies probability volumes. Then, I evaluate results for seismic-scale assessment of CO_2 injectivity and storage potential of the Arbuckle Group in Wellington Field in southern Kansas.

In Chapter 3, I use the seismic-scale petrofacies and probability volumes from Chapter 2 and combine that information with well log information for seismic-constrained reservoir modeling to model detailed stratigraphic and spatial variability of petrofacies and corresponding petrophysical properties. I then select these models to evaluate hypothesized CO_2 plume during long-term injection and post-injection periods using dynamic simulations. Finally, in the last chapter, I summarize the main conclusions based on the results from previous chapters in the dissertation.

References

Avseth, P., T. Mukerji, A. Jørstad, G. Mavko, and T. Veggeland, 2001, Seismic reservoir mapping from 3-D AVO in a North Sea turbidite system: Geophysics, 66, 1157–1176, doi: 10.1190/1.1487063.

Brown, A. R., 2011, Interpretation of three-dimensional seismic data, Society of Exploration Geophysicists, doi: 10.1306/M4271346.

Chopra, S., and K. J. Marfurt, 2007, Seismic Attributes for Prospect Identification and Reservoir Characterization, SEG Geophysical Development Series, 11.

Chopra, S., and J. P. Castagna, 2014, AVO. Soc. Of Exploration Geophysicists

Masaferro, J. L., R. Bourne, and J. C. Jauffred, 2004, Three-dimensional seismic visualization of carbonate reservoirs and structures, in Seismic imaging of carbonate reservoirs and systems: AAPG Memoir 81, p. 11–41.

Neuhaus, D., J. Borgomano, J.-C. Jauffred, C. Mercadier, S. Olotu, and J. Grötsch, 2004, Quantitative seismic reservoir characterization of an Oligocene–Miocene carbonate buildup: Malampaya field, Philippines, in Seismic imaging of carbonate reservoirs and systems: AAPG Memoir 81, p. 169–183.

Palaz, I. and Kurt J. Marfurt, 1997, Carbonate Seismology: An Overview, *Geophysical Developments Series*, No 6, Society of Exploration Geophysicists, doi: 10.1190/1.9781560802099.

Pranter, M. J., N. F. Hurley, and T. L. Davis, 2004, Sequence-stratigraphic, petrophysical, and multicomponent seismic analysis of a shelf-margin reservoir: San Andres Formation (Permian), Vacuum field, New Mexico, United States, in Seismic imaging of carbonate reservoirs and systems: AAPG Memoir 81, 59–89.

Wang, Z., 1997, Seismic properties of carbonate rocks, in I. Palaz and K. J. Marfurt, eds., Carbonate seismology: SEG Geophysical Developments Series No. 6, 29–52.

Chapter 1: Dolomitization geometry and reservoir quality from supervised Bayesian classification and probabilistic neural network: Midland Basin Leonardian Wichita and Clearfork Formations*

Abstract

Extensive dolomitization is prevalent in the platform and periplatform carbonates in the Lower-Middle Permian strata in the Midland and greater Permian Basin. Early workers have found that the platform and shelf-top carbonates were dolomitized, whereas slope and basinal carbonates remained calcitic, proposing a reflux dolomitization model as the possible diagenetic mechanism. More importantly, they underline that this dolomitization pattern controls the porosity and forms an updip seal. These studies are predominately conducted using well logs, cores, and outcrop analogs, and although exhibiting high resolution vertically, such determinations are laterally sparse. We have used supervised Bayesian classification and probabilistic neural networks (PNN) on a 3D seismic volume to create an estimation of the most probable distribution of dolomite and limestone within a subsurface 3D volume petrophysically constrained. Combining this lithologic information with porosity, we then illuminate the diagenetic effects on a seismic scale. We started our workflow by deriving lithology classifications from well-log crossplots of neutron porosity and acoustic impedance to determine the a priori proportions of the lithology and the probability density functions calculation for each lithology type. Then, we applied these probability distributions and a priori proportions to 3D seismic volumes of the acoustic impedance and predicted neutron porosity volume to create a lithology volume and probability volumes for each lithology type. The acoustic impedance volume was obtained by model-based poststack inversion, and the neutron porosity volume was obtained by the PNN. Our results best supported a regional reflux dolomitization model, in which the porosity increases from shelf to slope while the dolomitization decreases, but with sea-level forcing. With this study, we determined that diagenesis and the corresponding reservoir quality in these platforms and periplatform strata can

be directly imaged and mapped on a seismic scale by quantitative seismic interpretation and supervised classification methods.

Introduction

In comparison to siliciclastics, carbonate rocks make up only 30% of Phanerozoic sediments (Mackenzie and Morse, 1992) but account for more than half of the proven conventional hydrocarbon reserves (Burchette, 2012). Although carbonates differ from clastic rocks by depositional environments with carbonates being allochthonous and autochthonous and clastics being allochthonous carbonates are most impacted by syn- and postdepositional diagenetic processes. These unique differences cause postdepositional reservoir heterogeneity and strongly control the resulting reservoir quality and ultimate recovery and make their exploration and production challenging. This investigation focuses on one specific problem that continues to haunt seismic carbonate exploration: "dolomitization." That is, can reflection seismic provide information that can create an informative lithofacies-diagenetic geometry, one that can provide a model or models for dolomitic porosity creation/destruction, and in doing so predict before the drill-bit local aspects of a reservoir's quality down to the bin size?

The Midland Basin and the associated shelf margins of the greater Permian Basin in West Texas and southeast New Mexico have been producing oil for more than 80 years and as such form the largest onshore petroleum-producing province in the United States.

The Leonardian stratigraphic section in the Midland Basin is approximately 2500–3000 ft (~750–900 m) thick and developed reservoirs at depths between 5600 and 7800 ft (~1700–2400 m) (Tyler et al., 1991). Leonardian reservoirs have been estimated to contain 14.5 Bbbl of original oil

7

in place, making up approximately 15% of the total conventional resource in the greater Permian Basin. However, the recovery efficiency of these reservoirs is the lowest in the Permian Basin (Dutton et al., 2004) owing to the prevalent dolomitization and the resulting highly heterogeneous distribution of reservoir quality. Consequently, understanding the diagenetic mechanism and the resulting distribution of reservoir quality is crucial.

Dolomitization stands for the mineralogical change from calcium carbonate (calcite) to calcium magnesium carbonate (dolomite). Conventional wisdom suggests that porosity increases when calcite is replaced stoichiometrically "mole-for-mole" to dolomite with an accompanying reduction in the volume of crystals (Weyl, 1960). However, this is not always the case as when the original structure is preserved and not disrupted (e.g., an ooid, a brachiopod, etc.) the transformation is clearly "volume for volume" (Folk, 1964). Indeed, the effect of dolomitization on porosity is not always an increase, but it can even become an impermeable barrier (Warren, 2000). Therefore, dolomitization is highly dependent upon the diagenetic mechanism and the stage of dolomitization (Land, 1985; Bebout et al., 1987; Major et al., 1988; Kerans et al., 1994; Lucia and Major, 1994; Sun, 1995).

Studies focused on Leonardian carbonates in the Midland Basin (Mazzullo and Reid 1989; Ye and Mazzullo, 1993; Mazzullo, 1994; Saller and Henderson, 1998; Saller, 2004, 2013) stated that extensive dolomitization is prevalent in the platform and periplatform carbonates in the Lower-Middle Permian strata in the Midland and greater Permian Basin. Furthermore, these studies pointed out that the platform and slope carbonates are almost entirely dolomitized and progressively transitioned into limestone distally.

Saller and Henderson (1998) and Saller (2004) suggest that dolomitization in Lower-Middle Permian carbonates is caused by hypersaline brines flowing from the platform interior toward the slope and basin, pointing out that the possible diagenetic mechanism is "reflux dolomitization" (Adams and Rhodes, 1960). They also conclude that this diagenetic pattern is the main control of the porosity, with the resulting porosity increase from the platform interior toward the platform margin and slope.

Almost all previous studies have focused on diagenetic mechanisms, and the distribution of reservoir quality of Lower-Middle Permian reservoirs was studied with an abundance of well logs, core, and outcrop analogs to create highly detailed geologic models. Though they exhibit high resolution vertically, the lateral resolution was limited, being highly dependent on well control. Therefore, in areas with sparse well control, interwell uncertainty is evident. This study aims to use the seismic information to bridge the gap between the wells and reduce the uncertainty where the well data are limited.

Supervised Bayesian classification has been used in various geoscience problems, especially for identifying pay zones from nonpay lithologies and petrophysics-based facies classifications (among others, Avseth et al., 2001; Sengupta and Bachrach, 2007; Nieto et al., 2013). These types of rock-physics-based lithology prediction workflows use the integration of well logs, inversion results, and seismic interpretation to provide a robust estimate of the most probable lithofacies and the uncertainties associated with the prediction by using a fully Bayesian approach.

For this study, a similar approach was adopted to predict the most probable volumes of limestone, dolomite, and shale to map dolomitization on a seismic scale. To combine the lithology

9

information with porosity, a probabilistic neural network (PNN) was used to predict total porosity, ultimately to reveal the effects of the diagenesis upon the reservoir quality in Leonardian carbonates at the Eastern Shelf of the Midland Basin.

Geologic setting

The Permian Basin is one of the largest sedimentary basins in North America. It spans an area of 6000 mi^2 and includes all or parts of 52 counties of West Texas and southeast New Mexico. Structurally, the Permian Basin is bounded on the south by the Marathon-Ouachita Fold Belt, on the west by the Diablo Platform and Pedernales Uplift, on the north by the Matador Arch, and on the east by the Eastern Shelf and the west flank of the Bend Arch (Ball, 1995).

The Midland Basin is located on the east side of the Permian Basin and is bounded by the Central Basin Platform on the west, by Eastern Shelf on the east, by the Ozona Arch and Ouachita-Marathon Fold Belt and the Matador Arch to the south and north, respectively (Ward et al., 1986). The Eastern Shelf lies west of the Bend Arch and Llano uplift and extends westward to the eastern edge of the Midland Basin. The northern limits are the Knox-Baylor Basin and the Matador Arch with the Val Verde Basin being the southern boundary.

The history of the Permian Basin can be subdivided into three distinct stages (Adams, 1965; Hills, 1985; Ward et al., 1986; Sarg et al., 1999). During Cambrian to Mississippian time, the ancestral Permian Basin, called the Tobosa Basin, is formed by weak crustal extension and low subsidence. The Tobosa Basin was filled by passive margin shallow marine carbonates and shales (Horak, 1985). During the Mid-to-Late Mississippian, the Tobosa Basin was divided by the formation of a central high, effectively initiating the formation of the Delaware Basin, Central

Basin Platform, and Midland Basin. From the Late Mississippian until the end of the Pennsylvanian, the Ouachita Orogeny fragmented the Tobosa Basin into a series of horsts and grabens along high-angle reverse faults (Hills, 1985; Horak, 1985). At this time, carbonate shelves began to form along the margins of the newly formed basins and were intermixed with siliciclastic sediment throughout the filling of the basins (Flamm, 2008). The Middle Permian to the early Triassic interval was characterized by relative tectonic stability and rapid subsidence during which most of the subbasins within the Permian Basin were filled (Flamm, 2008). As the Delaware and Midland Basins subsided, the central basin platform continued to rise several thousand feet (Horak, 1985). Since the beginning of the Triassic, the Permian Basin has been tilted to the east as the western edge of the basin was uplifted approximately 9000 ft (2743 m), half of which is the result of uplifting during the Laramide orogeny (Horak, 1985). In the Late Permian, the basin became restricted from the sea by the possible closure of the Hovie Channel and the evaporates deposited.

The study area is located in Scurry County, Texas, along the eastern shelf of the Midland Basin (Figure 1.1). The regional stratigraphy of the study area comprises units from Ordovician to Permian age. The primary target unit of petroleum exploration of the study area is the Late Pennsylvanian to Early Permian-aged Horseshoe Atoll reefal buildup.

The interval of interest in this study is the Leonardian-aged Wichita and Clear Fork Formations (Figure 1.2). Rocks made up the Leonardian strata consist of vertically stacked, progradational, and aggradational platform-to-basin sequences dominated by dolomite, limestone, and shales. These rocks were cyclic alterations of peritidal, tidal-flat deposits and subtidal carbonates deposited in shallow-water, restricted, low-energy platforms in an arid climatic setting (Presley, 1987; Ruppel, 1992; Ye and Mazzullo, 1993; Atchley et al., 1999).

11

The progradational nature of the Leonardian strata in the study area is characterized by abrupt stratigraphic discontinuities, detrital carbonates, and distinct clinoformal geometries (Hamlin and Baumgardner, 2013). Seismic stratigraphic interpretation of the Leonardian section reveals shelf progradation dominated by clinoformal features divided by seismic parasequence boundaries. These parasequence boundaries reflect the relative sea-level cyclicity, with a series of alternating lowstand and highstands (Figure 1.3).

Available Data

For this study, a prestack time-migrated, and common-depth point stacked 3D seismic survey was used. The seismic survey was acquired with a vibroseis with a sweep of 8–90 Hz, a 2 ms sample rate, and processed with a bin size of 82.5×82.5 ft (25×25 m). The survey consists of 442 inlines and 418 crosslines, and a record length of 3 s. The approximate area of the seismic survey is 25 mi^2 (approximately 65 km^2). The vertical resolution (equals to one-fourth) of a wavelength of seismic data is 100 ft (approximately 30 m).

Along with the seismic survey, seven wells were selected for this study. These wells were selected based on the log quality and depth penetration of interest. A suite of conventional wireline logs includes gamma ray, caliper, shallow and deep resistivity, neutron porosity, density, sonic, and photoelectric factor logs. Neutron porosity and gamma-ray logs were normalized to eliminate the differences in measurement caused by different logging tools and operators. Synthetic seismograms were also generated to tie these wells to seismic.

Methods

The workflow followed for this study is illustrated in Figure 1.4. The approach to the problem starts with deriving lithology classifications from well-log crossplots, which will define the "a priori" proportions of the lithologies and with creating probability density functions (PDFs) to define the likelihood of each lithology in the attribute space. Once the prior lithology proportions and their probabilities within the seismic volumes were defined, the last step was to apply these to full inversion volumes to generate probability volumes for each lithology and the most probable lithology volume (Coulon et al., 2006; Doyen, 2006; Nieto et al., 2013). Seismic volumes needed to train the Bayesian classification and create the lithology classification (acoustic impedance and neutron porosity volumes) were derived from post stack acoustic impedance inversion and the PNN. Finally, the resulting lithology volume was combined with the total porosity volume to combine the lithology with the porosity information.

Supervised Bayesian classification for lithology prediction

Supervised Bayesian classification (Doyen, 2006; Grana, 2013; Nieto et al., 2013) uses well logs and a set of seismic attributes to provide an estimate of the most probable lithology and uncertainties associated with predicted lithology class. This method is based on Bayes' theorem, which can be expressed as:

$$p(c_i|X) = \frac{p(X|c_i) * p(C_i)}{p(X)} \tag{1}$$

where c_i represents the ith lithology (e.g., dolomite, limestone, or shale), X is the seismic attribute vector (crossplot of the attribute pairs), and $p(C_i)$ is the prior probability for

lithology ci (e.g., the probability of limestone in general). Importantly, a principal assumption is that the probabilistic occurrences of these lithology classes are independent of each other. But because of the mixing of mineralogies (e.g., calcite to magnesian calcite to dolomite) or of difficulties in discretizing their detection, as a first approximation, one states that $p(X|c_i)$ is the probability of attribute set X with the knowledge that the class is c_i (distribution of limestone in the attribute crossplot space). This is also called the "likelihood function." The term $p(X)$ is the probability of attribute vector X. For the lithology prediction workflow used, $p(C_i)$ is the input created by the user (lithology or petrofacies logs) and $p(X|c_i)$ is computed from PDFs.

As the first step in this lithology prediction method to map the dolomitization in the study area, lithology logs were created. This task can be achieved by applying discrete cutoff values to wireline logs for each lithology type. This can be achieved by defining clusters for each lithology type in the well-log crossplots. However, and with bearing upon the assumption of the validity of the independence of the classes, it must be noted that true lithology and facies information can only be determined from cores or cuttings (Nieto et al., 2013). Fortunately, among various attempts to create lithology classifications using different well-log pairs, the neutron porosity and acoustic impedance crossplot yielded the highest cluster separation between limestone, dolomite, and shale and is therefore used to create lithology logs. Figure 1.5 shows the crossplot between acoustic impedance and neutron porosity logs, color-coded by the photoelectric factor for well 6. Although limestone and dolomite have a similar range of acoustic impedance, the neutron porosity values help to distinguish the two lithology types as two independent classes. Furthermore, values assigned as shale can easily be distinguished in the crossplot by having low acoustic impedance

values and the highest neutron porosity values. The results of this method were also compared to "quick-look" lithology results to ensure the validity of the classifications (Figure 1.6).

After defining prior proportions of lithology by creating crossplot lithology logs, the next step was to define the "likelihood" of each lithology for the given sample within the attribute space. This can be done by calculating PDFs. PDFs can be built by convolving the data point in the crossplot with an operator (Nieto et al., 2013). PDFs provide the likelihood of each lithology for the given point in our crossplot space. A 2D PDF can be expressed as (after Grana, 2013):

$$PDF(x, y) = \frac{1}{nh} \sum_{i=1}^{n} K\left(\frac{x - x_i}{h_x}\right) K\left(\frac{y - y_i}{h_y}\right) \tag{2}$$

where x_i, y_i represent the observed values of attributes in the crossplot space, h is the smoothing operator defined by the interpreter, and K is the kernel operator.

The kernel operator in the commercial software package used in this study uses the Epanechnikov kernel (Doyen, 2006), which can be defined as:

$$K(x) = \begin{cases} \dfrac{3}{4} * (1 + x^2), \; for \; -1 \leq x \leq 1, \\ 0 \hspace{2.5cm} otherwise. \end{cases} \tag{3}$$

Figure 1.7 shows the PDFs computed from the upscaled lithology logs. Contours at each cluster represent the probability density value of samples belonging to a particular lithology. In other words, centers of each cluster would have a 100% probability of being limestone, dolomite,

or shale, whereas probabilities decrease away from centers and reach 0% on the outermost contour. This construct provides a measure of confidence in lithology classification by handling uncertainties associated with the overlaps between lithology classes in the attribute crossplot space.

To train the supervised Bayesian classification and predict the 3D volume of lithology, a supervised Bayesian classification workflow requires the same type of input attribute set that is used to create the lithology logs. Therefore, 3D volumes of acoustic impedance and neutron porosity are needed because lithology logs were derived from crossplotting neutron porosity and acoustic impedance logs. The acoustic impedance volume is obtained by poststack inversion, and a neutron porosity volume is subsequently predicted via PNN.

Post-stack inversion for acoustic impedance

Unlike seismic amplitude, which measures relative changes in rock properties, seismic inversion is directly correlated to the rock properties of each layer such as lithology and porosity (Swisi, 2009). Impedance is defined as the product of the intrinsic properties of rock such as the P-wave velocity and density. Seismic inversion can be defined as a process that creates "broadband" acoustic impedance values of the earth from the seismic reflection volumes. Besides being a lithology and porosity indicator, one of the other benefits of inversion can be an increase in seismic resolution (Veeken and Da Silva, 2004). Additionally, the inverted data can have more accurate thickness determination estimates below the tuning thickness and may even increase the accuracy above tuning (Hill, 2005). For this lithology classification study, the required acoustic impedance was created by "model-based" poststack inversion. This method requires an initial geologic model to be built by using interpreted horizons and low frequency filtered impedance logs to constrain the band limit and the distribution of acoustic impedance. This model is built by

extrapolating the filtered impedance logs throughout the volume using the seismic horizons. The extrapolation is done by weighting the log values inversely proportional to the square of the distance from wells. Next, a synthetic trace is generated by convolving the model values with a wavelet and it is then compared with the equivalent seismic trace. If the difference is small, the model trace is taken as the final solution. If the model trace differs significantly from the equivalent seismic trace, the impedance model is perturbed iteratively until the error between synthetic generated from the perturbed model and the original seismic trace reaches a minimum (Russell, 2004; Veeken and Da Silva, 2004). Figure 1.8 shows the results of the inversion process from arbitrary lines through wells 2 and 3. The impedance values can be observed to decrease from the platform interior (well 3) to the slope (well 2).

PNN for NPHI and total porosity volume prediction

The second component required for the Bayesian lithology classification is the neutron porosity (NPHI) volume. To predict the 3D volume of neutron porosity, the PNN method (Masters, 1995; Specht, 1995; Hampson et al., 2001) is used. This method combines a set of seismic attributes and a target log (neutron porosity) to predict a 3D volume of neutron porosity. Neural networks can enable seismic data to be related to porosity without explicitly defining parameters such as water content, lithology, or pore pressure. Additionally, neural networks can incorporate an interval of seismic data rather than a single sample value to predict porosity values (Himmer and Link, 1997). The procedure of neural network porosity prediction performed in this study can be divided into three steps (Figure 1.4) (Hampson et al., 2001; Verma et al., 2016).

The first step is to define the input attributes and the appropriate convolutional operator (or operator length) that controls how many neighboring samples of seismic attributes are to be related

17

to each sample in the target log. The objective of the first step is to derive a linear multiattribute transform between a subset of attributes and the target log values (in this case, neutron porosity), defined by the convolutional operator. The decision of valid operator length choice is important owing to differences in frequency between the target logs and the seismic data. An optimum set of attributes and convolutional operator length would yield a minimum validation error. Extending the operator length is equivalent to adding attributes at adjacent stratal slices to the stepwise linear regression workflow, increasing the chances for Kalkomey's (1997) false-positive correlation or as what is often termed "overtraining." Figure 1.9 shows the training and validation errors plotted against the number of attributes. Table 1 shows the training and validation errors of the corresponding attributes. Note that using more than four attributes decreased the training error while causing the validation error to increase. Therefore, the four attributes used in the training were colored inversion with added background model, envelope, relative acoustic impedance, and average frequency.

The second step in the process is to train the PNN with the given set of attributes and a specified operator length. This process produces nonlinear regression between a set of attributes and the target log.

After training the neural network, the final step is the application of the trained neural network to generate the 3D volume of neutron porosity and validate the results. For this study, six wells are used for neural network training, whereas one "blind" well that was not used in the training is used for validation. Figure 1.10 reveals the validation result from the blind well and the crossplot between the predicted neutron porosity from the neural network and the actual neutron porosity from the well logs. The correlation is 85%. Figure 1.11 shows the resulting predicted

18

neutron porosity values extracted along an arbitrary line passing through well 6. To investigate the dolomitization and the associated reservoir quality in the study area, the total porosity volume was also estimated using the same approach. The total porosity logs were calculated by using neutron and density porosity logs with the given formula:

$$\emptyset_{total} = \sqrt{\frac{\emptyset_{neutron}^2 + \emptyset_{density}^2}{2}} \tag{4}$$

The predicted total porosity volume will subsequently be used together with the lithology volume to investigate the effect of the dolomitization on reservoir quality. Figure 1.12 shows the optimum number of attributes used for neural network training. These attributes are the acoustic impedance volume from poststack inversion, the quadrature trace (the Hilbert-transformed seismic volume), 0/10–50/60 Hz, and the band-pass-filtered seismic volume. Table 2 shows the corresponding training and validation errors for these attributes. The training and validation of the neural network can be seen in Figure 1.13. The validation correlation is 81%. The result of the predicted total porosity volume is displayed in an arbitrary vertical slice through well 6 (Figure 1.14).

Application and quality control of the Bayesian lithology classification

With all the necessary components available, the supervised Bayesian classification was trained and applied to create a lithology volume and associated uncertainties with the classification. This part of the workflow uses the upscaled a priori lithology proportions from lithology logs and PDFs that are generated earlier.

19

To quality control (QC) the lithology classification results, and to evaluate the principal assumption of independence of classes, a confusion matrix was created (Table 1.3). The confusion matrix shows the match between the actual lithology from well logs and the predicted lithology class. The diagonal elements of the matrix show the accuracy of the classification, whereas the off-diagonal elements quantify the misclassification or "confusion" of classification with other lithology classes. For example, limestone was correctly classified as limestone 83% of the time and misclassified (confused) as dolomite 11% of the time.

After training and QC, supervised Bayesian classification was applied to inverted volumes of acoustic impedance and neutron porosity to generate the volume of most probable lithology and probabilities of each lithology class. Figure 1.15 shows the results of the supervised Bayesian classification results at an arbitrary line through well 6. Output volumes obtained from the supervised Bayesian classification are the probability volumes of limestone, dolomite, shale, and the most probable lithology volumes. Probability volumes are helpful by providing a measure of confidence for the lithology classification. Additionally, this information can also be useful as a possible indicator of areas where there is a mixture of lithology.

Results and discussion

The most probable lithology volume and associated probability volumes were interpreted together with the predicted total porosity volume to assess the diagenetic mechanism, spatial distribution of the lithology, and its associated reservoir quality in the study area. It must be noted that the predicted total porosity volume was derived from porosity logs that were not corrected for

the clay-bound water. Therefore, the predicted porosity values are possibly overestimated for the intervals with a high shale content.

East–west arbitrary cross sections taken from lithology and total porosity volumes (Figure 1.16) indicate that the platform interior is mainly dolomite with very low porosity, whereas the platform margin and slope are limestone with the porosity increasing basinward. The same outputs were also extracted on the seismic sequence boundary SS3 surface (Figure 1.17). The results indicate that the probability of limestone and total porosity increases from the shelf interior to the slope whereas the dolomite probability decreases. This observation might suggest that the degree of dolomitization is decreasing from the shelf interior to the slope. However, upon closer examination, these results complicate a single diagenetic mechanism for Lower to Middle Leonardian carbonates on the Midland Basin periplatform.

As a first-order observation, the probabilities of limestone and dolomite in Figures 1.15 to 1.17 are antithetic. In general, the limestone probabilities are highest in the periplatform and the lowest on the platform and dolomites exhibit higher probabilities on the platform and lower on the periplatform. As mentioned earlier, the reflux dolomitization mechanism would be consistent with dense hypersaline brines in restricted lagoons and tidal flats on the shelf refluxing toward the basin and would provide for the most dolomite precipitation to occur in the proximal parts of the system (the shelf). If massive, this would cause the most porosity occlusion to accompany the highest dolomitization on the shelf. According to the model, the continuation of refluxing brines with decreasing dolomite saturation results in gradually less dolomite replacement and increasing porosity toward the slope and basin (Saller and Henderson, 1998; Jones and Xiao, 2005; Figure 1.18).

However, the geometries of the limestones and dolostones shown in Figures 15–17 offer complications to a singular model of dolomitization. For example, the observed periplatform dolomite and limestones show alternating "stringer"-like features.

One possible observation is that during lowstands, the limestones dominate and during highstands, the dolomites are not only on the platform but then appear to prograde out on the periplatform as stringers. Such geometries strongly suggest a sea-level forcing of dolomitization occurrence (Vahrenkamp et al., 1991) and at least two possible mechanisms for dolomite periplatform dispersal. An alternative is that, during highstands with an elevated hydrologic head, dolomites would form on the periplatform through the mixing of freshwaters with marine waters (Austin and Pigott, 2007) but during lowstands, the previously deposited dolomite is transported detritally (Wiggins and Harris, 1985). Petrographic analysis of cores and cuttings from wells penetrating the Lower Clear Fork platform and periplatform by Landreth (1977) confirms the geometry presented by this seismic of tight dolostones on the shelf and less dolomite and greater porosity on the slope. Landreth (1977) even goes on to suggest that the alternating diagenetic trends seen on the periplatform might have been related to eustatic fluctuations. In any case, the reflux model better explains the platform dolomitization and only with future integrated petrography with isotopic analysis could one discern better the paragenesis and appropriate model or models for these dolomite occurrences.

Conclusions

Integration of supervised Bayesian classification and PNN study in the Midland Basin demonstrates that the dolomitization and corresponding reservoir quality can be extracted from seismic data with sparse well control. Additionally, when combined with the seismic stratigraphic

analysis, the results generally support a regional reflux dolomitization model on the platform, in which the porosity is increasing from the shelf to the slope concomitant with dolomitization decreasing and on the periplatform responding to variations in sea level.

Acknowledgments

References

Adams, E. A., and M. L. Rhodes, 1960, Dolomitization by seepage refluxion: AAPG Bulletin, 44, 1912–1920, doi: /10.1306/0BDA6263-16BD-11D7-8645000102C1865D.

Adams, J. E., 1965, Stratigraphic-tectonic development of Delaware Basin: AAPG Bulletin, 49, 2140–2148, doi: 10.1306/A6633888-16C0-11D7-8645000102C1865D.

Atchley, S. C., M. G. Kozar, and L. A. Yose, 1999, A predictive model for reservoir characterization in the Permian (Leonardian) Clear Fork and Glorieta Formations, Robertson Field area, west Texas: AAPG Bulletin, 83, 1031–1056, doi: 10.1306/E4FD2E65-1732-11D7-8645000102C1865D.

Austin, S. E., and J. D. Pigott, 2007, Eustatic sea level-influenced heterogeneous dolomitization of the Hope Gate Formation, Discovery Bay, Jamaica: GSA Denver Annual Meeting Paper No. 54-11.

Avseth, P., T. Mukerji, A. Jørstad, G. Mavko, and T. Veggeland, 2001, Seismic reservoir mapping from 3-D AVO in a North Sea turbidite system: Geophysics, 66, 1157–1176, doi: 10.1190/1.1487063.

Ball, M., 1995, Permian Basin Province (044), in D. L. Gautier, G. I. Dolton, K. T. Takahashi, and K. L. Varnes, eds., National assessment of United States oil and gas resources: Results, methodology, and supporting data: U.S. Geological Survey, U.S. Geological Survey Digital Data Series DDS-30.

Bebout, D. G., F. J. Lucia, C. R. Hocott, G. E. Fogg, and G. W. Vander Stoep, 1987, Characterization of the Grayburg reservoir, University Lands Dune field, Crane County, Texas: The University of Texas at Austin, Bureau of Economic Geology Report of Investigations, No. 168.

Burchette, T. P., 2012, Carbonate rocks and petroleum reservoirs: A geological perspective from the industry: Geological Society, London, Special Publications.

Coulon, J.-P., Y. Lafet, B. Deschizeaux, P. M. Doyen, and P. Duboz, 2006, Stratigraphic elastic inversion for seismic lithology discrimination in a turbidite reservoir: 76th Annual International Meeting, SEG, Expanded Abstracts, 2092–2096, doi: 10.1190/1.2369949.

Doyen, P. M., 2006, Seismic reservoir characterization: An earth modelling perspective: EAGE Publications B.V., EAGE Education Tour Series.

Dutton, S. P., E. M. Kim, R. F. Broadhead, C. L. Breton, W. D. Raatz, S. C. Ruppel, and C. Kerans, 2004, Play analysis and digital portfolio of major oil reservoirs in the Permian Basin:

Application and transfer of advanced geological and engineering technologies for incremental production opportunities: University of Texas.

Flamm, D. S., 2008, Wolfcampian development of the nose of the Eastern Shelf of the Midland Basin, Glasscock, Sterling, and Reagan Counties, Texas: M.S. thesis, Brigham Young University.

Folk, R. L., 1964, Some aspects of recrystallization in ancient limestones, in L. C. Pray and R. C. Murray, eds., Dolomitization and limestone diagenesis: Society for Sedimentary Geology, Special Publications 13, 14–48.

Grana, D., 2013, Bayesian inversion methods for seismic reservoir characterization and time-lapse studies: Ph.D. thesis, Stanford University.

Hamlin, H. S., and R. W. Baumgardner, 2013, Wolfberry (Wolfcampian-Leonardian) deep-water depositional systems in the Midland Basin: Stratigraphy, lithofacies, reservoirs, and source rocks: Bureau of Economic Geology.

Hampson, D. J., S. Schuelke, and J. Quirein, 2001, Use of multiattribute transforms to predict log properties from seismic data: Geophysics, 66, 220–236, doi: 10.1190/1.1444899.

Hill, S. J., 2005, Inversion-based thickness determination: The Leading Edge, 24, 477–480, doi: 10.1190/1.1926799.

Hills, J. M., 1985, Structural evolution of the Permian basin of West Texas and New Mexico, in P. A. Dickerson and W. R. Muehlberger, eds., Structure and tectonics of trans-Pecos Texas: West Texas Geological Society Field Conference, Publication 85-81, 89–99.

Himmer, P., and C. Link, 1997, Reservoir porosity prediction from 3-D seismic data using neural networks: 67th Annual International Meeting, SEG, Expanded Abstracts, 842–845, doi: 10.1190/1.1886145.

Horak, R. L., 1985, Tectonic and hydrocarbon maturation history in the Permian Basin: Oil and Gas Journal, 83, 124–129.

Jones, G. D., and Y. Xiao, 2005, Dolomitization, anhydrite cementation, and porosity evolution in a reflux system: Insights from reactive transport models: AAPG Bulletin, 89, 577–601, doi: 10.1306/12010404078.

Kalkomey, C. T., 1997, Potential risks when using seismic attributes as predictors of reservoir properties: The Leading Edge, 16, 247–251, doi: 10.1190/1.1437610

Kerans, C., F. J. Lucia, and R. K. Senger, 1994, Integrated characterization of carbonate ramp reservoirs using Permian San Andres Formation outcrop analogs: AAPG Bulletin, 78, 181–216, doi: 10.1306/BDFF905A-1718-11D7-8645000102C1865D.

Land, L. S., 1985, The origin of massive dolomite: Summary and suggestion: Journal of Geological Education, 33, 112–125, doi: 10.5408/0022-1368-33.2.112.

Landreth, R. A., 1977, Depositional environments and diagenesis of the lower clear fork group, Mitchell County, Texas: M.S. thesis, Texas Tech.

Lucia, F. J., and R. P. Major, 1994, Porosity evolution through hypersaline reflux dolomitization, in B. Purser, M. Tucker, and D. Zenger, eds., Dolomites: International Association of Sedimentologists Special Publication 21, 325–341, doi: 10.1002/9781444304077.ch18

26

Mackenzie, F. T., and J. W. Morse, 1992, Sedimentary carbonates through Phanerozoic time: Geochimica et Cosmochimica Acta, 56, 3281–3295, doi: 10.1016/0016-7037(92)90305-3.

Major, R. P., D. G. Bebout, and F. J. Lucia, 1988, Depositional facies and porosity distribution, Permian (Guadalupian) San Andres and Grayburg Formations, P.J.W.D.M. field complex, Central Basin Platform, West Texas, giant oil and gas fields: SEPM Core Workshop Notes 12, 615–648, doi: /10.2110/cor.88.12.0615.

Masters, T., 1995, Advanced algorithms for neural networks: John Wiley & Sons Inc.

Mazzullo, S. J., 1994, Dolomitization of periplatform carbonates (Lower Permian, Leonardian), Midland basin, Texas: Carbonates and Evaporites, 9, 95–112, doi: 10.1007/BF03175189.

Mazzullo, S. J., and A. M. Reid, 1989, Lower Permian platform and basin depositional systems, northern Midland Basin, Texas, in P. D. Crevello, J. L. Wilson, J. F. Sarg, and J. F. Read, eds., Controls on carbonate platforms and basin development: Special Publications: SEPM, 305–320, doi: 10.2110/pec.89.44.0305.

Nieto, J., B. Batlai, and F. Delbecq, 2013, Seismic lithology prediction: A Monterey Shale gas case study: CSEG Recorder, 38, 34–43.

Presley, M. W., 1987, Evolution of Permian evaporite basin in Texas panhandle: AAPG Bulletin, 71, 167–190, doi: 10.1306/94886D67-1704-11D7-8645000102C1865D.

Ruppel, S. C., 1992, Styles of deposition and diagenesis in Leonardian carbonate reservoirs in west Texas: Implications for improved reservoir characterization: Annual Exhibition and Technical Conference, SPE, Extended Abstracts, 313–320, doi: 10.2118/24691-MS.

Russell, B. H., 2004, The application of multivariate statistics and neural networks to the prediction of reservoir parameters using seismic attributes: Ph.D. dissertation, University of Calgary.

Russell, B., D. Hampson, and B. Bankhead, 2006, An inversion primer, CSEG Recorder Special Edition, no. 1, 96–103.

Saller, A. H., 2004, Paleozoic dolomite reservoirs in the Permian Basin, SW USA: Stratigraphic distribution, porosity, permeability, and production: Geological Society, London, Special Publications 235, 309–323.

Saller, A. H., 2013, Diagenetic evolution of porosity in carbonates during burial: AAPG Search and Discovery Article #50779.

Saller, A. H., and N. Henderson, 1998, Distribution of porosity and permeability in platform dolomites: Insight from the Permian of West Texas: AAPG Bulletin, 82, 1528–1550, doi: 10.1306/1D9BCB01-172D-11D7-8645000102C1865D.

Sarg, J. F., J. R. Markello, and L. J. Weber, 1999, The second-order cycle, carbonate platform growth, and reservoir, source, and trap prediction, Advances in carbonate sequence stratigraphy: Application to reservoirs, outcrops, and models, P. M. Harris and J. A. Toni Simo: Special Publication: SEPM Society for Sedimentary Geology 63, 11–34.

Sengupta, M., and R. Bachrach, 2007, Uncertainty in seismic-based pay volume estimation: Analysis using rock physics and Bayesian statistics: The Leading Edge, 26, 184–189, doi: 10.1190/1.2542449.

Specht, D. F., 1995, Probabilistic neural networks and general regression neural networks, in C. H. Chen, ed., Fuzzy logic and neural network handbook: McGraw-Hill Inc., 301–344.

Sun, S. Q., 1995, Dolomite reservoirs: Porosity evolution and reservoir characteristics: AAPG Bulletin, 79, 186–204, doi: 10.1306/8D2B14EE-171E-11D7-8645000102C1865D.

Swisi, A., 2009, Post- and pre-stack attribute analysis and inversion of Blackfoot 3D seismic dataset: M.S. thesis, The University of Saskatchewan.

Tyler, N., D. G. Bebout, C. M. Garrett Jr., E. H. Guevara, C. R. Hocott, M. H. Holtz, S. D. Hovorka, C. Kerans, F. J. Lucia, R. P. Major, S. C. Ruppel, and G. W. Vander Stoep, 1991, Integrated characterization of Permian Basin reservoirs, University Lands, West Texas: Targeting the remaining resource for advanced oil recovery: The University of Texas at Austin, Bureau of Economic Geology, Report of Investigations No. 203.

Vahrenkamp, V. C., P. K. Swart, and J. Ruiz, 1991, Episodic dolomitization of late Cenozoic carbonates in the Bahamas; Evidence from strontium isotopes: Journal of Sedimentary Petrology, 61, No.6, 1002–1014, doi: 10.23867/RI0203D.

Veeken, P. C. H., and M. da Silva, 2004, Seismic inversion and some of their constraints: First Break, 22, No. 6, 47–70, doi: /10.3997/1365-2397.2004011.

Verma, S., T. Zhao, K. J. Marfurt, and D. Devegowda, 2016, Estimation of TOC and brittleness volume: Interpretation, 4, no. 3, T373–T385, doi: 10.1190/INT-2015-0166.1.

Ward, R. F., C. Kendall, and P. M. Harris, 1986, Upper Permian (Guadalupian) facies and their association with hydrocarbons Permian Basin, West Texas and New Mexico: AAPG Bulletin, 70, 239–262, doi: 10.1306/9488566F-1704-11D7-8645000102C1865D.

Warren, J., 2000, Dolomite: Occurrence, evolution and economically important associations: Earth-Science Reviews, 52, 1–81, doi: 10.1016/S0012-8252(00)00022-2.

Weyl, P. K., 1960, Porosity through dolomitization: Conservation-of-mass requirements: Journal of Sedimentary Research, 30, 85–90.

Wiggins, W. D., and P. M. Harris, 1985, Burial diagenetic sequence in deep-water allochthonous dolomites, Permian Bone Spring Formation, southeast New Mexico, in P. D. Crevello and P. M. Harris, eds., Deep-water carbonates: Buildups, turbidites, debris flows and chalks: SEPM Core Workshop 6, 140–173, doi: /10.2110/cor.85.06.0140.

Ye, Q., and S. J. Mazzullo, 1993, Dolomitization of lower Permian platform facies, Wichita Formation, north platform, Midland basin, Texas: Carbonates and Evaporites, 8, 55–70, doi: 10.1007/BF03175163.

Chapter 1 Figures
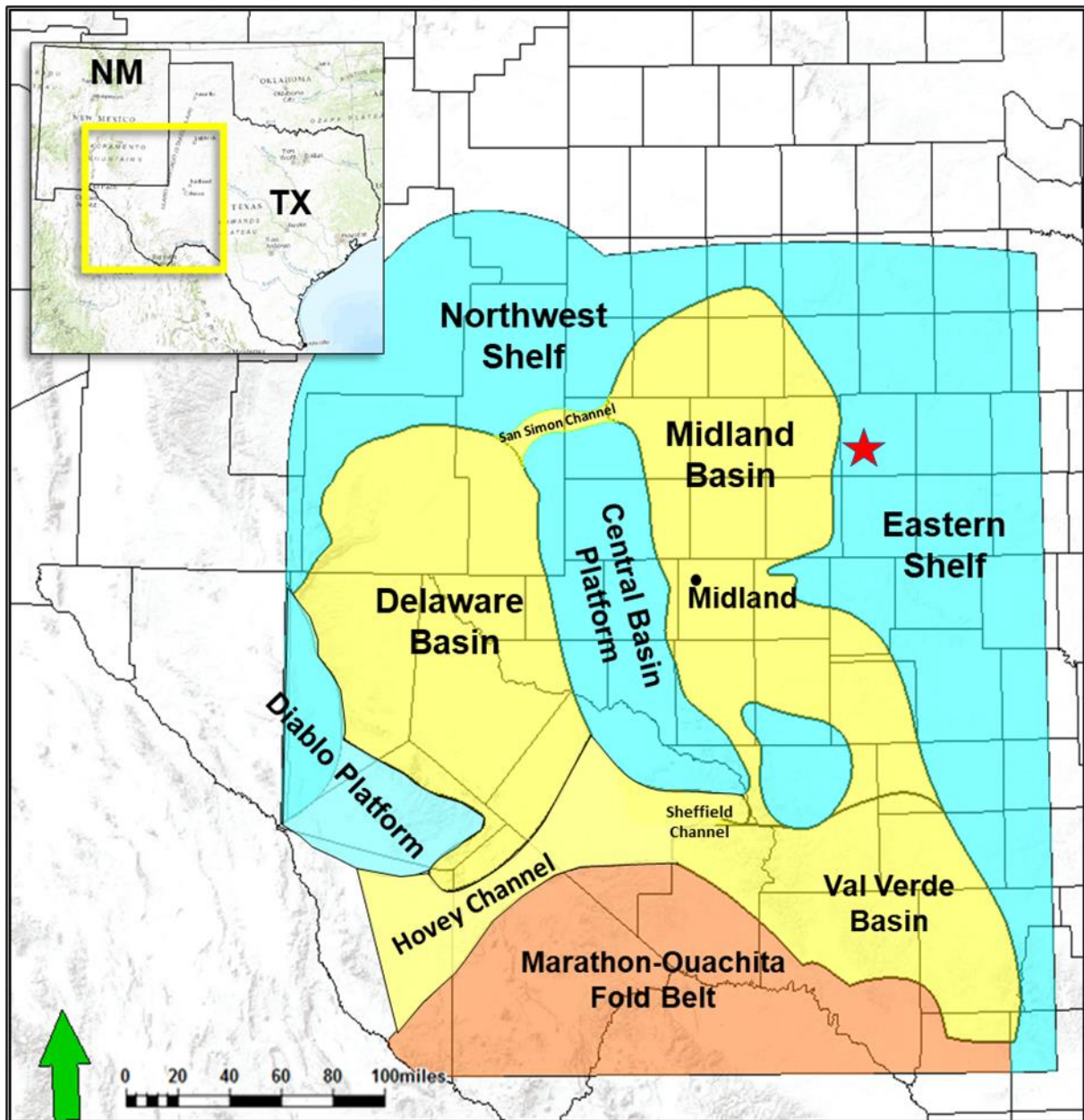
Figure 1.1: Paleogeographic map showing the main provinces of the Permian Basin during the Early Permian time. The study area is located in Scurry County, Texas. The approximate location of the study area is denoted by the red star.

AGE		STRATIGRAPHIC UNIT	
SYSTEM	SERIES	MIDLAND BASIN	EASTERN SHELF
PERMIAN	Ochoan	Dewey Lake	
		Rustler	Rustler
		Salado	Salado
	Guadalupian	Tansill	Tansill
		Yates	Yates
		Seven Rivers	Seven Rivers
		Queen	Queen
		Grayburg	Grayburg
		San Andres	San Andres
	Leonardian	Spraberry	Clearfork
		Dean	
		Leonard	Wichita
	Wolfcampian	Wolfcamp	Wolfcamp

Figure 1.2: Simplified stratigraphic chart showing the regional stratigraphy of the Midland Basin and the Eastern Shelf (modified after Ball, 1995). The interval of interest for this study is the Leonardian Wichita and Clear Fork Formations (the red square).
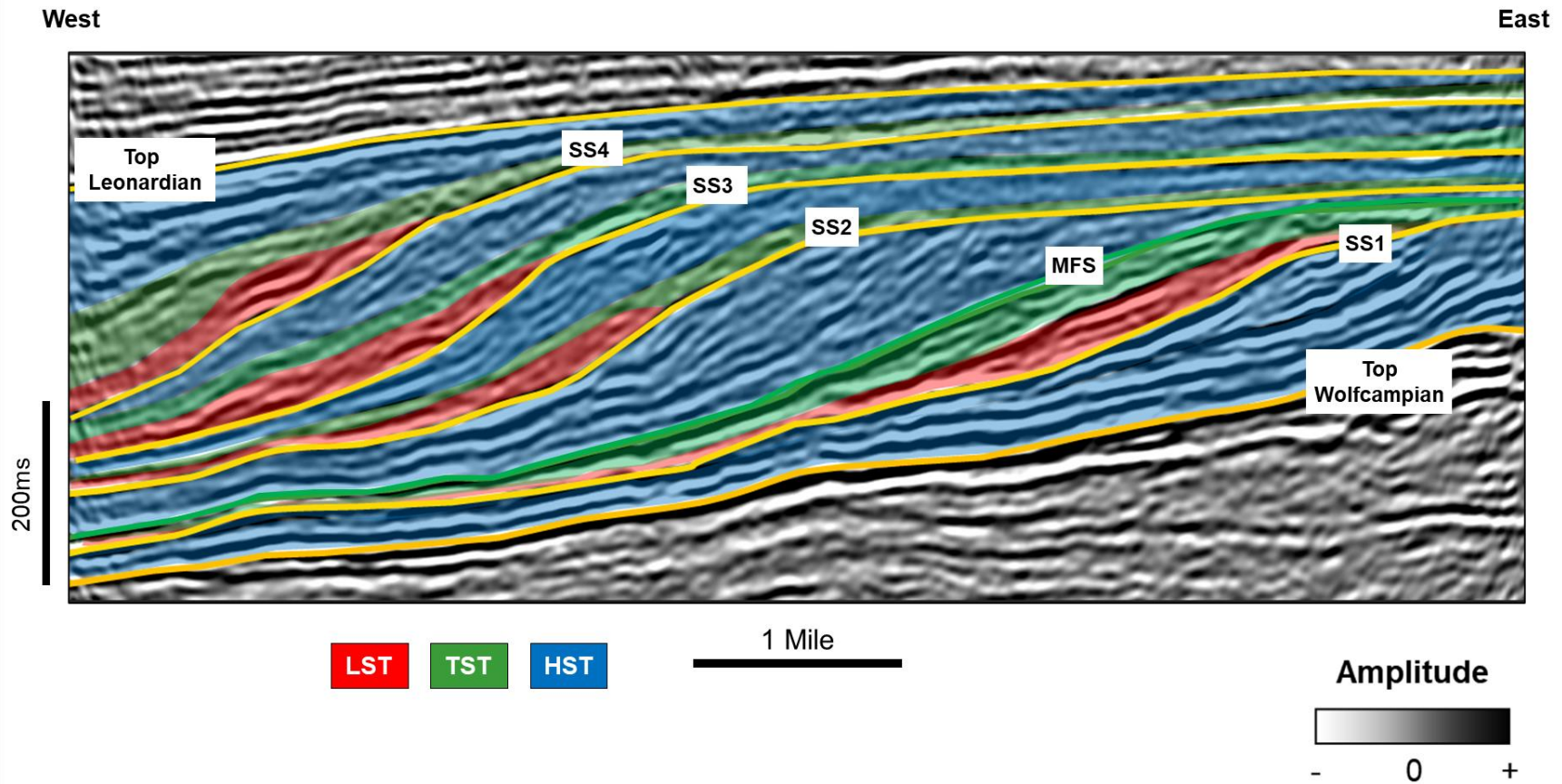
Figure 1.3: Seismic stratigraphic interpretation of east–west arbitrary line illustrating the progradation-retrogradation episodes of the Leonardian platform carbonates with distinct clinoformal geometries. Four complete seismic sequences were interpreted within the Leonardian section (LST, lowstand systems tract; TST, transgressive systems tract; HST, highstand systems tract; SS1-5, seismic sequence boundaries; and MFS, maximum flooding surface).
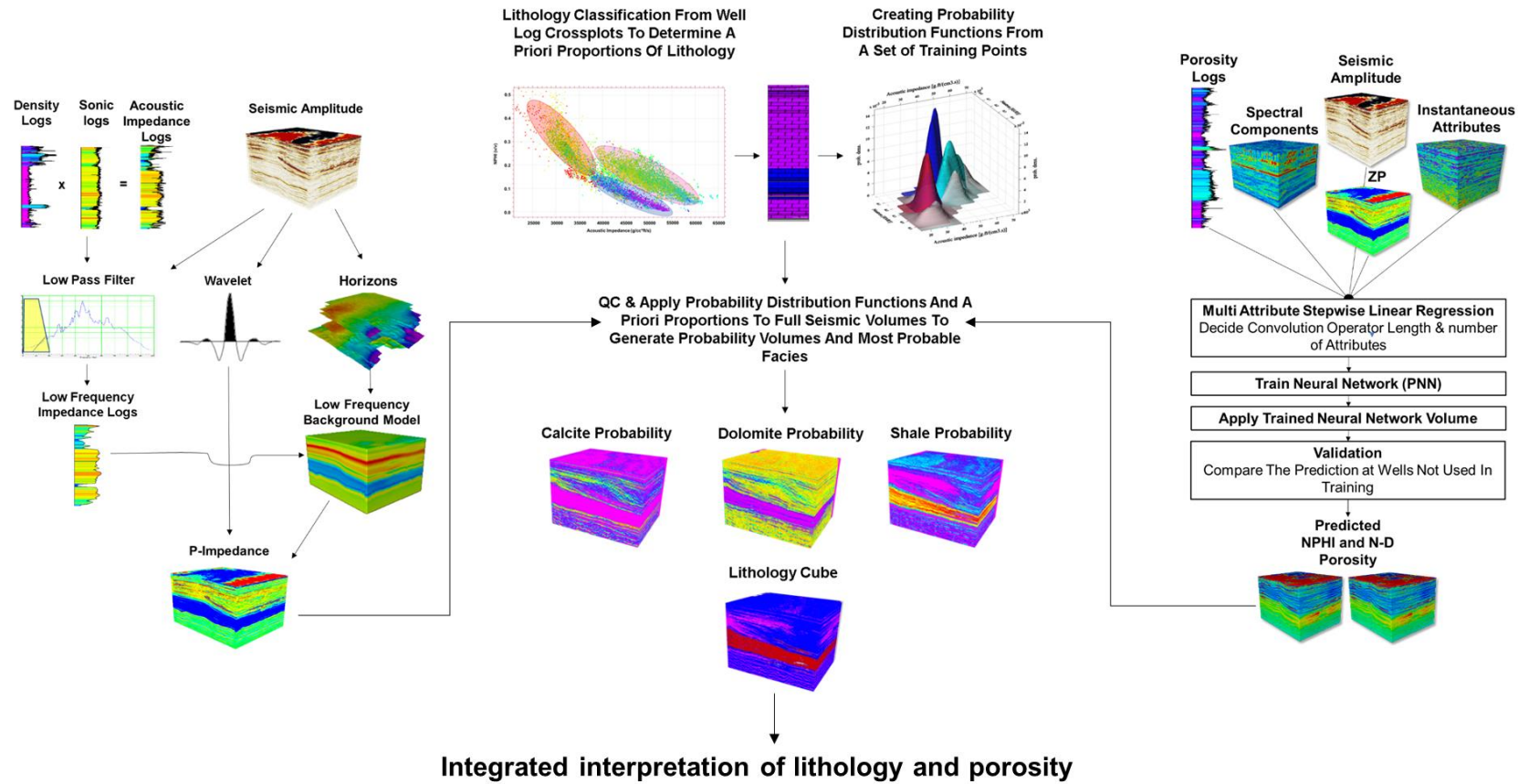
Figure 1.4: Generalized workflow showing the three main steps followed in this study. These steps are the (left) model-based poststack inversion (after Russel et al., 2006), (middle) Bayesian supervised classification (after Nieto et al., 2013), and (right) PNN for porosity prediction (after Verma et al., 2016).

34
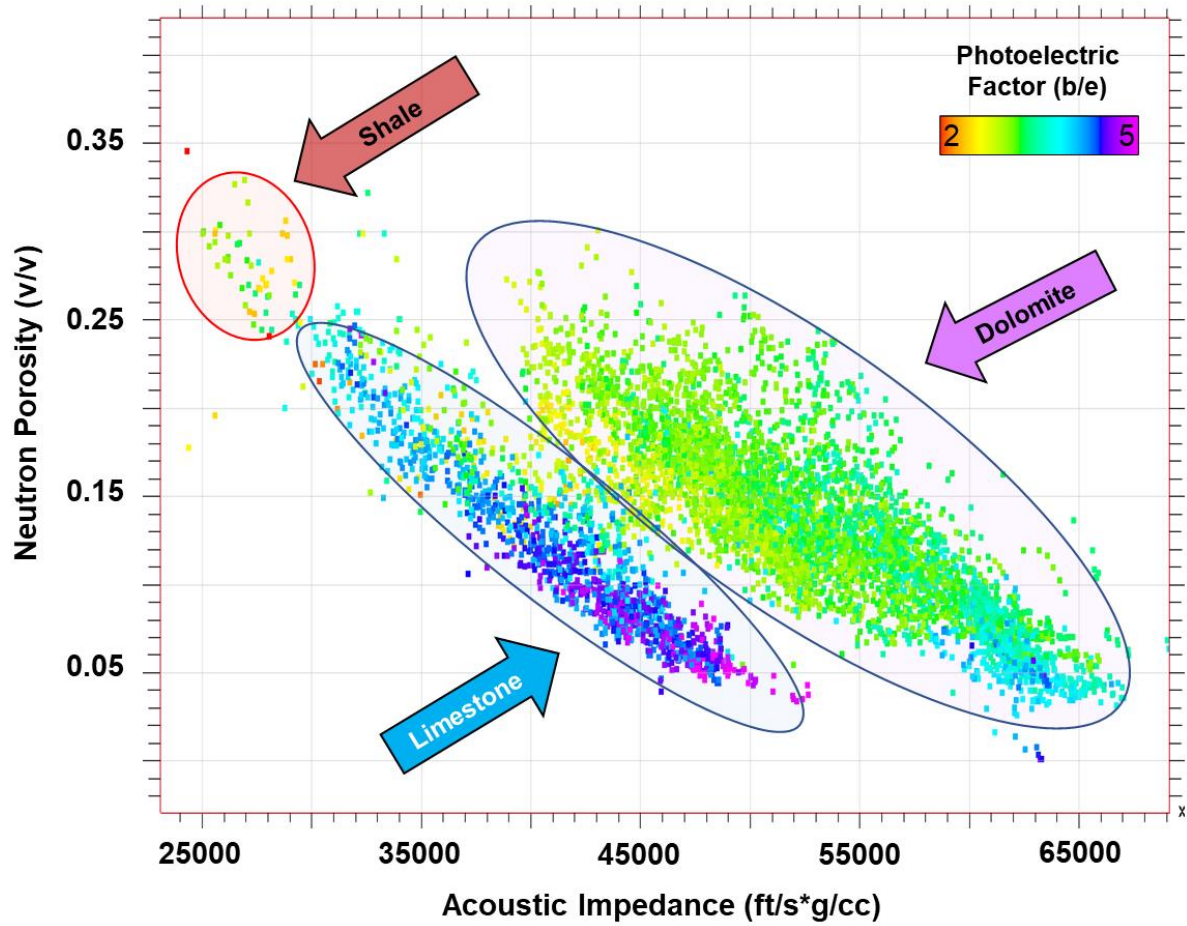
Figure 1.5: Crossplot of acoustic impedance and neutron porosity logs, color-coded by photoelectric factor log showing distinct separations interpreted as limestone, dolomite, and shale.
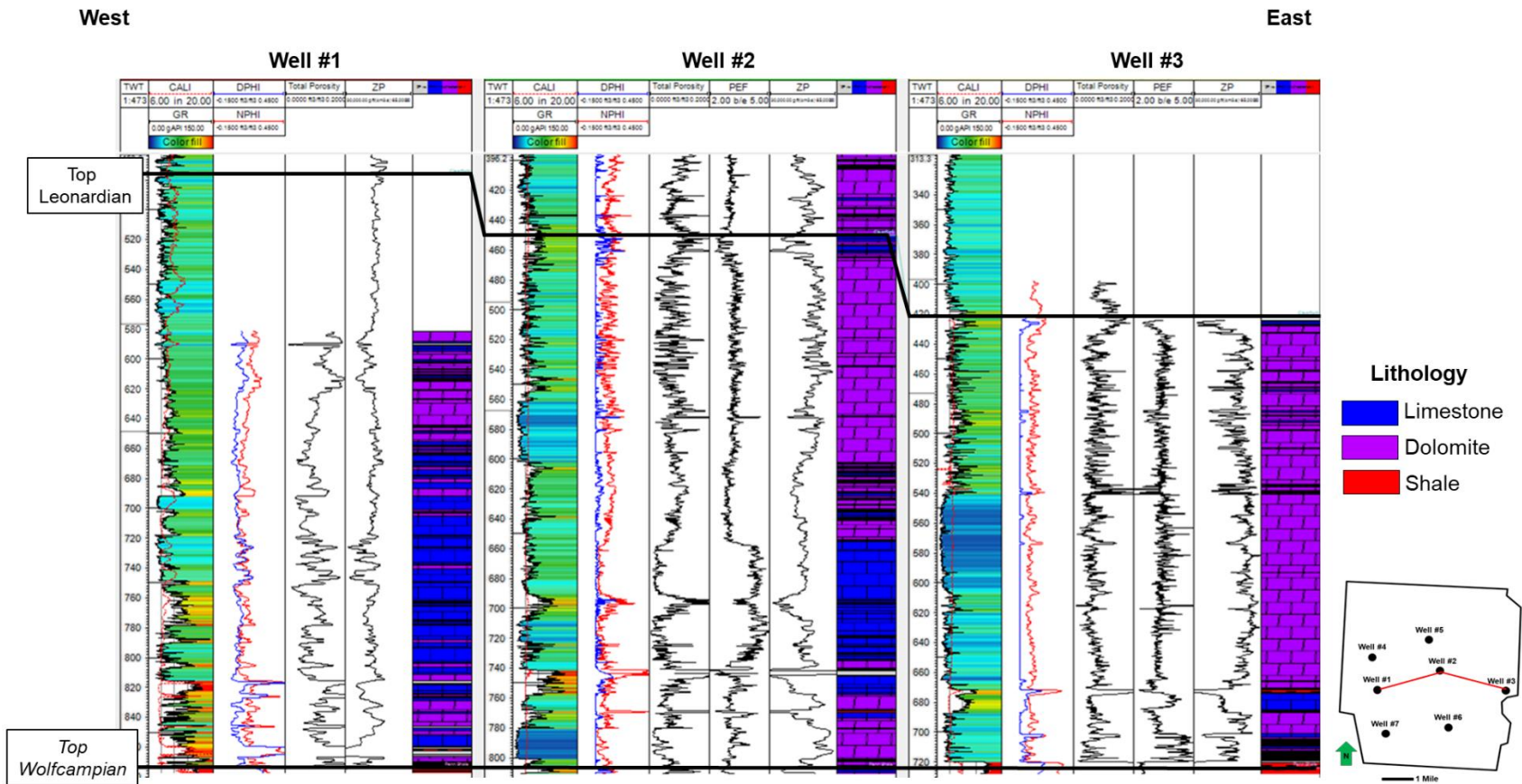
Figure 1.6: East–west cross section of wells showing the lithology logs together with a suite of well logs (track 1, overlay of Gamma Ray and Caliper; track 2, overlay of Neutron and Density porosity logs; track 3, Total porosity; track 4, Photoelectric Factor Log; track 5, Acoustic Impedance; and track 6, Lithology).
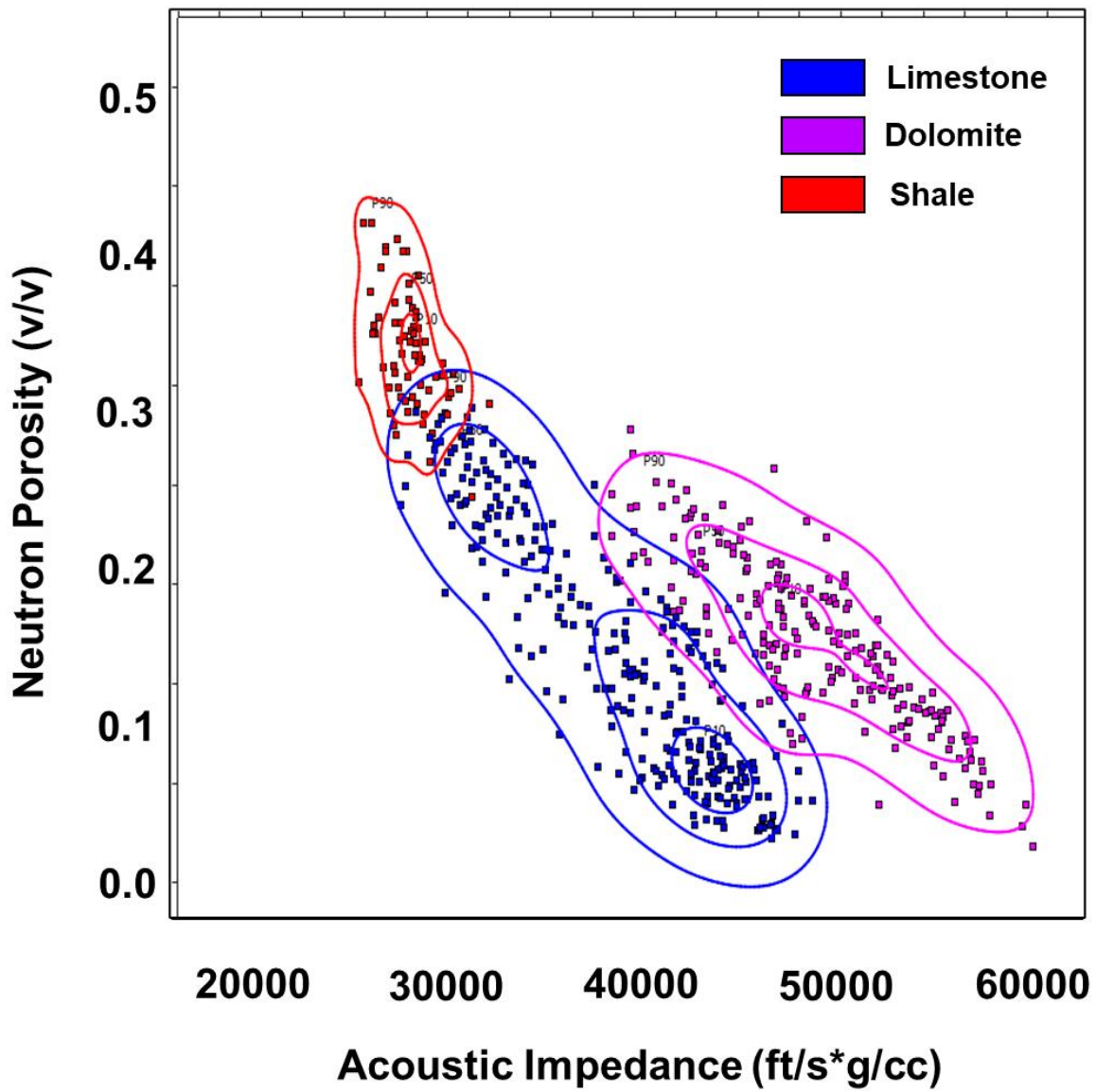
Figure 1.7: PDFs calculated from upscaled well logs for each lithology type.
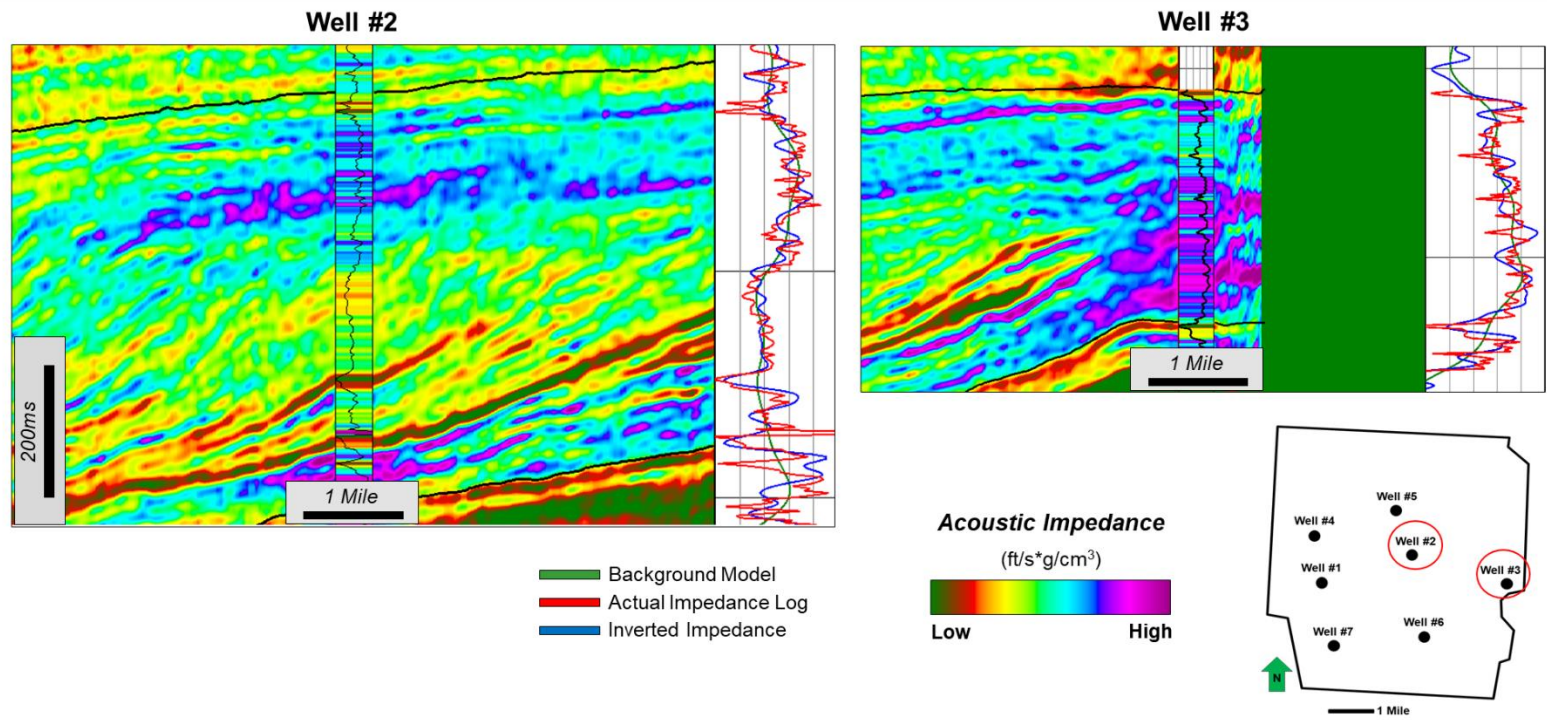
Figure 1.8: QC of the post-stack inversion results extracted at well locations 2 and 3. Note the high impedance values of the Leonardian section at the platform interior (well 3), which decrease toward the slope (well 2).
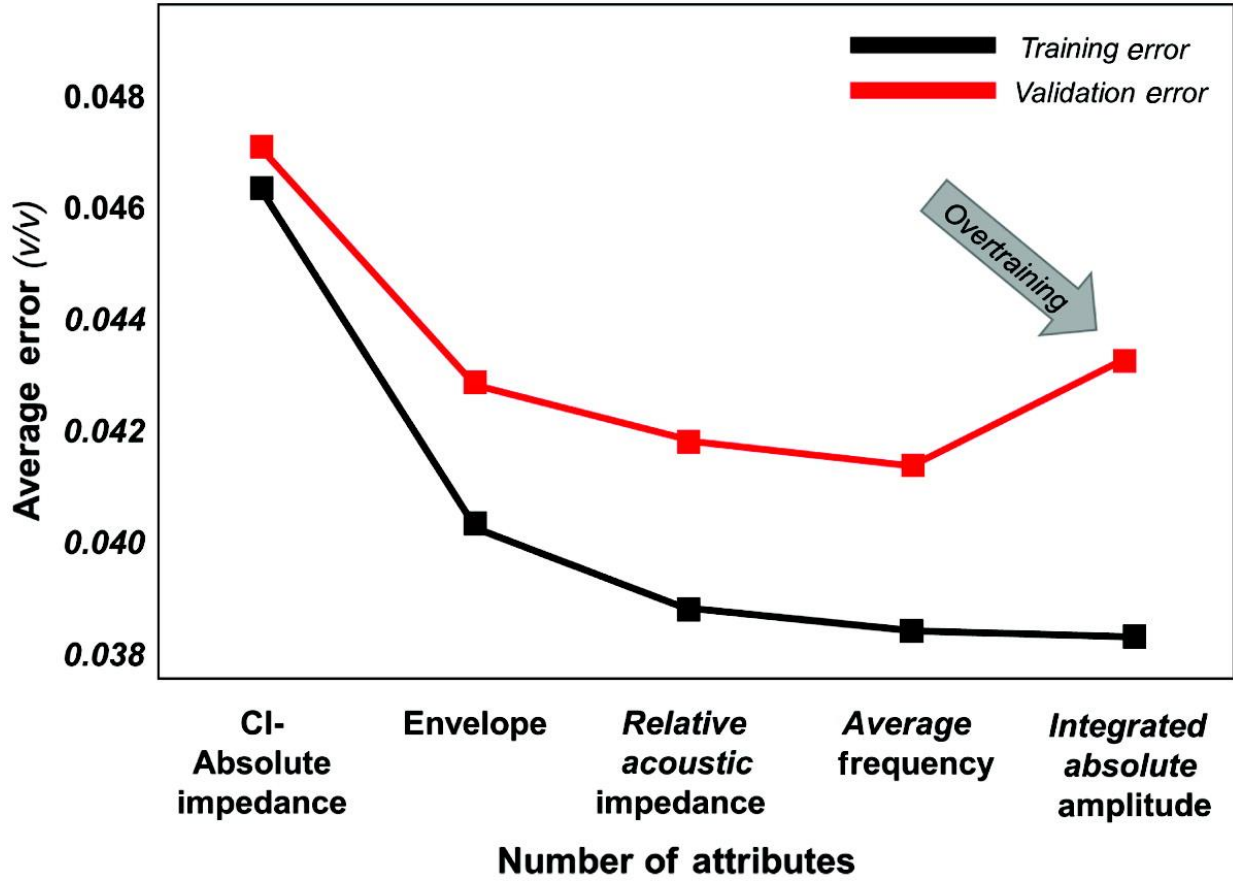
Figure 1.9: Selection of the optimum number of attributes for PNN neutron porosity volume prediction. The training and validation errors are plotted against the number of attributes. Note the increase in validation error after four attributes, indicating overtraining.
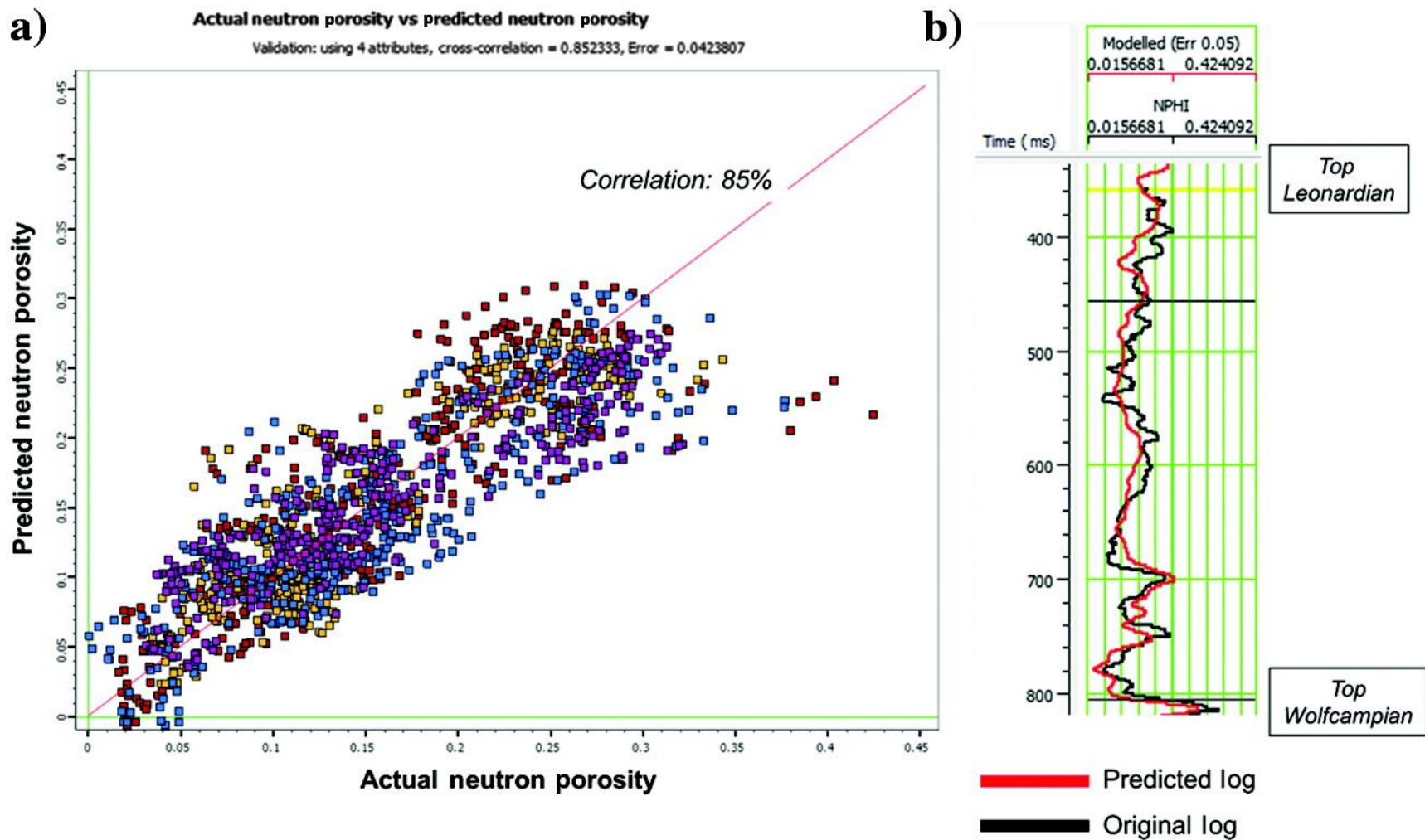
Figure 1.10: Validation results of the PNN neutron porosity volume prediction. (a) Crossplot between the actual and predicted neutron porosity values shows an 85% correlation. (b) Blind well (well 6) validation of the PNN results.
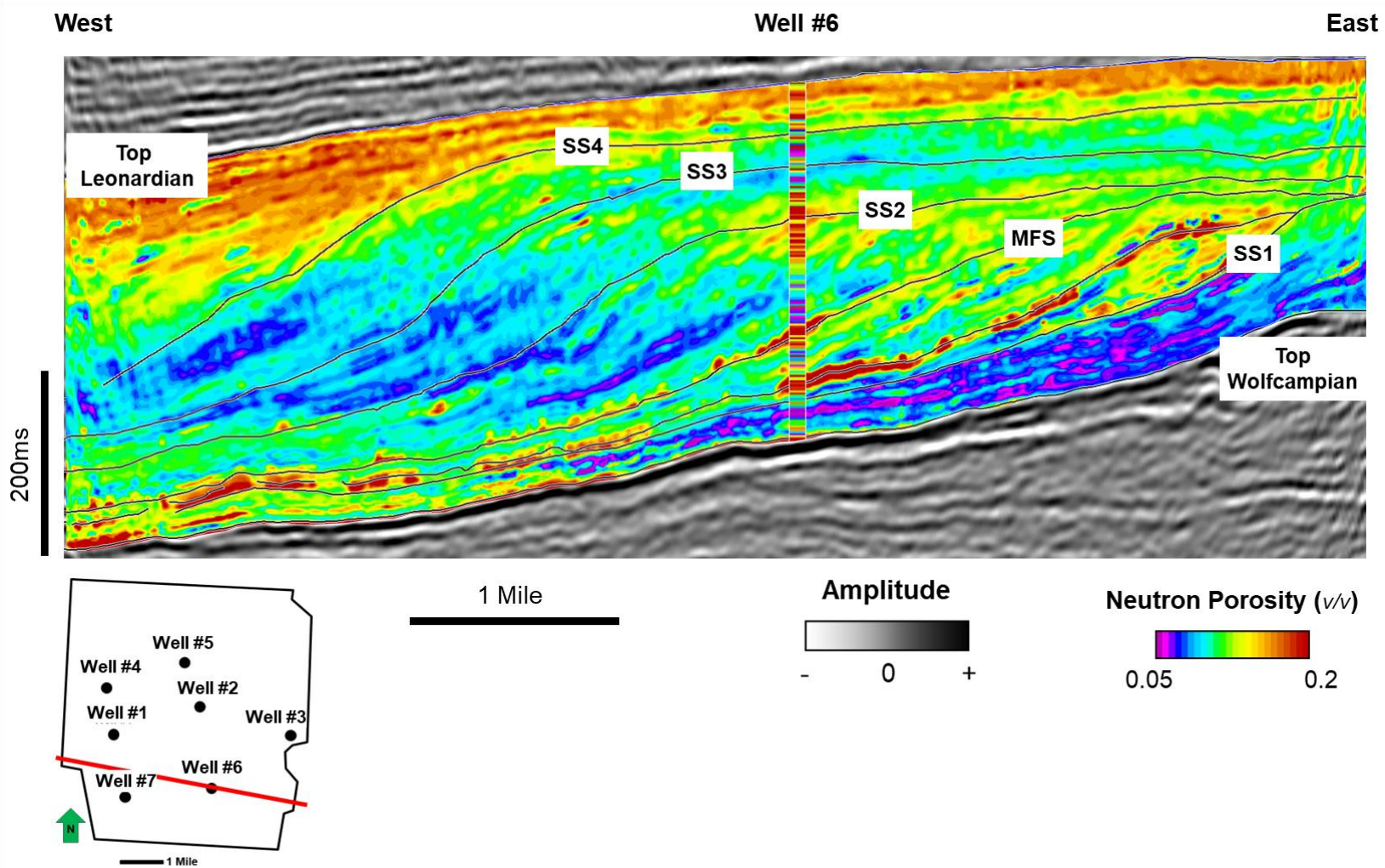
Figure 1.11: Arbitrary line through the blind validation well (well 6) showing the PNN neutron porosity volume prediction result.
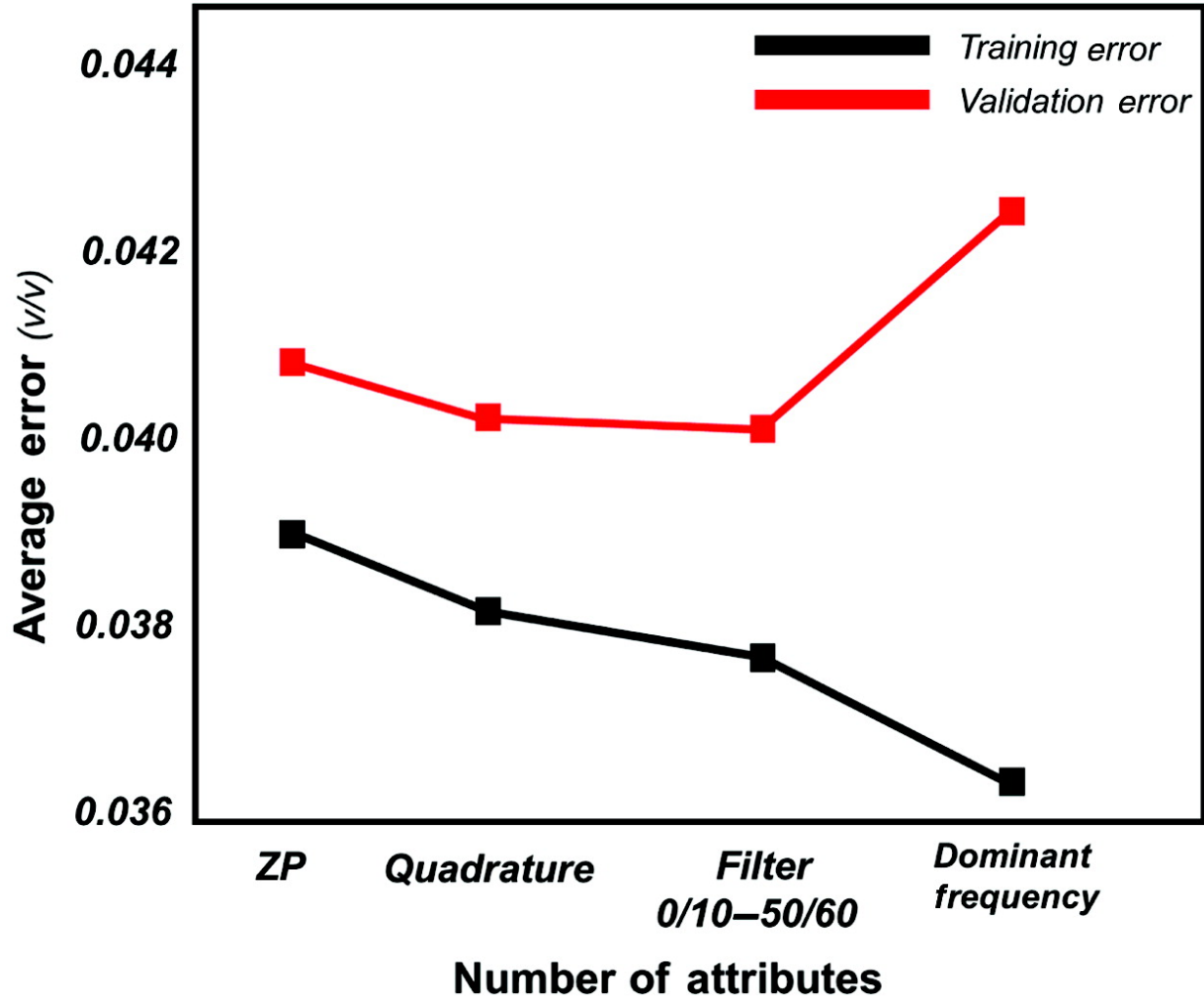
Figure 1.12: Selection of the optimum number of attributes for the PNN total porosity volume prediction. The training and validation error curves indicate that using three attributes yields the lowest validation error.
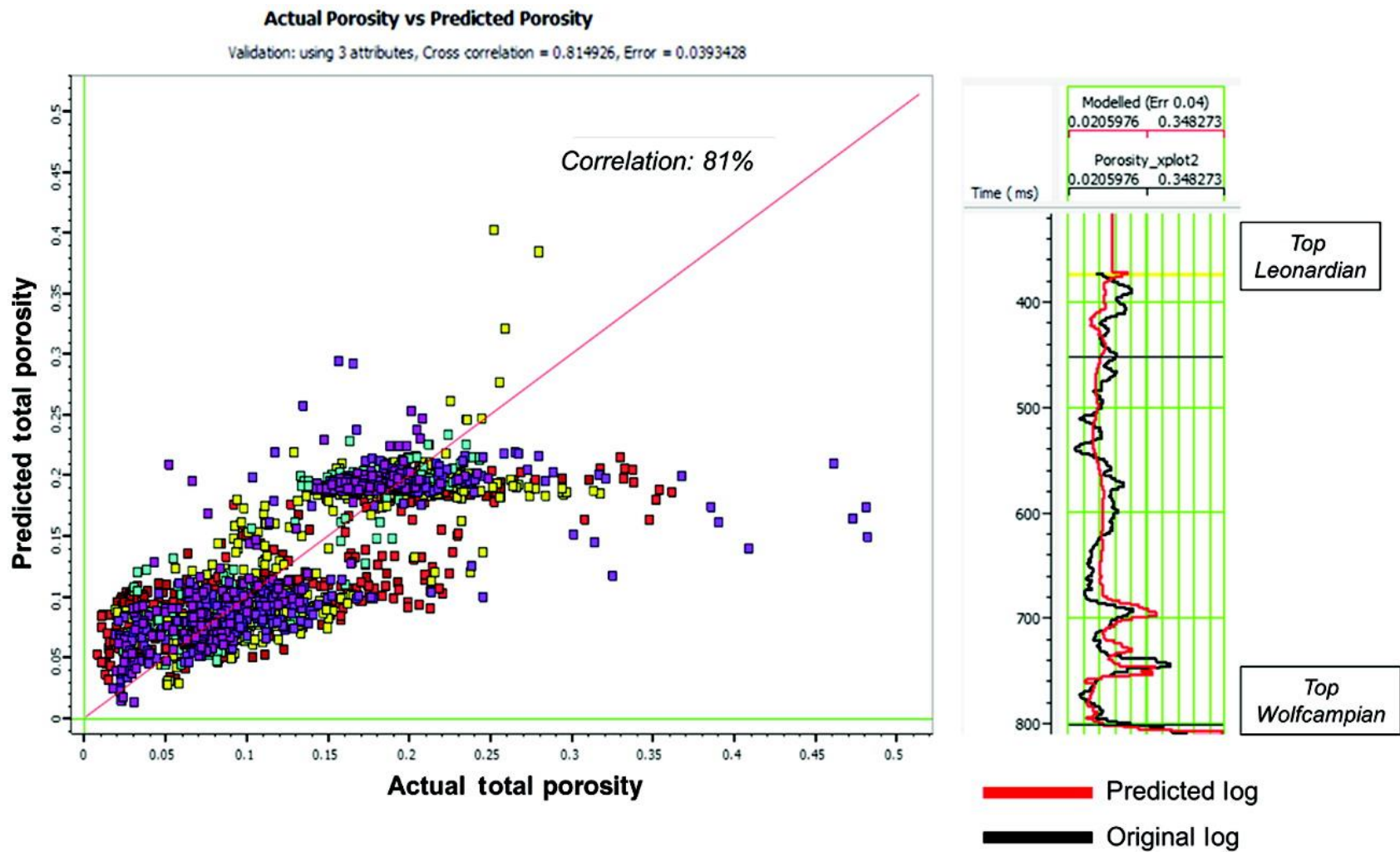
Figure 1.13: Validation results of the PNN total porosity prediction volume. (Left) A crossplot between the actual and predicted total porosity values shows an 81% correlation. (Right) Blind well validation of the PNN results.
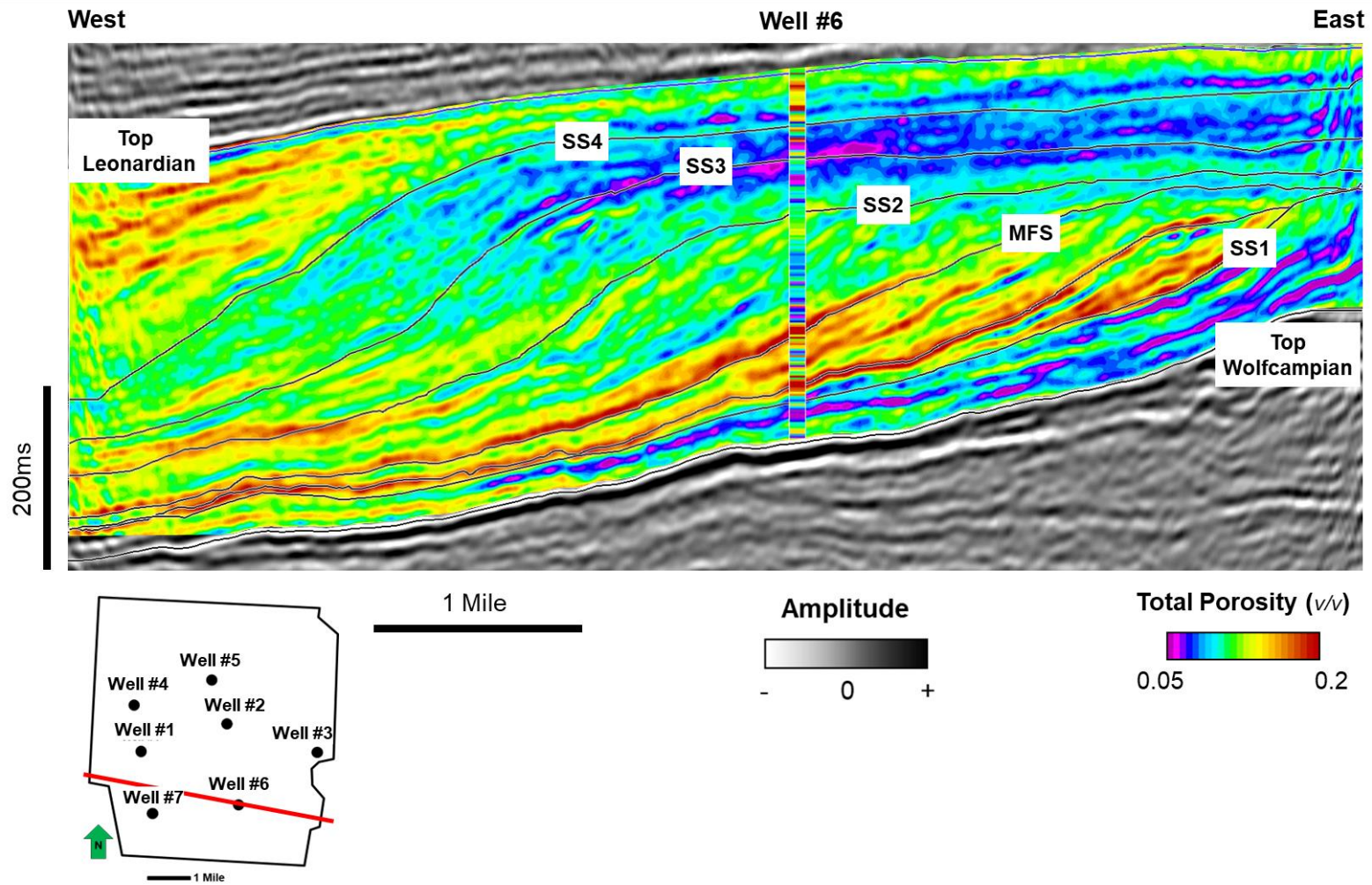
Figure 1.14: The arbitrary line through the blind validation well (well 6) showing the PNN total porosity volume prediction results.
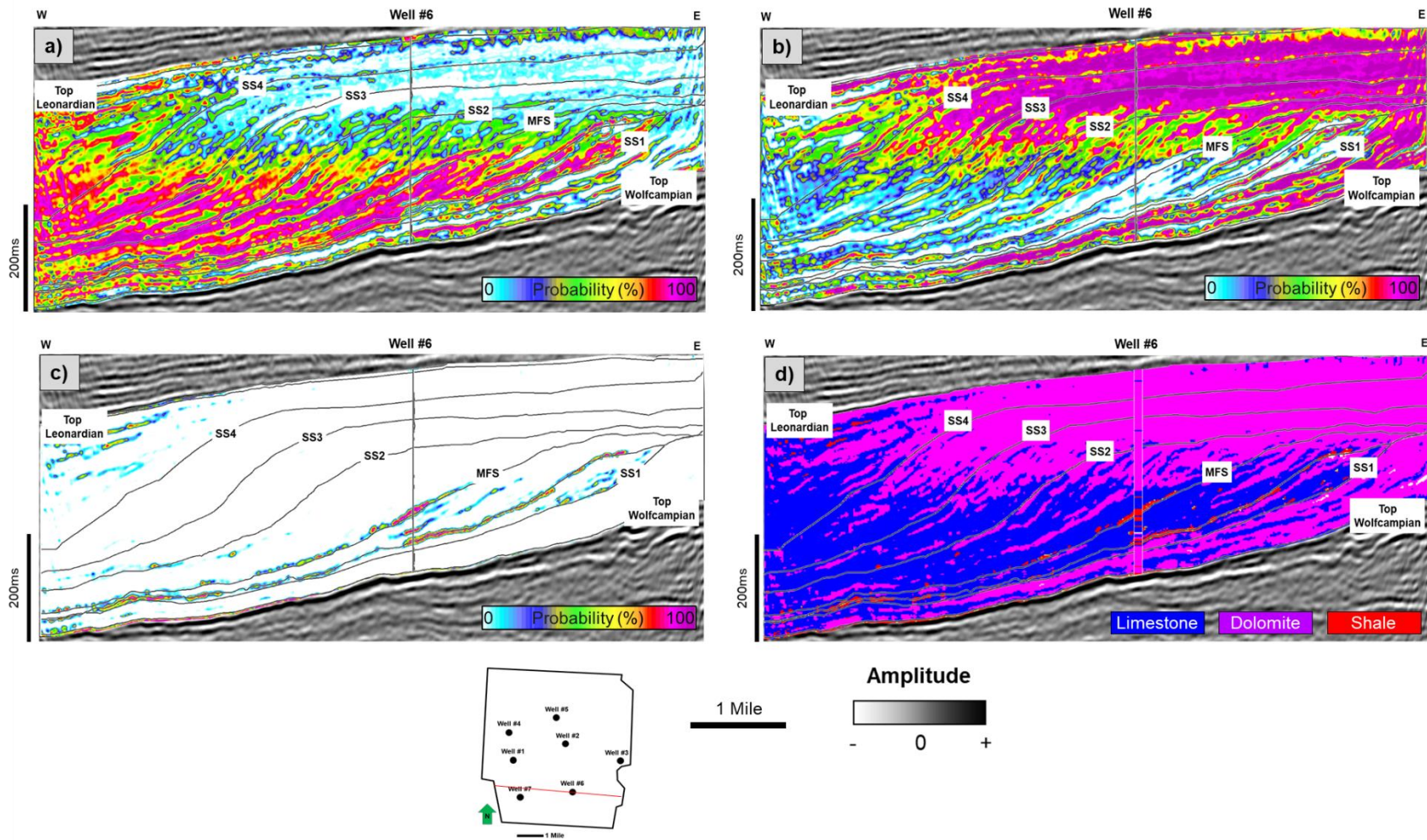
Figure 1.15: Supervised Bayesian classification results at an arbitrary line through well 6. The output volumes are the probabilities of each lithology type and the most probable lithology volume: (a) probability of limestone, (b) probability of dolomite, (c) probability of shale, and (d) the most probable lithology volume.
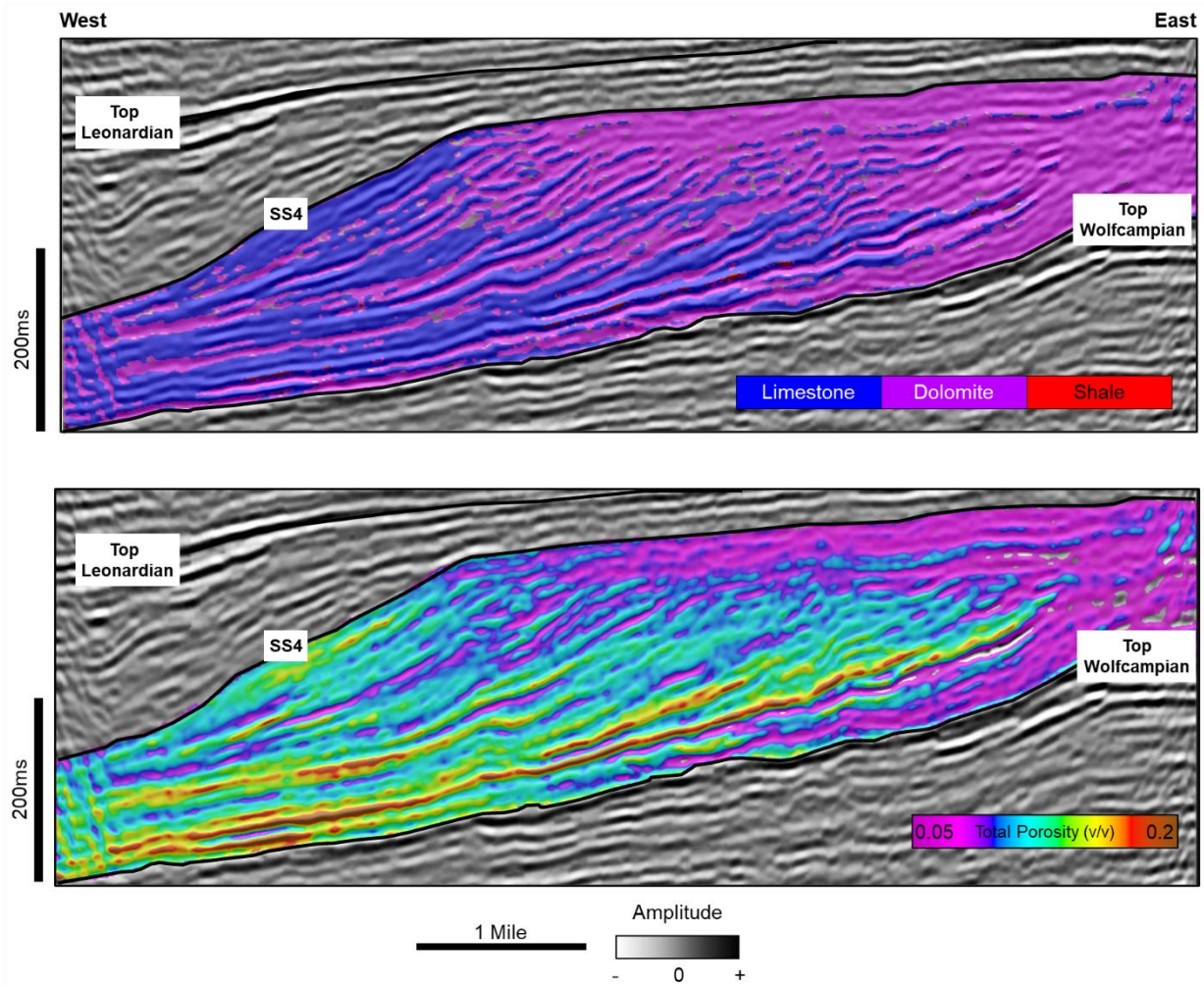
Figure 1.16: Lower to Middle Permian sections through arbitrary lines from the most probable lithology and PNN predicted total porosity volumes. The arbitrary line showing the most probable lithology co-rendered with the seismic amplitude values. Note that the platform interior and shelf is dominantly dolomite, whereas the slope is limestone (Upper image). The predicted total porosity extracted on the same arbitrary line showing increasing porosity from shelf to slope (Lower Image).
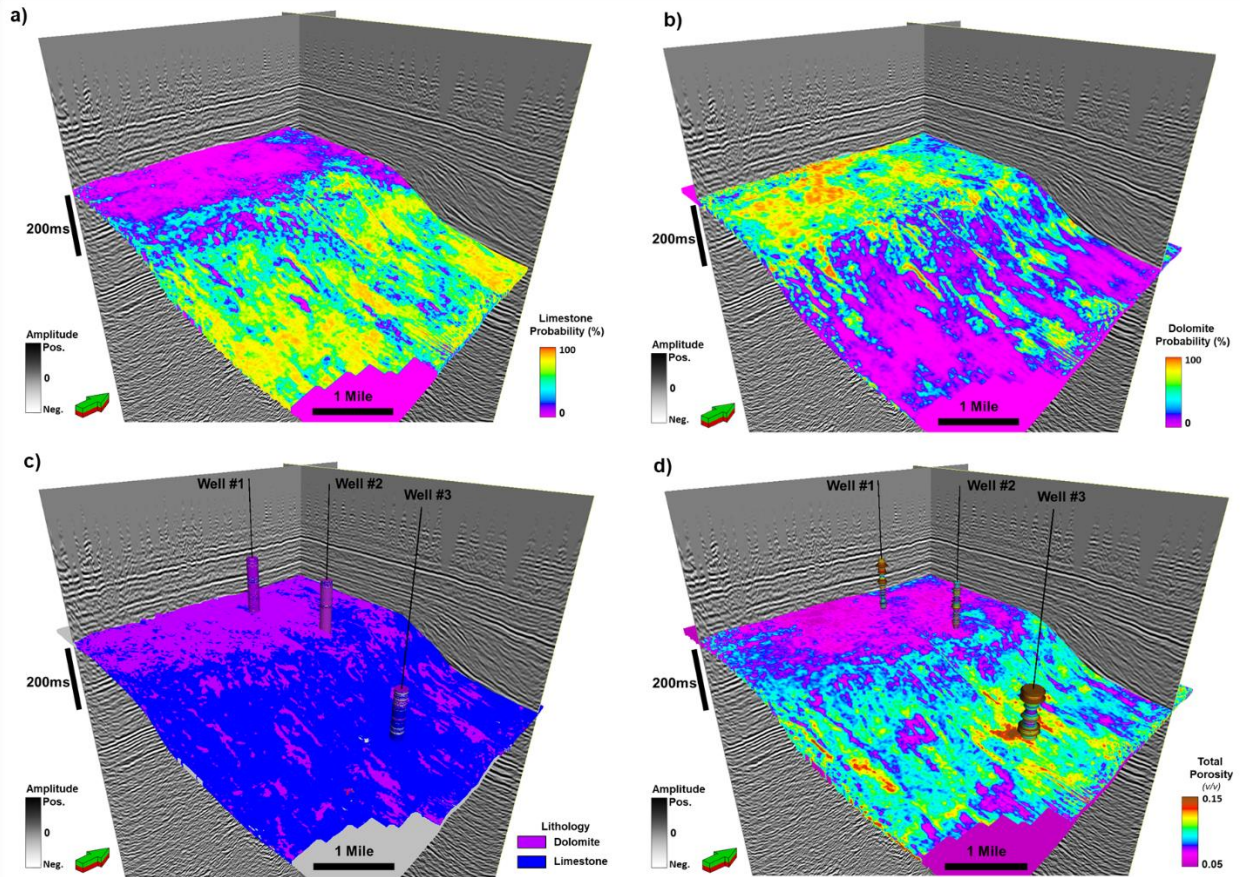
Figure 1.17: Supervised Bayesian classification and PNN total porosity prediction results extracted on the SS3 surface. Note (a) the increasing limestone probability from the shelf to slope. (b) Extracted dolomite probability values show the opposite trend where the shelf top has a high probability of dolomite, decreasing distally to the down-slope direction. (c) The most probable lithology surface shows that the dominant lithology of the shelf is dolomite, whereas the slope is mainly composed of limestone. (d) Extracted PNN total porosity values showing the porosity increase from the shelf to the slope.
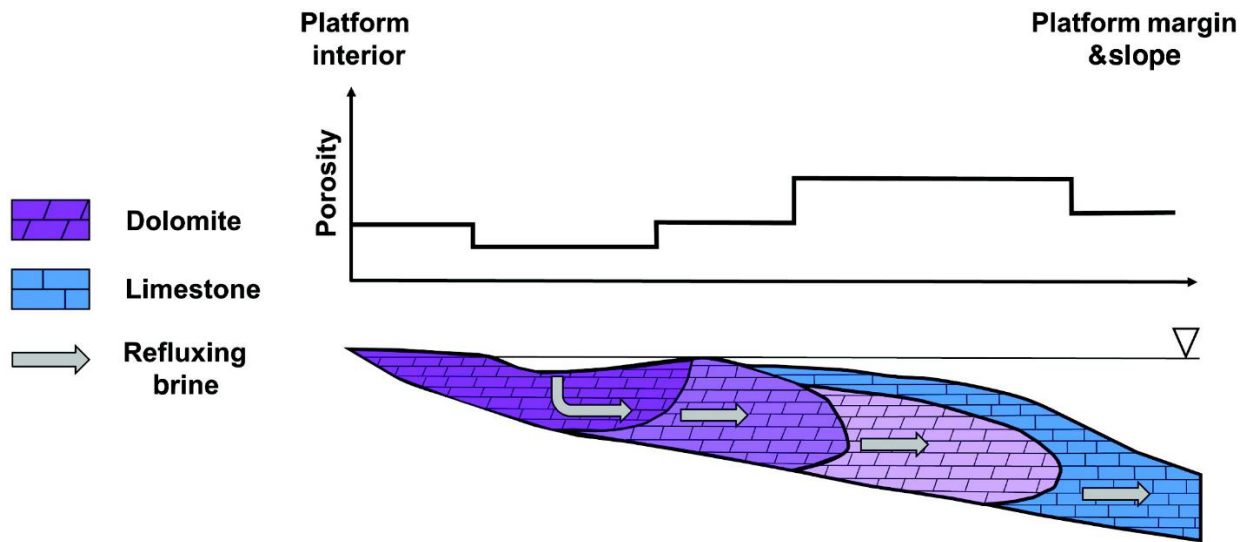
Figure 1.18: A conceptual model of reflux dolomitization. Note that the platform interior is mainly replaced with nonporous dolomite due to the cementation proximal to the brine source, whereas the porosity increases basinward with a decreasing degree of dolomitization (modified after Jones and Xiao, 2005; Saller, 2013).

Chapter 1 Tables

Target	Final Attribute	Training Error (v/v)	Validation Error (v/v)
Neutron Porosity	Colored Inversion-Absolute Impedance	0.046053	0.047575
Neutron Porosity	Envelope	0.040881	0.042741
Neutron Porosity	Relative Acoustic Impedance	0.039697	0.042486
Neutron Porosity	Average Frequency	0.039299	0.042381

Table 1.1: Training and validation errors of the attributes used in the PNN training for neutron porosity volume prediction.

Target	Final Attribute	Training Error (v/v)	Validation Error (v/v)
Total Porosity	Acoustic Impedance- Post Stack Inversion	0.039087	0.041144
Total Porosity	Quadrature Trace	0.038250	0.040695
Total Porosity	Filter 0/10-50/60	0.037826	0.040555

Table 1.2: Training and validation errors of the attributes used in the PNN training for total porosity volume prediction.

		Predicted Lithology		
		Limestone	Dolomite	Shale
Lithology Logs	Limestone	**83.87%**	11.43%	4.35%
	Dolomite	7.08%	**81.95%**	4.63%
	Shale	5.19%	0.04%	**94.85%**

Table 1.3: Confusion matrix showing the match between the actual lithology (lithology logs) and the predicted lithology.

Chapter 2: Mapping seismic scale petrofacies variability in the Arbuckle Group for CO₂ sequestration using supervised machine learning: Wellington Field, Kansas*

*This chapter was presented as an invited talk at the 1st International Meeting for Applied Geoscience and Energy (IMAGE) conference in 2021:

Caf, A., B., D. Lubo-Robles, K. J. Marfurt, H. Bedle, M. J. Pranter, and D. Devegowda, 2021, Injectivity and Storage Potential Assessment of the Arbuckle Group for CO2 Sequestration via Supervised Neural Network: Wellington Field, Kansas, International Meeting for Applied Geoscience and Energy (IMAGE) Conference, Denver, CO, September 2021.

*This chapter will be submitted for publication in the journal, *Interpretation* in 2023.

Abstract

The Arbuckle Group in southern Kansas has recently been investigated for carbon geosequestration-related studies. In this study, we evaluated seismic-scale petrophysically defined facies variability of the Arbuckle Group at the Wellington Field, Kansas, using quantitative seismic interpretation and a supervised random forest classification approach. We first defined three petrophysics-based rock types (petrofacies) from core-derived porosity and permeability measurements using the flow-zone indicator (FZI) approach. Then, using the artificial neural network (ANN), we classified these petrofacies in non-cored intervals and a well. We observed that petrofacies 1 corresponds to medium and coarse-grained dolomitic packstone, wackestone, and dolomitic breccia with up to 8% porosity and Darcy-scale permeability values. Whereas petrofacies 2 and 3 correspond to argillaceous and fine-grained micritic dolomites and dolomitic mudstones with lower permeability values for a given porosity, with respect to petrofacies 1. Using the common reflection-point gathers, we performed pre-stack seismic inversion and calculated various amplitude-versus-offset (AVO) attribute volumes. We used these elastic properties and AVO attribute volumes as input for estimating supervised seismic-scale 3D petrofacies and petrofacies probability volumes using the Random Forest algorithm. Results reveal the heterogeneous distribution of the petrofacies in the study area. The workflow we present through this study can help reduce the uncertainty in the areas where well control is limited. Furthermore, the outputs of this study can be utilized as input in modeling and simulation studies by providing the seismic-scale spatial variability of petrofacies and petrophysical property trends, ultimately aiding more robust modeling of carbon dioxide plume behavior in the subsurface.

Introduction

Geologic carbon sequestration is one potential method for reducing atmospheric carbon dioxide (CO_2) levels. This process entails injecting and storing CO_2 into a deep saline aquifer or a depleted hydrocarbon reservoir (Gale, 2004; Friedmann, 2007; Breuning et al., 2013). Geophysical methods have been utilized for many geosequestration-related studies, including site characterization (Kazemeini et al., 2009, Sundal et al., 2016; DeAngelo et al., 2019; Fawad et al., 2021) and monitoring (Chadwick et al., 2010; Lumley, 2010; Li et al., 2013; Bergmann et al., 2014; Pires de Lima, 2019b; Fawad and Mondol, 2021). These studies mainly focused on monitoring the injected CO_2 plume in the subsurface, while relatively few studies were conducted on the characterization of candidate injection zones.

Among the many other variables, such as reservoir depth to keep the CO_2 supercritical and a confining zone that can trap the injected CO_2, a viable carbon geosequestration requires a reservoir with extensive storage capacity and injectivity (Rodosta et al., 2011; Goodman et al., 2011). Therefore, characterizing the spatial variability of storage capacity and the fluid-flow behavior is crucial for identifying optimal sites for CO_2 geosequestration.

The Arbuckle Group in southern Kansas and Oklahoma has become a focus for CO_2 sequestration-related studies due to its geological properties and the proximity to significant zones of CO_2 emission (Watney and Rush, 2012; Holubnyak, 2017). Numerous geophysical studies have been carried out to evaluate the CO_2 sequestration potential of the Arbuckle Group (Ohl and Raef, 2014; Gupta et al., 2017; Doveton and Watney, 2015). Ohl and Raef (2014) performed multi-attribute analysis and created porosity-related petrofacies clusters using an Artificial Neural

Network method (ANN). Gupta et al. (2017) utilized S-wave amplitude variation with offset to characterize possible fracture presence that can be a potential factor affecting the injectivity and CO_2 movement in the subsurface.

To build upon the previous studies, we assess the seismic-scale spatial variability of injectivity and storage potential of the heterogeneous Arbuckle Group by integrating petrophysics-defined rock types from cored wells with seismic data to create a 3D volume of petrofacies and individual petrofacies probabilities, using supervised machine learning.

The Wellington Field is in Sumner County, Kansas (Figure 2.1). Along with the Arbuckle Group, which is being targeted for CO_2 and wastewater injection, the primary unit of oil production of the study area are Mississippian-age carbonates that have produced 20 MMBO and are recently being targeted for enhanced-oil recovery- (EOR-) related CO_2 injection (Watney and Rush, 2012). Data for this study include a 3D seismic survey with pre-stack time migrated (PSTM) offset gathers covering a 12.6 mi^2 (~32.7 km^2) area. The seismic survey has a 2 ms sample rate and is processed with a bin size of 82.5 by 82.5 ft (25 by 25 m) and offset ranging from 456 to 6553 ft (~139 to 1998 m). The survey consists of 288 inlines and 178 crosslines and a record length of two seconds. The vertical seismic resolution (equal to one-fourth of a wavelength) at the interval of interest is 115 ft (~35 m). The dataset also includes two vertical wells, Berexco Wellington KGS #1–28 and #1-32. Both wells have a full suite of open-hole logs and the Berexco Wellington KGS #1–32 well also has 800 ft (~245 m) of core with petrophysical measurements and descriptions (Figures 2.2 and 2.3).

Core-derived porosity and permeability measurements were used to define petrophysics-defined rock types (petrofacies) for the cored well and classified in the uncored well using the

artificial neural network (ANN) method. Sonic and density logs from the two wells were used with seismic data used to generate synthetic seismograms to perform well-to-seismic ties. The seismic data were used to interpret key horizons and perform simultaneous pre-stack inversion for creating acoustic and shear impedance volumes. Additionally, angle stacks and amplitude-versus-offset (AVO) attribute volumes were produced. These seismic volumes and petrofacies logs were used to train a supervised Random Forest classifier to create a 3D volume of petrofacies and individual petrofacies probability volumes at a seismic scale. Finally, the resulting volumes were analyzed to evaluate the seismic-scale spatial distribution of potential injection and baffle zones in the Arbuckle interval in the study area (Figure 2.4).

Geological setting

The Wellington Field is in the southern portion of the Sedgwick Basin. The Sedgwick Basin is a major pre-Desmoinesian to post-Mississippian-age, shelf-like, southerly plunging feature in southwest Kansas. Structurally, it is bounded by the Central Kansas Uplift to the west, the Nemaha uplift to the east, the Salina Basin to the north, and the Anadarko Basin to the south (Merriam, 1963).

The Arbuckle Group is composed (bottom to top) of the Eminence Dolomite, Gasconade Dolomite with basal Gunther Sandstone, Robidoux Formation, and Jefferson City/Cotter Dolomite. The Arbuckle Group was mainly deposited in sub-tropical, intertidal to shallow subtidal environments within high salinity shallow continental seas (Merriam, 1963). Post-depositional dolomitization of the Arbuckle Group occurred when magnesium-rich fresh waters mixed with local marine waters. Along with dolomitization, hydrothermal alteration, karstification, and fracturing resulted in complex rock fabrics and a heterogeneous distribution of reservoir and non-

reservoir lithologies throughout the Arbuckle Group (Franseen et al., 2004). These lithologies are mainly boundstones, grainstones, packstones, and mudstones with various pore types, including intercrystalline, moldic, fenestral, and vuggy (Doveton and Watney, 2015). Except for certain structurally high regions on the Central Kansas uplift and the Nemaha anticline, where the Arbuckle has been eroded, the Arbuckle Group is regionally extensive across Kansas (Carr, 1986; Franseen et al., 2004). The average thickness increases from north to south, reaching approximately 1000 ft (~ 304 m) in south-central Kansas. Stratigraphically, the Arbuckle Group overlies the Precambrian granitic basement and the Reagan Sandstone and underlies the rocks of the Simpson Group (Figure 2.5). In the study area, the top of the Arbuckle Group is approximately 4000 ft (~1220 m) below the surface. Regarding the CO_2 geosequestration applications, this depth is well below the adequate depth (~2600 ft; 800 m) for injected CO_2 to stay in a supercritical state in the subsurface (Friedmann, 2007).

Methods

Lithologies and Petrophysics-based rock types (Petrofacies)

Lithologies were identified in the Arbuckle Group using detailed core descriptions by the Kansas Geological Survey (KGS) for the Berexco Wellington KGS #1–32 well. The descriptions identify lithologies and lithofacies through observations of composition, sedimentary structures, grain size, color, and diagenetic textures.

Several different methods of petrophysics-based rock-type classification methods have previously been introduced by authors such as Pitman (1992), Lucia (1995), Lee et al. (2002), Kaale (2010), and Gupta et al. (2017). In this study, we defined petrophysics-based rock types

(petrofacies) using the Flow Zone Indicator (FZI) approach (Amaefule et al., 1993). Using the core-derived porosity and permeability measurements. A petrofacies is a rock with similar pore geometry and fluid-flow characteristics that are internally consistent and different from adjacent rocks (Amaefule et al., 1993). When mapped with well and seismic data, petrofacies can help delineate the distribution of petrophysically unique rock types and associated storage capacity potential of the Arbuckle Group. The FZI method (Amaefule et al., 1993) is a technique based on the Kozeny-Carmen equation (Kozeny, 1927; Carmen, 1937) that identifies petrophysical hydraulic (fluid flow) units based on parameters such as grain surface area and tortuosity. Samples with similar FZI values will have similar pore geometry, sorting, diagenetic products, and grain size and exhibit similar fluid-flow characteristics. FZI is calculated using the following formulas:

$$RQI = 0.0314 * \sqrt{\frac{k}{\emptyset}} \tag{1}$$

$$R_{pvgv} = \frac{\emptyset}{1 - \emptyset} \tag{2}$$

$$FZI = \frac{RQI}{R_{pvgv}} \tag{3}$$

Where RQI is the reservoir quality index, k is the permeability (mD), $\emptyset$ is the porosity (fraction) and R_{pvgv} is the pore-to-grain volume ratio. On a log-log plot between RQI and R_{pvgv}, samples with different FZI values will lie on separate lines. To define the number of petrofacies, we applied FZI value cutoffs to cross plots of core-derived porosity and permeability. These cutoff values were determined by first defining initial cutoff values, then and analyzing petrophysical

properties of each petrofacies and adjusting the cutoff values accordingly until a sufficient contrast between petrofacies were achieved.

Petrofacies definition in the noncored well

To determine the petrofacies for the uncored intervals of the Berexco Wellington KGS #1-32 well and for the entire Arbuckle interval of the Berexco Wellington KGS #1-28 well, we used the electrofacies classification concept (Serra and Abbott, 1980). We utilized a supervised artificial neural network (ANN) to establish a relationship with the well-log signatures with corresponding petrofacies of the cored interval in the KGS Berexco #1-32 well and applied this relationship using the same well-log suite in the non-cored intervals to create a petrofacies log.

ANNs can be described as a type of mathematical algorithm that is inspired by the way human brain operates. A neural network learns from given data by forming a relationship between the petrofacies log and well-log signatures, trains the data to build specific patterns for each subject, and then predicts targets using the output model. The ANN achieves the prediction by minimizing the error between the actual and the estimated petrofacies logs through an iterative training process (Haykin, 2000). At each iteration, data is split into training and testing portions (%70-%30), where the first part is used to establish the relationships, while the remaining data is used for testing the accuracy. These samples were shuffled and resampled randomly in each iteration to ensure that the ANN training was not using the same portion of the data to learn the parameters of the prediction function. For the ANN training, the choice of input well logs were the photoelectric effect (PE), total porosity (PHIT), deep resistivity (RESD), and P-wave sonic (DT) logs. The total porosity (PHIT) logs were calculated by using neutron and density porosity logs with the given formula:

59

$$\emptyset_{total} = \sqrt{\frac{\emptyset_{neutron}^2 + \emptyset_{density}^2}{2}} \qquad (4)$$

To evaluate the performance of the ANN petrofacies classification, core-derived petrofacies logs were compared with the classified logs using a confusion matrix (Ting, 2011). A confusion matrix can be simply explained as a table that shows instances of the actual class in rows and instances of the predicted class in columns (Kohavi and Provost, 1998; Ting, 2011). Using the confusion matrix, two types of accuracy metrics were measured; individual petrofacies prediction accuracy was calculated by dividing the number of correct predictions by the total predictions for each petrofacies class. The overall accuracy is calculated by dividing all correct predictions by the number of classes.

Simultaneous pre-stack inversion

Using the simultaneous pre-stack inversion process, we generated acoustic and shear impedance volumes to be used as input feature volumes for the supervised random forest classifier. Seismic inversion produces "broadband" impedance values from the seismic reflection data. The goal of conducting seismic inversion is to derive quantitative measurements of subsurface parameters that relate to lithological and petrophysical properties (Chopra and Castagna, 2014). This method requires pre-stack gathers in the angle domain and initial 3D acoustic and shear impedance models. The model-based simultaneous inversion algorithm computes a synthetic offset seismic from the initial set of impedance models and the angle-dependent wavelets. To create the synthetic offset seismic data, the pre-stack inversion process utilizes the Fatti et al. (1994) variation of the Aki-Richards (1980) approximation of Zoeppritzs equations. The

difference between the synthetic and the actual seismic data is determined and iteratively updated until the synthetic seismic data best fits the observed seismic data, or a global minimum is achieved (Appendix A, Hampson et al., 2005; Veeken et al., 2007).

Prior to the pre-stack simultaneous inversion process, we pre-conditioned the seismic gathers by removing random noise and correcting for residual move-out errors. Then, we converted the offset gathers to the angle domain using the RMS velocity model. The viable incidence angle range of the study interval is between 2°- 30° (Appendix B). Once obtaining the pre-conditioned gathers, we then extracted the angle-depended wavelet group for near (2°-10°), mid (10°-20°), and far (20°-30°) angles from the seismic angle gathers. Using the near-angle wavelet, we performed well-to-seismic ties for both wells in the study by applying minor bulk shift, stretch, and squeeze to match the synthetic seismogram to the 2° angle trace (Figure 2.6).

To provide an initial solution for the inversion process and to compensate for the missing low-frequency part of the seismic spectrum, the low-frequency background models of P-impedance, S-impedance, and density were calculated by using the low-pass-filtered impedance and density logs from the wells with inverse-distance weighted interpolation within the Arbuckle Group (within the top and the base of the Arbuckle seismic horizons).

Seismic-scale 3D petrofacies volume prediction via supervised random forest classifier

Supervised machine learning methods have been widely used for rock type, lithology, and facies classification, and well-log property prediction problems (Hampson et al., 2001; Roy et al., 2014; Verma, 2016; Zhao et al., 2015; Gupta et al., 2018, 2020; Kim et al., 2019; Pires de Lima et al., 2019b; Caf and Pigott, 2021; Lubo-Robles et al., 2021, 2022, and many others).

In this study, we adopted the supervised Random Forest Classifier (Breiman, 2001, 2002; Liaw and Wiener, 2002; Scornet et al., 2015; Gender et al., 2017) to delineate the spatial variability of petrofacies at the seismic scale. The random forest method can be explained as an ensemble of decision trees that can be used for regression and classification tasks. For classification cases such as this study, the prediction is achieved by selecting the most prevalent class among all tree predictors.

To classify petrofacies, we used the petrofacies logs, P and S impedance volumes created by the pre-stack inversion process, AVO attributes such as Intercept and Gradient, and angle stacks as inputs.

The Random Forest training workflow in our study involves the creation of the training dataset, removing outliers, scaling, and hyperparameter optimization. To create the training dataset, first, we blocked the petrofacies logs in the time domain with the equal sampling rate as the seismic data (2 ms) (Appendix C). Then we extracted traces around the well locations, using a 5 by 5 sample window at each time sample from each input attribute. The size of the extraction window is based on geological insight, the number of wells, and the seismic bin size. In the training phase of the classifier, we used an 80-20 train-test split, where 80% of the samples belonged to training and the remaining 20% for validation. To overcome the possible bias related to the difference in units between the input features, we scaled our data using a Min-Max scaler approach (Jain et al., 2005; Pedregosa et al., 2011). To optimize our random forest training model, we optimized the hyperparameters using a random-search algorithm, where a combination of hyperparameters is randomly sampled from an initial grid space, reducing the computational cost (Bergstra et al., 2011; Bergstra and Bengio, 2012). To assess the model performance of the

optimized random forest model, we computed the average F1-score by dividing the total number

of true positive predictions by the total number of all false positive or false negatives predictions.

After training our Random Forest classifier model, we observed an average F-1 score of 86%

(Appendix D). We calculated a confusion matrix to quality control the petrofacies prediction

results and evaluate the principal assumption of class independence, we calculated a confusion

matrix. Finally, we applied the trained random forest model to our input attributes to predict the

3-D volume of rock types and associated probability volumes.

Results

Lithologies and Petrofacies

The Arbuckle Group in the study area consists primarily of nine lithologies: (1) Peloidal

dolomitic packstone, (2) Argillaceous dolomitic packstone, (3) Argillaceous micritic dolomite, (4)

Crystalline dolomite, (5) Crystalline micritic dolomite, (6) Dolomitic breccia, (7) Dolomitic

mudstone, (8) Fine-grained dolomitic packstone, and (9) Medium-grained dolomitic wackestone

(Figure 2.7). Using the FZI method, we defined three petrofacies for the Arbuckle Group (Figure

2.8). Petrofacies 1 exhibits the highest permeability values (up to Darcy-scale) for a given porosity,

and low acoustic and shear impedance values ($Z_p = 48000, Z_s = 27000$ ft/s*g/cc). In contrast,

petrofacies 3 has the lowest range of permeability (<0.2-20 mD) for a given porosity value and

high impedance values ($Z_p = 58000, Z_s = 32000$ ft/s*g/cc). Petrofacies 2 has porosity,

permeability, and elastic values that are in between petrofacies 1 and 3. Petrofacies 1 corresponds

to medium-grained peloidal dolopackstone, medium and coarse-grained dolowackestone, and

dolomitic breccia. Petrofacies 2 corresponds to argillaceous dolomitic packstone, fine-grained

micritic dolomites, and dolomitic mudstone, and petrofacies 3 corresponds to crystalline dolomite and argillaceous micritic dolomites.

ANN Petrofacies estimation for the noncored well (Berexco Wellington KGS #1-28) yielded relatively high individual and overall accuracies. The overall accuracy is 85%. Individual petrofacies prediction accuracies are 81%, 89%, and 82%, respectively (Figure 2.9 and Table 2.1).

Seismic-scale elastic property and petrofacies distribution

To quality control the pre-stack inversion results, we show the comparison between the inverted well logs and seismic gathers with the original input data (Figure 2.10). A good correlation (90%) between inverted and actual properties can be observed. Qualitative evaluation of impedance inversion results indicate that the inversion accurately estimated the elastic properties at the well locations (Figure 2.11). The results also show that the middle portion of the Arbuckle interval can be seen with high acoustic and shear impedance values. In contrast, relatively lower values of impedances are primarily located in the lower and the upper portion.

The supervised random forest classification results include one classification volume corresponding to the most likely petrofacies prediction and three volumes corresponding to the probability for each petrofacies at each seismic voxel. The predictive capability and uncertainty range of the 3D petrofacies prediction process is illustrated in a confusion matrix (Table 2.2). The matrix shows that the individual petrofacies prediction was achieved with 83.3%, 87%, and 84% accuracies, for petrofacies 1, 2, and 3, respectively. The overall prediction accuracy is 85%.

To evaluate the spatial distribution of petrofacies within the Arbuckle Group, we display the petrofacies prediction results on vertical sections and maps. The petrofacies cross-section

illustrates the stratigraphic and lateral variability of the Arbuckle strata. Porous and permeable petrofacies 1 is mostly concentrated at the lower and the upper portion of the Arbuckle Group, while the tight and impermeable petrofacies 3 can be observed in the middle part of the Arbuckle interval (Figure 2.12). Additionally, Petrofacies distribution is relatively continuous in the southeastern portion, gradually increasing lateral variability towards the northeast.

To show the uncertainty associated with the petrofacies prediction, we show arbitrary lines through individual petrofacies probability volumes (Figure 2.13a-c). High probability values (up to 87%) for petrofacies 1 are observed in the lower and the upper part of the zone of interest (Figure 2.13a). Similarly, we obtained high probabilities of petrofacies 2 and 3 in the middle Arbuckle interval.

Figures 2.14a through c show the petrofacies values extracted onto proportional slices, showing the spatial variability of petrofacies corresponding to the lower, middle, and upper Arbuckle intervals, respectively. The map extracted on the lower portion of the Arbuckle shows that the interval mainly consists of petrofacies 1, which was previously defined as the petrofacies with high porosity and permeability values. The map also shows that petrofacies 1 is mainly concentrated around the central and southern portions of the study area. The middle Arbuckle map reveals that the interval is dominated primarily by the petrofacies 2 and 3, described previously as the lower permeability petrofacies. In this interval, petrofacies 3 becomes more dominant towards the southeast. The horizon slice corresponding to the upper Arbuckle section is mainly composed of petrofacies 1 and 2, whereas the petrofacies 1 composition is mainly dominant towards the northeast.

Discussion

The integration of core-derived petrophysical-property measurements and seismic information helped to identify highly heterogeneous petrofacies variability within the Arbuckle Group at the seismic scale. This heterogeneity can be interpreted as the imprint of the complex distribution of pore structure, which resulted from depositional and diagenetic processes.

To compare the rock-type classification workflow of this study with previous work, Ohl et al. (2014) utilized map-based supervised classification using a neural network approach with various post-stack seismic attributes and well log rock-types as an input. Rock- type classes were created based on arbitrary neutron-porosity cut-offs (e.g., low, medium, and high neutron porosity). The resulting rock-type map shows the spatial variability only in two dimensions at the horizon corresponding to the top of the Arbuckle Group. Additionally, rock types defined in this study defined based on a single well log, without any correlation to the lithology and corresponding petrophysical properties.

Watney and Rush (2012) created their rock type model by first creating geostatistical models of porosity and permeability and then arbitrarily defining rock types by binning associated reservoir quality index (RQI) values.

In this study, petrofacies are defined based on core porosity and permeability using the FZI method. Each petrofacies also relates to core-defined lithofacies. To link petrofacies to seismic elastic properties and angle dependent attributes, we utilized the supervised random forest classifier. The resulting volume provides a three-dimensional petrofacies volume and associated prediction uncertainty information away from wells. The petrofacies correspond to both lithofacies

and petrophysical properties of the Arbuckle Group. The stratigraphic and lateral variability of petrofacies from this method establishes distinct reservoirs zones for both subsurface injection and storage and fluid-flow barriers. Therefore, the petrofacies volume is useful as 3D facies trend volume for static and dynamic modeling.

Limitations

While this workflow achieves high performance for predicting the petrofacies within the study area, some limitations are present: In this study, there were only two wells fully penetrating the Arbuckle interval. Therefore, both wells were used to train the random forest algorithm, without additional well (or wells) to evaluate the performance of the model in the presence of test data (data that was not used for training). Moreover, due to the limited number of wells, the amount of training samples is limited. These limitations were challenging for application of other supervised classification methods such as neural networks. Therefore, we utilized the random forest method, since it is known for generating robust results without overfitting the training data, needing only a small number of hyperparameters to be tuned and most importantly, its ability to work with a weak input data, where there is a small number of input samples to distinguish between classes (Breiman, 2001; Liaw and Wiener, 2002; Scornet et al., 2015). Additionally, to further overcome the sampling related issue, we used number of traces around each well (from each input feature volume) using a 5 by 5 sample window, augmenting the number of training samples. The size of the window is selected after analyzing the input feature variability with the distance from wells, in order to ensure that there is no significant change in the geological character within the sample extraction window.

Conclusions

The Arbuckle Group in the Wellington Field can be represented by three petrophysics-based rock types (petrofacies) based on the core-derived porosity and permeability measurements using the FZI method. The petrofacies correspond to lithologies varying from (1) medium and coarse-grained peloidal dolo packstone, wackestone, and dolomitic breccia. (2) Argillaceous dolomitic packstone, fine-grained micritic dolomite, and dolomitic mudstone, and (3) crystalline dolomite and argillaceous micritic dolomite. To map the petrofacies in three dimensions at the seismic scale, we successfully applied the supervised random forest classifier algorithm using the petrofacies logs, elastic property, and angle-dependent seismic volumes. The random forest algorithm achieved an 86% average F1 score for predicting the petrofacies. As a result of this process, we have estimated petrofacies and individual petrofacies probabilities at each seismic voxel. The resulting 3D petrofacies volume reveals that the petrofacies corresponding to the highest permeability and porosity are in the lower and upper portions of the Arbuckle, and low porosity and permeability rocks are in the middle Arbuckle interval. Results also reflect the heterogeneous spatial distribution of petrofacies, revealing the complexity of the porosity, permeability, and fluid flow characteristics within the Arbuckle Group. Additionally, the workflow suggested in this study can be helpful by bridging the gap between and away from the wells and reduce the uncertainty in the areas where the well control is limited. Furthermore, outputs of this study can be used as spatial trend volumes in seismic-constrained static modeling and dynamic simulation workflows for modeling the behavior of CO_2 plumes in the subsurface.

Acknowledgments

References

Aki, K., and P. G. Richards, 1980, Quantitative Seismology-Theory and methods: W. H. Freeman.

Amaefule, J. O., M. Altunbay, D. Tiab, D. G. Kersey, and D. K. Keelan, 1993, Enhanced reservoir description: Using core and log data to identify hydraulic (flow) units and predict permeability in uncored intervals/ wells: 68th Annual Technical Conference and Exhibition, SPE, Extended Abstracts, SPE-26436-MS, doi: 10.2118/26436-MS.

Bergmann, P., M. Ivandic, B. Norden, C. Rücker, D. Kiessling, S. Lüth, C. Schmidt-Hattenberger, and C. Juhlin, 2014, Combination of seismic reflection and constrained resistivity inversion with an application to 4D imaging of the CO2 storage site, Ketzin, Germany, Geophysics, 79, no. 2, B37–B50, doi: 10.1190/geo2013-0131.1.

Bergstra, J., R. Bardenet, Y. Bengio, and B. Kégl, 2011, Algorithms for hyper-parameter optimization: 24th International Conference of Neural Information Processing Systems, 2546-2554.

Bergstra, J., and Y. Bengio, 2012, Random Search for Hyper-Parameter Optimization: Journal of
Machine Learning Research, 13, 281-305.

Breiman, L., 2001, Random forests: Machine Learning, 45, 5–32, doi: 0.1023/A:1010933404324.

Breiman, L., 2002, Manual on setting up, using, and understanding random forests v3.: Statistics
Department University of California.

Breunig, H. M., J. T. Birkholzer, A. Borgia, C. M. Oldenburg, P. N. Price, and T. E., McKone
2013, Regional evaluation of brine management for geologic carbon sequestration,
International Journal of Greenhouse Gas Control, 14, 39–48, doi:
10.1016/j.ijggc.2013.01.003.

Caf, A., B., and J. D. Pigott, 2021, Dolomitization geometry and reservoir quality from
supervised Bayesian classification and probabilistic neural networks: Midland Basin
Leonardian Wichita and Clear Fork Formations, Interpretation, 9, no. 2, T585-T598,
doi:10.1190/INT-2020-0204.1.

Campbell, J. A., C. J. Mankin, A. B. Schwarzkopf, and J. J. Raymer, 1988, Habitat of petroleum
in Permian rocks of the Midcontinent region; in, Permian Rocks of the Midcontinent, W.
A. Morgan and J. A. Babcock, eds.: Midcontinent Society of Economic Paleontologists
and Mineralogists, Special Publication No. 1, 13–35.

Carmen, P.E,1937, Fluid Flow through Granular Beds, Trans. AIChE v. 15, 150 -166.

Carr, J., E., H. E. McGovern, T. Gogel, and J. H. Doveton, 1986, Geohydrology of and potential for fluid disposal in the Arbuckle Aquifer in Kansas. U.S. Geological Survey open-file report, 86-491, doi: 10.3133/ofr86491.

Carr, T. R., D. F. Merriam, and J. D. Bartley, 2005, Use of relational databases to evaluate regional petroleum accumulation, groundwater flow, and CO2 sequestration in Kansas, AAPG Bulletin, 89 no. 12, 1607–1627, doi:10.1306/07190504086.

Chadwick, A., G. Williams, N. Delepine, V. Clochard, K. Labat, S. Sturton, M. Buddensiek, M. Dillen, M. Nickel, M., A. L. Lima, R. Arts, F. Neele, and G. Rossi, 2010, Quantitative analysis of time-lapse seismic monitoring data at the Sleipner CO2 storage operation, The Leading Edge, 29, 170–177, doi: 10.1190/1.3304820.

Chopra, S., and J. P. Castagna, 2014, AVO. Soc. Of Exploration Geophysicists.

DeAngelo, M. V., R. Fifariz, T. Meckel, R. H. Treviño, 2019, A seismic-based CO2-sequestration regional assessment of the Miocene section, northern Gulf of Mexico, Texas and Louisiana, International Journal of Greenhouse Gas Control, International Journal of Greenhouse Gas Control, 81, 29-37,1750-5836, doi: 10.1016/j.ijggc.2018.12.009.

Doveton, J., and L. Watney, 2015, Textural and pore size analysis of carbonates from integrated core and nuclear magnetic resonance logging: An Arbuckle study, Interpretation 3, SA77-SA89, doi: https://doi.org/10.1190/INT-2014-0050.1

Dutton, S. P., 1984, Fan-Delta Granite Wash of the Texas Panhandle: Oklahoma City Geological Society, Short Course Notes, 1–44.

Fatti, J. L., G. C. Smith, P. J. Vail, P. J. Strauss, and P. R. Levitt, 1994, Detection of gas in sandstone reservoirs using AVO analysis: A 3-D seismic case history using the geostack technique: Geophysics, 59, no. 9, 1362–1376, doi: 10.1190/1.1443695.

Fawad, M., MD. J. Rahman, and N. H. Mondol, 2021, Seismic reservoir characterization of potential CO2 storage reservoir sandstones in Smeaheia area, Northern North Sea, Journal of Petroleum Science and Engineering, 205, 108812, doi: 10.1016/j.petrol.2021.108812.

Friedmann, S. J., 2007, Geological carbon dioxide sequestration: Elements, 3, 179–184, doi:10.2113/gselements.3.3.179.

Franseen, E. K., A. P. Byrnes, J. R. Cansler, D. M. Steinhauff, and T. R. Carr, 2004, The geology of Kansas – Arbuckle group: Current Research in Earth Sciences, Kansas Geological Survey Bulletin 250, part 2, http://www.kgs.ku.edu/Current/2004/franseen/index.html (Accessed February 2021).

Friedmann, S. J., 2007, Geological carbon dioxide sequestration: Elements, 3, 179–184, doi: 10.2113/gselements.3.3.179.

Gale, J., 2004, Geological storage of CO2: What do we know, where are the gaps and what more needs to be done? Energy, 29, 1329–1338, doi: 10.1016/j.energy.2004.03.068.

Genuer, R., J-M. Poggi, C. Tuleau-Malot, and N. Villa-Vialaneix, 2017, Random Forests for Big Data: Big Data Research, 9, 28-46.

Goodman, A., A. Hakala, G. Bromhal, D. Deel, T. Rodosta, S. Frailey, M. Small, D. Allen, V. Romanov, J. Fazio, N. Huerta, D. McIntyre, B. Kutchko, and G. Gutherie, 2011, US DOE

methodology for the development of geologic storage potential for carbon dioxide at the national and regional scale, Int. J. Greenhouse Gas Control, 5, 952-965, doi: 10.1016/j.ijggc.2011.03.010.

Gupta, M., K. Spikes, and B. Hardage, 2017, Characterization of naturally fractured Arbuckle Group in the Wellington Field, Kansas, using S-wave amplitude variation with offset, Interpretation 5, T49-T63, doi: 10.1190/INT-2016-0061.1.

Gupta, I., C. H. Sondergeld, C. Rai, and D. Devegowda, 2017, Rock typing in Wolfcamp formation: 58th SPWLA Annual Logging Symposium, SPWLA-2017-D.

Gupta, I., C. Rai, D. Devegowda, and C. Sondergeld, 2018, Use of data analytics to optimize hydraulic fracture locations along borehole: Petrophysics, 59, 811–825, doi: 10.30632/PJV59N6-2018a6.

Gupta, I., N. Tran, D. Devegowda, V. Jayaram, C. Rai, C. Sondergeld, and H. Karami, 2020, Looking ahead of the bit using surface drilling and petrophysical data: Machine-learning-based real-time geosteering in volve field, SPE J. 25 (2): 990–1006, doi:10.2118/199882-PA.

Hampson, D. P., J. S. Schuelke, and J. A. Quirein, 2001, Use of multiattribute transforms to predict log properties from seismic data, Geophysics, 66, 220–236, doi: 10.1190/1.1444899.

Hampson, D. P., B. H. Russell, and B. Bankhead, 2005, Simultaneous inversion of pre-stack seismic data: 75th Annual International Meeting, SEG, Expanded Abstracts, 1633–1638, doi: 10.1190/1.2148008.

Haykin, S., 2000, Neural networks: A guided tour. Nonlinear Biomedical Signal Processing, 1, 53-68.

Holubnyak, Y., E. Williams, L. Watney, T. Bigdoli, J. Rush, M. Fazelalavi, and P. Gerlach, 2017, Calculation of CO2 Storage Capacity for Arbuckle Group in Southern Kansas: Implications for a Seismically Active Region, Energy Procedia, 114, 4679-4689, doi: 10.1016/j.egypro.2017.03.1599.

Jain, A., K. Nandakumar, and A. Ross, 2005, Score normalization in multimodal biometric systems: Pattern Recognition, 38, no. 12, 2270-2285, doi: 10.1016/j.patcog.2005.01.012.

Johnson, K. S., and K. V. Luza, 2008, Earth sciences and mineral resources of Oklahoma: Oklahoma Geological Survey, Educational Publication 9, 1–22.

LoCricchio, E., 2012, Wash Play Overview, Anadarko Basin: Stratigraphic framework and controls on Pennsylvanian granite wash production, Anadarko Basin, Texas and Oklahoma: AAPG Search and Discovery Article #110163.

Kale, S., C. Rai, and C. H. Sondergeld, 2010, Rock typing in gas shales: 85th Annual Technical Conference and Exhibition, SPE, Extended Abstracts, SPE-134539-MS, doi: 10.2118/134539-MS

Kazemeini, S. H., C. Juhlin, K. Zinck-Jorgensen, and B. Norden, 2009, Application of the continuous wavelet transform on seismic data for mapping of channel deposits and gas detection at the CO2SINK site, Ketzin, Germany, Geophysical Prospecting, 57, 111–123, doi: 10.1111/j.1365-2478.2008.00723.x.

Kim, Y., R. Hardisty, and K. J. Marfurt, 2019, Attribute selection in seismic facies classification: Application to a Gulf of Mexico 3D seismic survey and the Barnett Shale, Interpretation 7, no. 3, SE281-SE297, doi: 10.1190/INT-2018-0246.1.

Kohavi, R., and F. Provost, 1998, Special issue on applications of machine learning and the knowledge discovery process: Kluwer Academic Publishers, Boston, 271 p.

Kozeny, J.: "Uber Kapillare Leitung des Wassel'S im Boden, Sitzungsberichte," Royal Academy of Science, Vienna, Proc. Class I (1927) v. 136,271-306.

Lee, S. H., A. Kharghoria, and A. Dutta-Gupta, 2002, Electrofacies characterization and permeability prediction in complex reservoirs, SPE Reservoir Evaluation and Engineering, 5, 237–248, doi: 10.2118/78662- PA.

Li, J., C. Liner, P. Geng, and J. Zeng, 2013, Convolutional time-lapse seismic modeling for CO2 sequestration at the Dickman oilfield, Ness County, Kansas, GEOPHYSICS, 78, no. 3, B147–158, doi:10.1190/geo2012-0159.1.

Liaw, A., and M. Wiener, 2002, Classification and regression by Random Forest, *R news*, *2*(3), 18-22.

Lucia F. J., 1995, Rock-fabric/petrophysical classification of carbonate pore space for reservoir characterization, AAPG Bulletin, 79, no. 9, 1275–1300, doi: 10.1306/7834D4A4-1721-11D7-8645000102C1865D.

Lubo-Robles, D., T. Ha, S. Lakshmivarahan, K. J. Marfurt, and M. J. Pranter, 2021, Exhaustive probabilistic neural network for attribute selection and supervised seismic facies classification, Interpretation 9, no. 2, T421-T441, doi:10.1190/INT-2020-0102.1.

Lubo-Robles, D., D. Devegowda, V. Jayaram, H. Bedle, K. J. Marfurt, and M. J. Pranter, 2022, Quantifying the sensitivity of seismic facies classification to seismic attribute selection: An explainable machine learning study, Interpretation, 10:3, SE41-SE69, doi: 10.1190/INT-2021-0173.1.

Lumley, D., 2010, 4D seismic monitoring of CO2sequestration, The Leading Edge, 29, 150–155, doi: 10.1190/1.3304817.

McConnell, D. A., M. J. Goyda, G. N. Smith, and J. P. Chitwood, 1989, Morphology of the frontal fault zone, southwest Oklahoma: Implications for deformation and deposition on the Wichita Uplift and Anadarko Basin: Geology, 18, no. 7, 34–637.

Merriam, D., F., 1963, The geologic history of Kansas: Kansas Geological Survey Bulletin, v. 162, 317 p.

Northcutt, R. A., and J. A. Campbell, 1995, Geology provinces of Oklahoma: Oklahoma Geological Survey Open-File Report 5–95.

Ohl, D., and A. Raef, 2014, Rock formation characterization for carbon dioxide geosequestration: 3D seismic amplitude and coherency anomalies, and seismic petrophysical facies classification, Wellington and Anson-Bates Fields, Kansas, USA, Journal of Applied Geophysics, 103, 221–231, doi: 10.1016/j.jappgeo.2014.01.017.

Pedregosa F., G. Varoquaux, A. Gramfort, V. Michel, B. Thirion, O. Grisel, M. Blondel, P. Prettenhofer, R. Weiss, V. Dubourg, J. Vanderplas, A. Passos, D. Cournapeau, M. Brucher, M. Perrot, and E. Duchesnay, 2001, Scikit-learn: Machine Learning in Python: Journal of Machine Learning Research, 12, 2825-2830.

Pires de Lima, R., F. Suriamin, K. J. Marfurt, and M. J. Pranter, 2019a, Convolutional neural networks as aid in core lithofacies classification, Interpretation, 7, no. 3, SF27–SF40, doi: 10.1190/INT-2018-0245.1.

Pires de Lima, R., and Y. Lin, 2019b, Geophysical data integration and machine learning for multi-target leakage estimation in geologic carbon sequestration, 89th Annual International Meeting, SEG, Expanded Abstracts, 2333-2337, doi: 10.1190/segam2019-3215405.1.

Pittman, E. D., 1992, Relationship of porosity and permeability to various parameters derived from mercury injection – Capillary pressure curves for sandstones: AAPG Bulletin, 76, 191–198, doi: 10.1306/BDFF87A4- 1718-11D7-8645000102C1865D.

Rodosta, T. D., J.T. Litynski, S.I. Plasynski, S. Hickman, S. Frailey, and L. Myer, 2011, U.S. Department of Energy's site screening, site selection, and initial characterization for storage of CO2 in deep geological formations, USGS Publications Warehouse, doi: 10.1016/j.egypro.2011.02.427.

Roy, A., A. S. Romero-Peláez, T. Kwiatkowski, and K. J. Marfurt, 2014, Generative topographic mapping for seismic facies estimation of a carbonate wash, Veracruz Basin, southern Mexico: Interpretation, 2, no. 1, SA31–SA47, doi: 10.1190/INT-2013-0077.1.

Scheffer, A., 2012, Geochemical and microbiological characterization of the Arbuckle saline aquifer, a potential CO2 storage reservoir; Implications for hydraulic separation and caprock integrity: M.S. thesis, University of Kansas.

Scornet, E., G. Biau, and J-P. Vert, 2015, Consistency of random forests: Annals of Statistics, Institute of Mathematical Statistics (IMS), 43, no. 4, 1716-1741, doi: 10.1214/15-AOS1321.

Sundal, A., J. P. Nystuen, K-L. Rørvik, H. Dypvik, and P. Aagaard, 2016, The Lower Jurassic Johansen Formation, northern North Sea-Depositional model and reservoir characterization for CO2 storage, Marine and Petroleum Geology, 77, 1376-1401, doi: 10.1016/j.marpetgeo.2016.01.021.

Ting, K. M., 2011, Confusion matrix, in C. Sammut and G.I. Webb, eds., Encyclopedia of machine learning, 1st ed: New York, Springer, 209 p.

Veeken, P. C.H., 2007, Handbook of Geophysical Exploration – Seismic Stratigraphy, Basin Analysis and Reservoir Characterization, Volume 37. Elsevier.

Verma, S., T. Zhao, K. J. Marfurt, and D. Devegowda, 2016, Estimation of total organic carbon and brittleness volume, Interpretation 4: T373-T385, doi: 10.1190/INT-2015-0166.1.

Watney, W. L., and J. Rush, 2012, Small scale field test demonstrating CO2 sequestration in Arbuckle Saline Aquifer and by CO2-EOR at Wellington Field, Sumner County, Kansas: DOE Project Number DE-FE0006821.

Watney, W., L., J. Rush, M. Dubois, R. Barker, T. Birdie, K. Cooper, S. Datta, J. Doveton, M. Fazelalavi, D. Fowle, P. Gerlach, T. Hansen, D. Hedke, Y. Holubnyak, B. Huff, K. D. Newell, L. Nicholson, J. Roberts, A. Scheffer, A. Sirazhiev, R. Sorenson, G. Tsoflias, E. Williams, D. Wreath and J. Youle, 2013, Evaluating CO_2 utilization and storage in Kansas, AAPG Search and Discovery Article 80337, Accessed December 1, 2021, https://www.searchanddiscovery.com/documents/2013/80337watney/ndx_watney.pdf

Zhao, T., V. Jayaram, A. Roy, and K. J. Marfurt, 2015, A comparison of classification techniques for seismic facies recognition: Interpretation, 3, no. 4, SAE29–SAE58, doi: 10.1190/INT-2015-0044.1.

Appendix A

Pre-stack simultaneous inversion

The commercial software used for the pre-stack simultaneous inversion utilizes the re-expression of Aki-Richard's (2002) equation created by Fatti et al. (1994):

$$R(\theta) \approx 1 + tan^2\theta R_p + -8\,(V_s/V_p)^2\,tan^2\theta R_s + -0.5tan^2\theta + 2\,(V_s/V_p)^2\,sin^2\theta R_D, \qquad \text{(A-1)}$$

Where, $R_p = \frac{1}{2}\left[\frac{\Delta V_p}{V_P} + \frac{\Delta\rho}{\rho}\right]$, $R_s = \frac{1}{2}\left[\frac{\Delta V_s}{V_s} + \frac{\Delta\rho}{\rho}\right]$, and $R_\rho = \frac{\Delta\rho}{\rho}$. $\qquad\qquad$ (A-2)

R_p, R_s and R_ρ Represents angle-depended P-wave, S-wave, and density reflectivities, respectively.

When the zero-offset forward model (Hampson et al., 2005) equation (which relates the seismic trace to the logarithm of the P-impedance) is extended to an angle-dependent trace using the Fatti's equation, it yields:

$$T(\theta) = \frac{1}{2}c_1 + \frac{1}{2}kc_2 + mc_3(\theta)D\ln(Z_p) + \frac{1}{2}c_2W(\theta)D\,\Delta\ln(Z_s) + W(\theta)c_3D\Delta\ln(\rho) \qquad \text{(A-3)}$$

$W(\theta)$ Represents angle-dependent wavelet, and D is the derivative operator. The commercial software uses the linear relationship between $\ln Z_p$ and $\ln Z_s$ and $\ln Z_p$ and $\ln(\rho)$ in logarithmic space to solve for $\Delta\ln(Z_s)$ and $\Delta(\ln\rho)$, which are fluid anomalies separated from the background wet trend (Hampson et al., 2005):

$$\ln(Z_s) = k\ln(Z_p) + k_c + \Delta\ln(\rho) \qquad\qquad\qquad\qquad\qquad\qquad \text{(A-4)}$$

$$\ln(\rho) = m\ln(Z_p) + m_c + \Delta\ln(\rho) \qquad\qquad\qquad\qquad\qquad\qquad \text{(A-5)}$$

The coefficients k and m are supplied by the user input by fitting the best line at crossplots of $\ln(\rho)$ vs $\ln(Z_p)$, and $\ln(Z_p)$ vs $\ln(Z_s)$. The inversion for P-impedance, S-impedance, and density is achieved by solving equation B-3 by matrix inversion methods. To initialize the solution, the software uses the low-frequency background models (of P impedance, S impedance, and density) and iterates toward a solution using the conjugate gradient method.

Appendix B

Pre-stack gather pre-conditioning

Prior to pre-stack simultaneous inversion and angle-dependent seismic volumes calculation (angle stacks and AVO attributes), seismic gathers were pre-conditioned due to coherent (ground roll, multiples, etc.) and incoherent random noise present in the seismic data.

The conditioning workflow followed in this study involves parabolic Radon Filtering, applying angle mute, and creating final angle gathers.

Parabolic Radon filtering

The algorithm in the commercial software used in this process is set to identify the long-period multiples and the random noise within the data. Based on the parameters defined by the user, the software creates a model of primary reflection events and noise. After the model is created, the software then subtracts the model of these multiples and the random noise from the data.

This data are modeled using a Radon transform that assumes that the coherent data within a pre-stack gather can be modeled as a linear combination of constant amplitude parabolic events. Since the transform is applied to the NMO-corrected data, the primary P-wave events have a moveout of about 0 ms, while slower multiples and converted waves will have greater moveouts. These larger moveout events are then used to generate a model of the coherent noise which is then subtracted from the input gather giving the result seen in Figure B-1.

The critical element in this filtering process is defining the range of the move-out values for the artifacts and the number of parabolas for the noise modeling. The first part is done by visually inspecting the input gather and determining the range of move-outs. Once the range is defined, the number of parabolas can be calculated based on the rule that at least one parabola is needed to model each half-wavelength at the farthest offset. To fine-tune the filtering parameters and QC the results, the filtering process was done iteratively by perturbing the parameters at each step and inspecting the rejected noise and the output. Figure B.1 shows the result of the parabolic Radon filtering where the random and coherent noise is eliminated, and no artifacts were artificially created at the filtered gather.
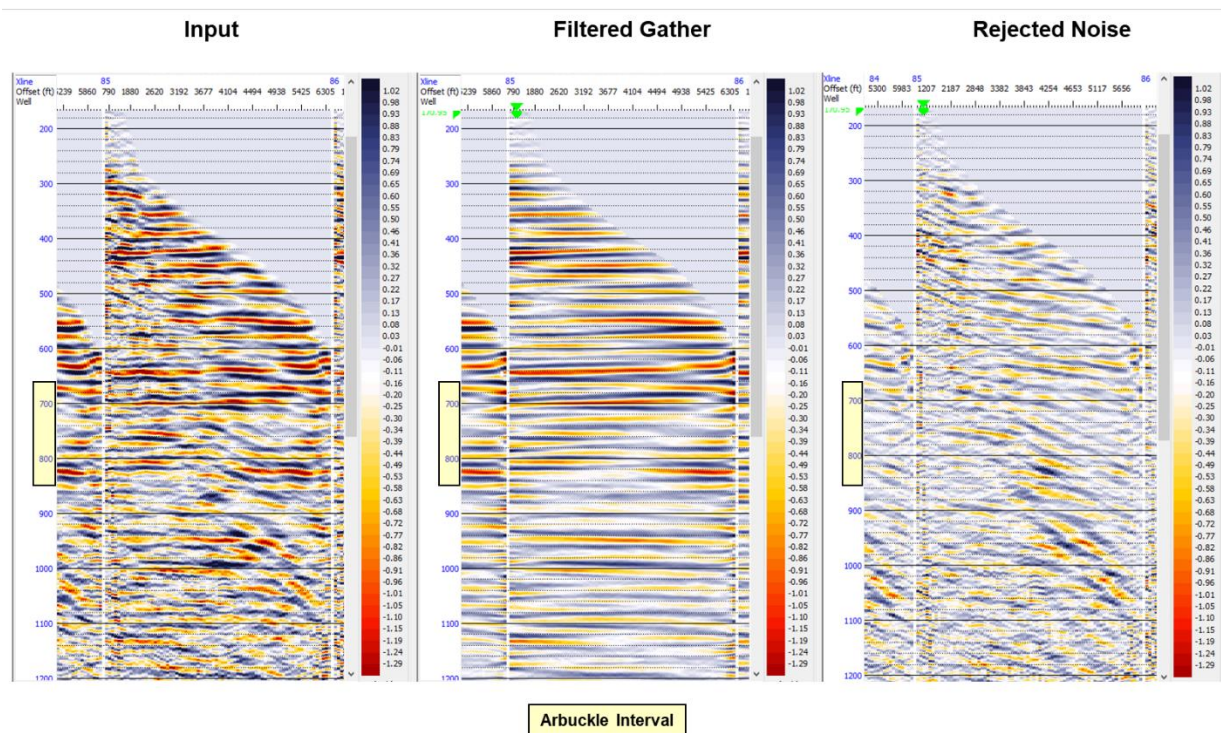
Figure 2-B. 1: Pre-stack gathers before the conditioning (left image), conditioned gathers (middle image), and the noise subtracted from the original data (right image).

83

Angle gather calculation

As the last step in the gather pre-conditioning, 30^0 angle mute was applied to the radon-filtered gathers, and angle gather was calculated to convert the gathers from offset to the incident angle domain (Figure A-2) to be used in the pre-stack simultaneous inversion process. This calculation was done by Ray Tracing Method using the RMS velocity information to map each sample to its corresponding incident angle by the equation below:

$$tan\ \theta = \frac{X}{V_{RMS*t_0}} \tag{A-1}$$

Where θ is the incidence angle, and X equals the offset, and V_{RMS} Is the RMS velocity and t_0 zero-offset travel time. For this study, the angle gathers were created by binning the traces into 10 angle bins ranging from 0 to 30 degrees. Figure A-3 shows the angle muting process, and the final angle gather output.
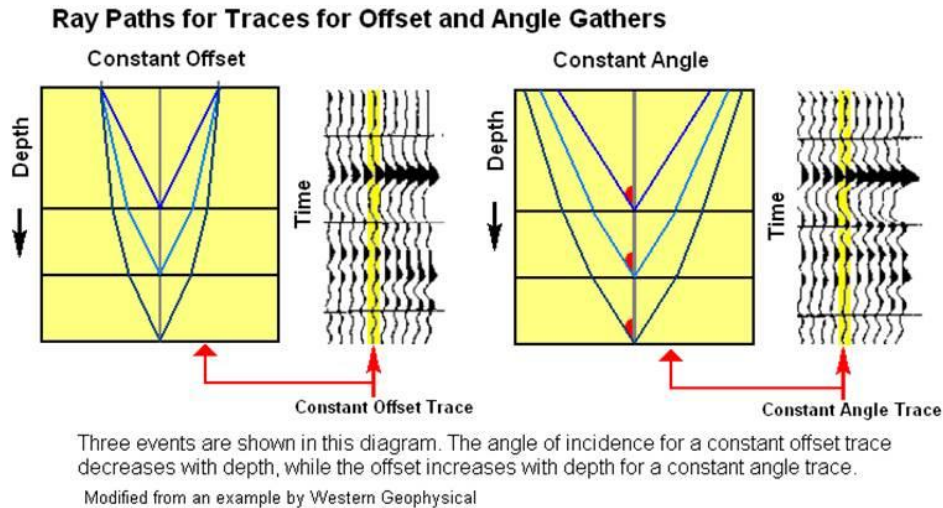
Figure 2-B. 2: Offset to incidence angle conversion (Taken from CGG Geoview software manual).
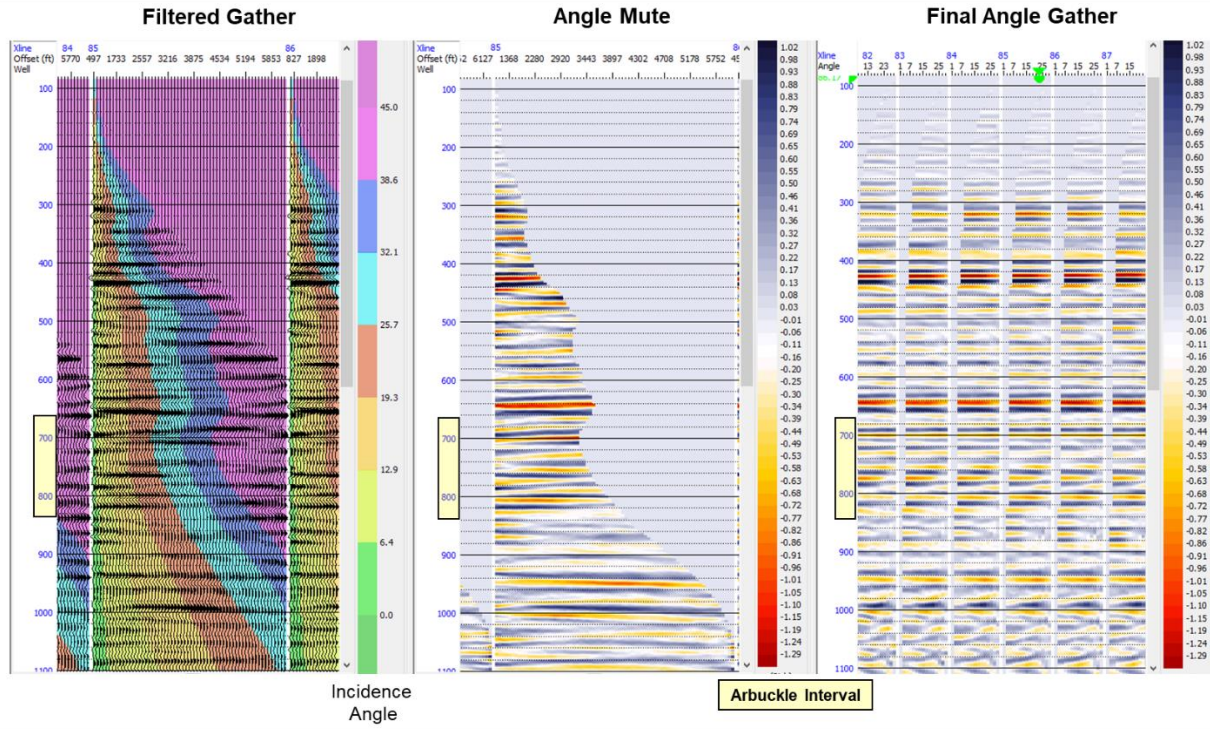
Figure 2-B. 3: Conversion of conditioned gathers from offset to incidence angle domain and angle gather (right image) calculation.

Appendix C

Resampling petrofacies logs in the time domain
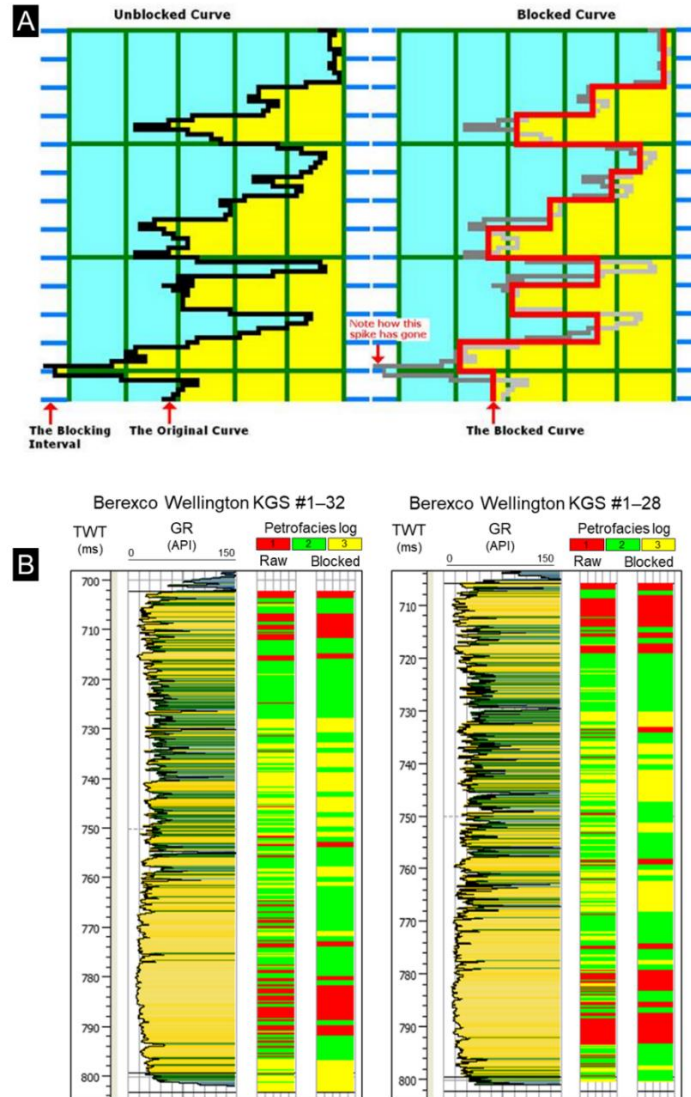
Figure 2-C. 1: The example of the log blocking workflow used to upscale the petrofacies logs in the time domain. (A) schematic display of the blocking method utilized in the commercial software. Petrofacies logs were blocked at a uniform increment defined by the user. The mean value of each block will replace the value at each sample in the block (taken from the CGG Geoview software help database). (B) Petrofacies log upscaling results compared to the raw petrofacies logs. Logs were upscaled in the time domain by a block size equal to the seismic sampling interval (2ms).

Appendix D

Hyperparameter optimization for the supervised random forest training
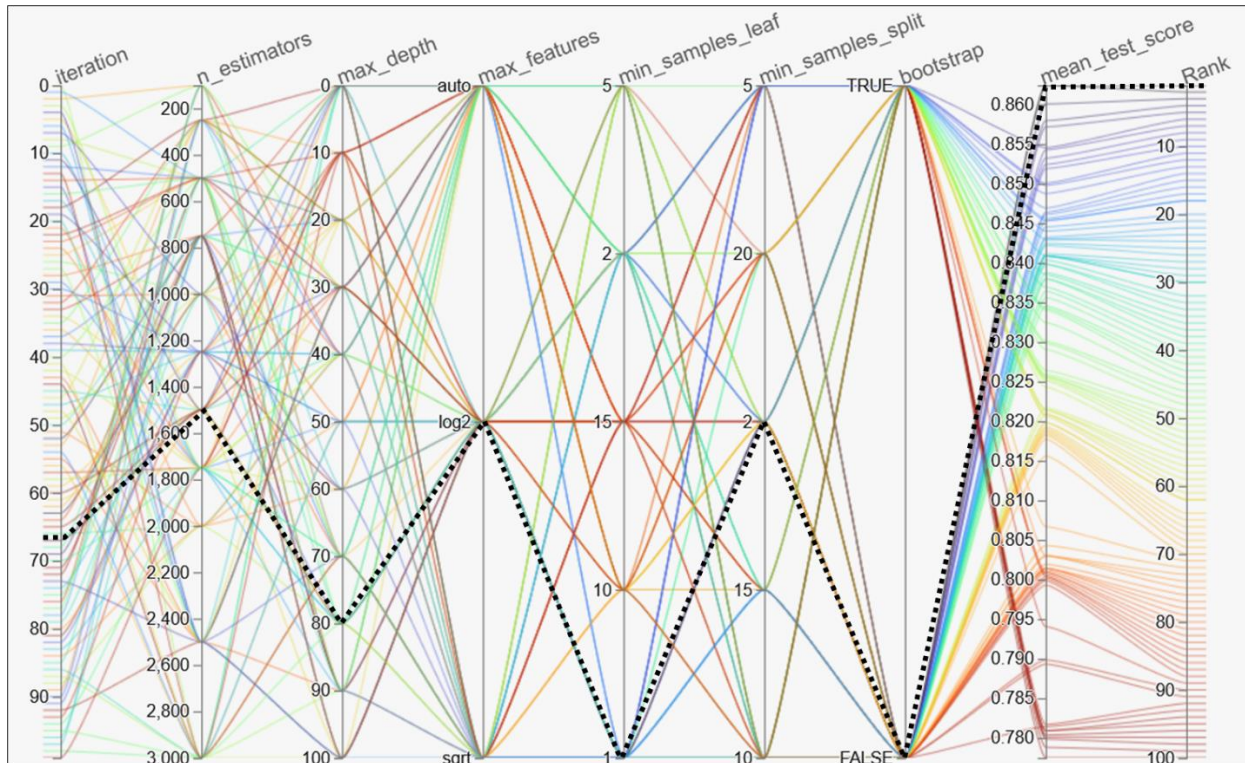
Figure 2-D. 1: Parallel coordinates visualization illustrating hyperparameter optimization for the random forest classifier. The plot displays the combination of each hyperparameter value and the corresponding test score, connected by lines (ranked and color-coded by the average F1 score). The dashed-black line shows hyperparameter values yielded the highest validation score and are used in the random forest model training. ***n_estimators*** parameter defines the total number of decision trees in the forest. The ***max_depth*** parameter is defined as the maximum depth of the tree. The ***max_features*** parameter is the number of maximum features provided to each tree in a random forest. The ***min_samples_leaf*** parameter is the minimum number of sample points that are allowed in a single leaf node. The ***min_samples_split*** can be defined as the minimum number of samples required to split an internal node. The ***bootstrap*** parameter refers to is a statistical resampling technique that involves random sampling of a dataset with replacement (Scikit-learn random forest web page, URL: https://scikit-learn.org, Accessed: May 2022).

Appendix E

Visual QC of the random forest prediction
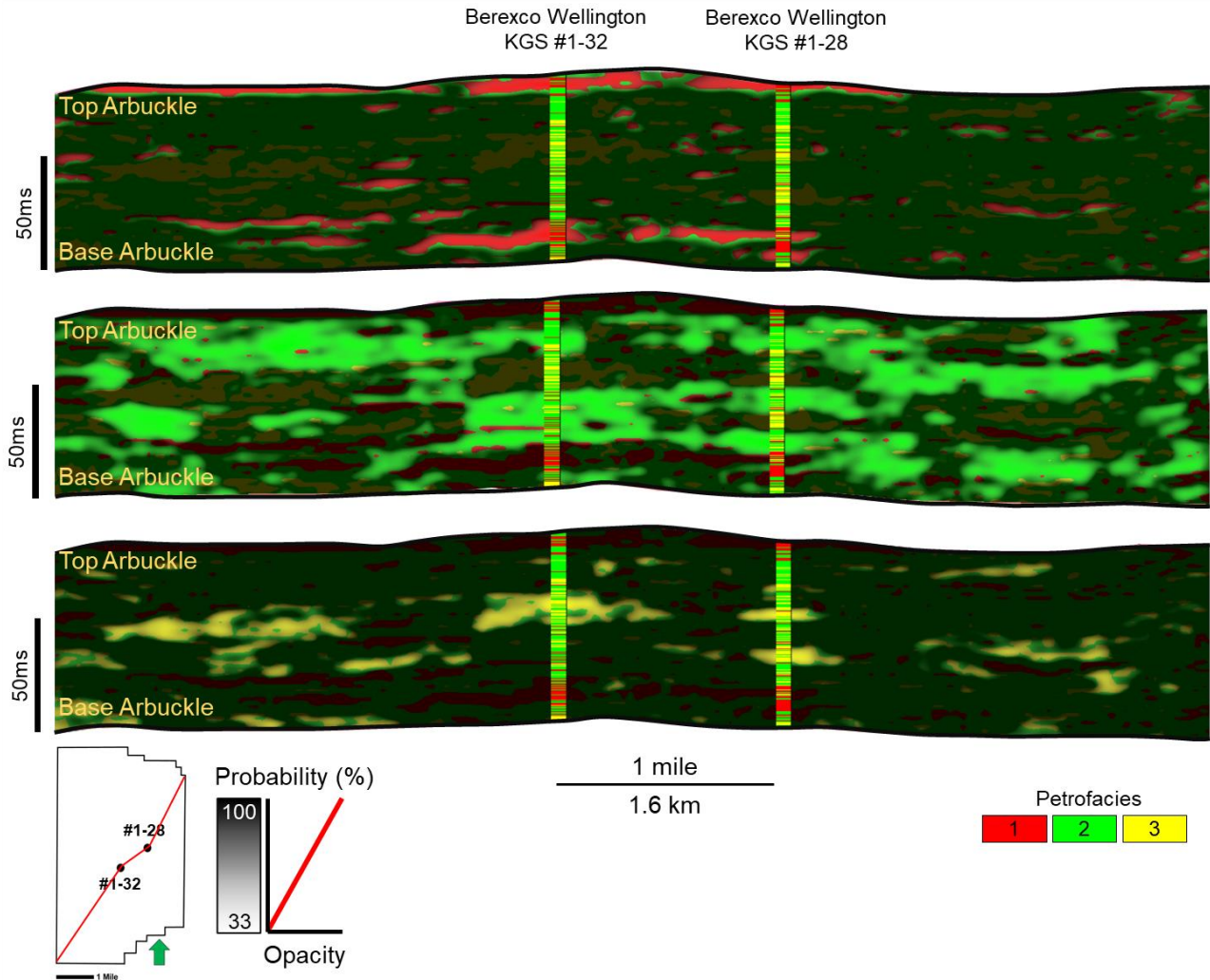
Figure 2-E. 1: Arbitrary lines from most probable petrofacies prediction volume are co-rendered with the individual petrofacies probability volumes showing the confidence in the random forest prediction. High probabilities of petrofacies prediction are set to be transparent, while the low probability values are set to be opaque black. Top figure shows the shows the QC of the prediction of the petrofacies 1, Middle figure shows the QC of the prediction of the Petrofacies 2 and the bottom figure shows the visual QC of the prediction of the petrofacies 3.

Chapter 2 Figures
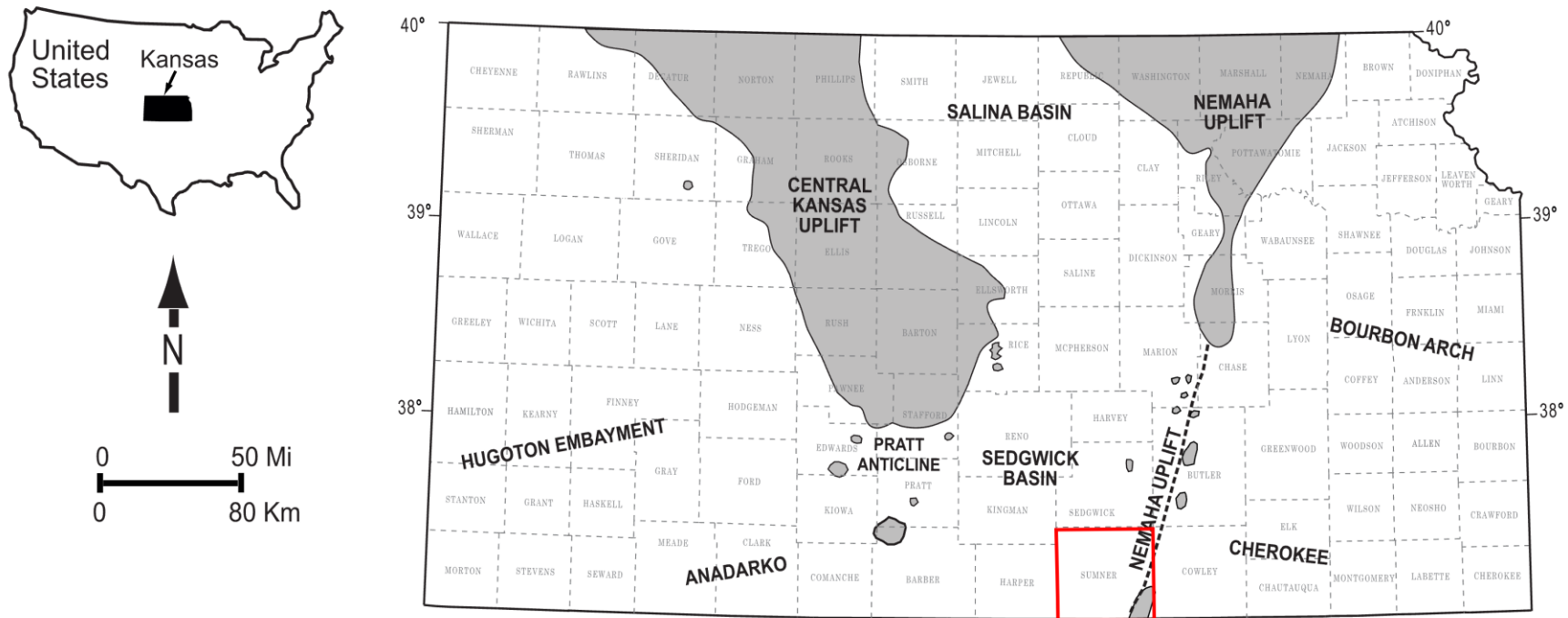
Figure 2.1: Regional map showing the subsurface tectonic features of Kansas. The Wellington field is located in Sumner County, Kansas (Red square, Modified after Dutton, 1984; Campbell et al., 1988; McConnell, 1989; Northcutt and Campbell, 1995; Johnson and Luza, 2008; LoCriccho, 2012).
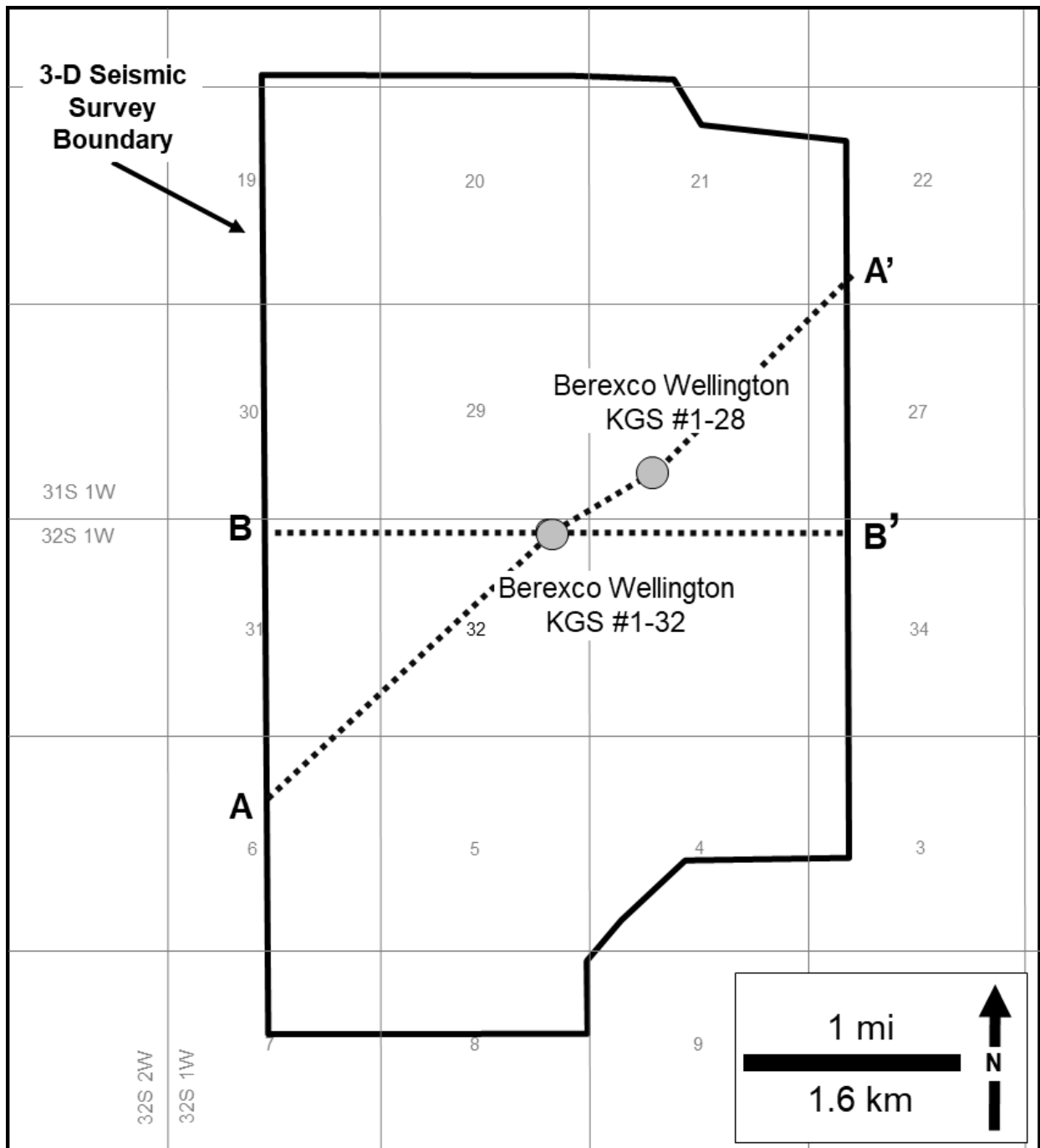
Figure 2.2: Detailed base map of the study area showing the 3D seismic survey and the wells used in the study. A-A' is the approximate location of the arbitrary line shown in figures 3, 12, and 13. B-B' is the arbitrary line shown in figure 11.
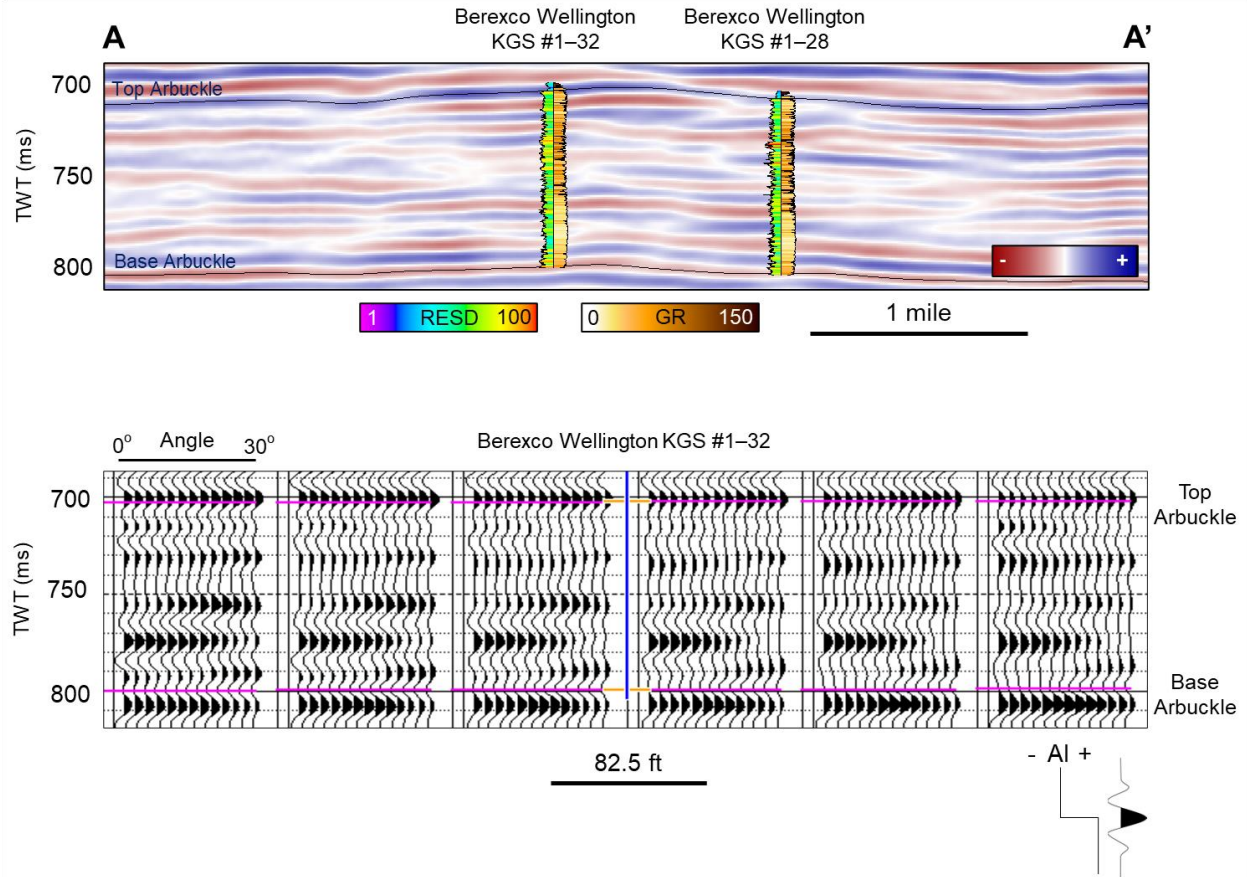
Figure 2.3: Arbitrary seismic line B-B' through the Berexco Wellington KGS #1-32 and Berexco Wellington KGS #1-28 showing the seismic survey used in the interpretation of the key horizons in the study interval (upper image). See Figure 2 for the location of the seismic line and wells. Pre-stack angle gathers were used in the study (lower image).
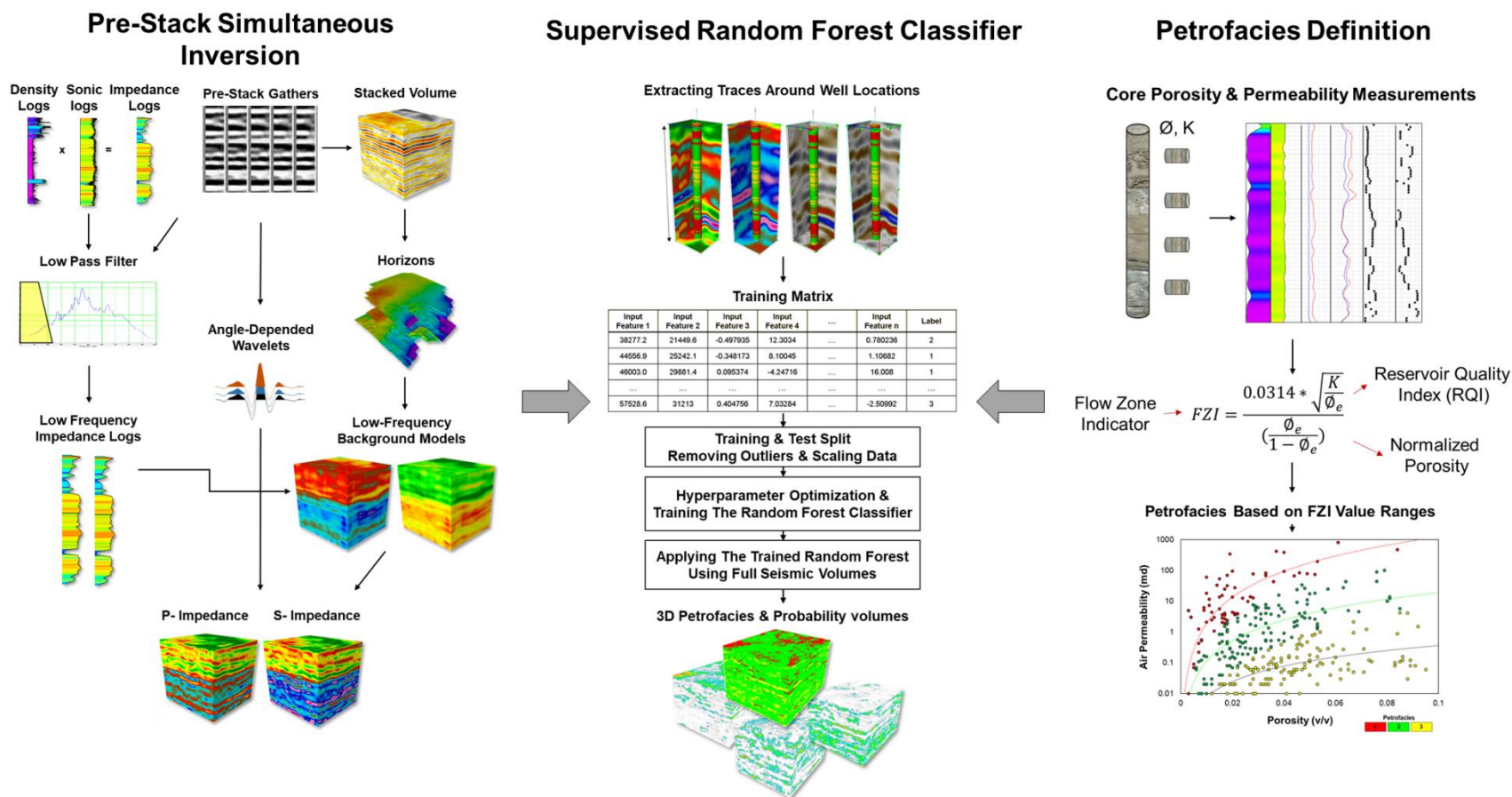
Figure 2.4: Generalized Workflow showing the three main steps followed in this study. These steps are simultaneous Pre-stack inversion for P and S Impedance volumes (Left), Supervised Random Forest Classifier (Middle), Petrophysics-based rock typing based on Flow Zone Indicator (Right).
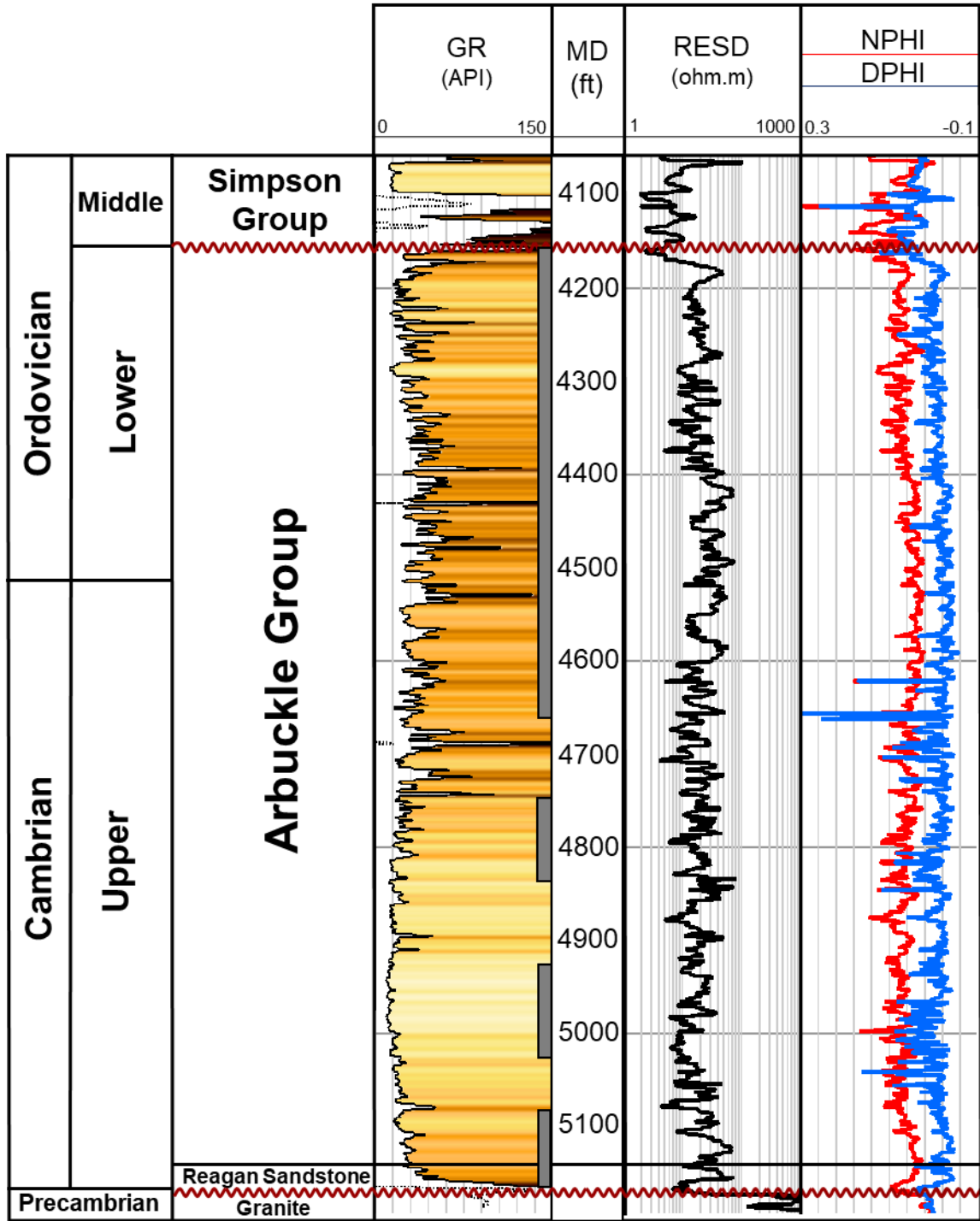
Figure 2.5: Generalized stratigraphic column of the study interval and Berexco Wellington KGS #1-32 type log. Gamma-ray (GR), deep resistivity (RESD), neutron porosity (NPHI), and density porosity (PHID) are shown. Gray bars represent cored intervals.
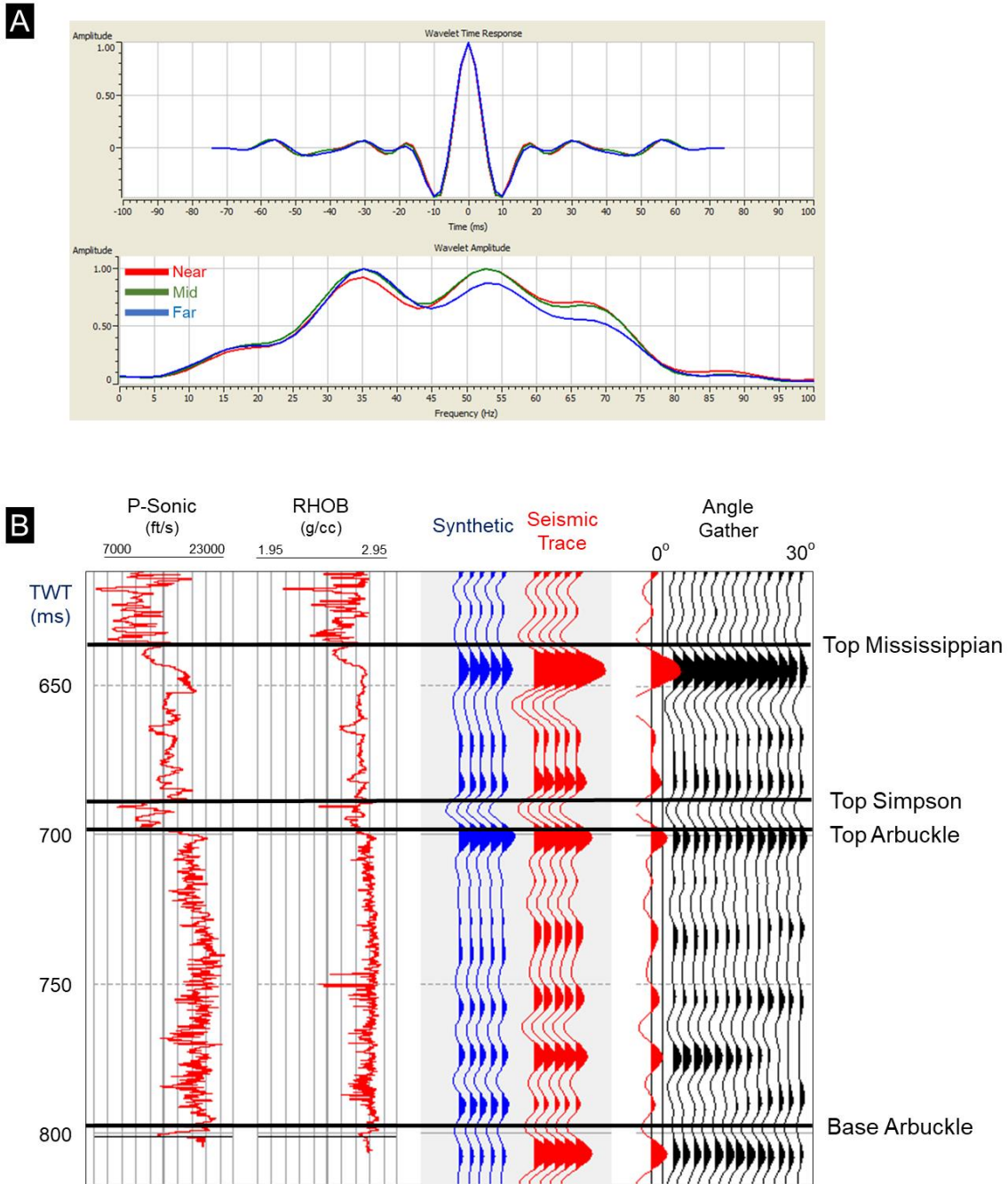
Figure 2.6: (A) The Extracted statistical wavelet group used in the simultaneous pre-stack inversion process. (B) Seismic-to-well correlation for the Berexco Wellington KGS #1-32. Using the near-angle wavelet, the synthetic seismogram was adjusted to match the near-angle trace at the well location. A cross-correlation of 80% was achieved.
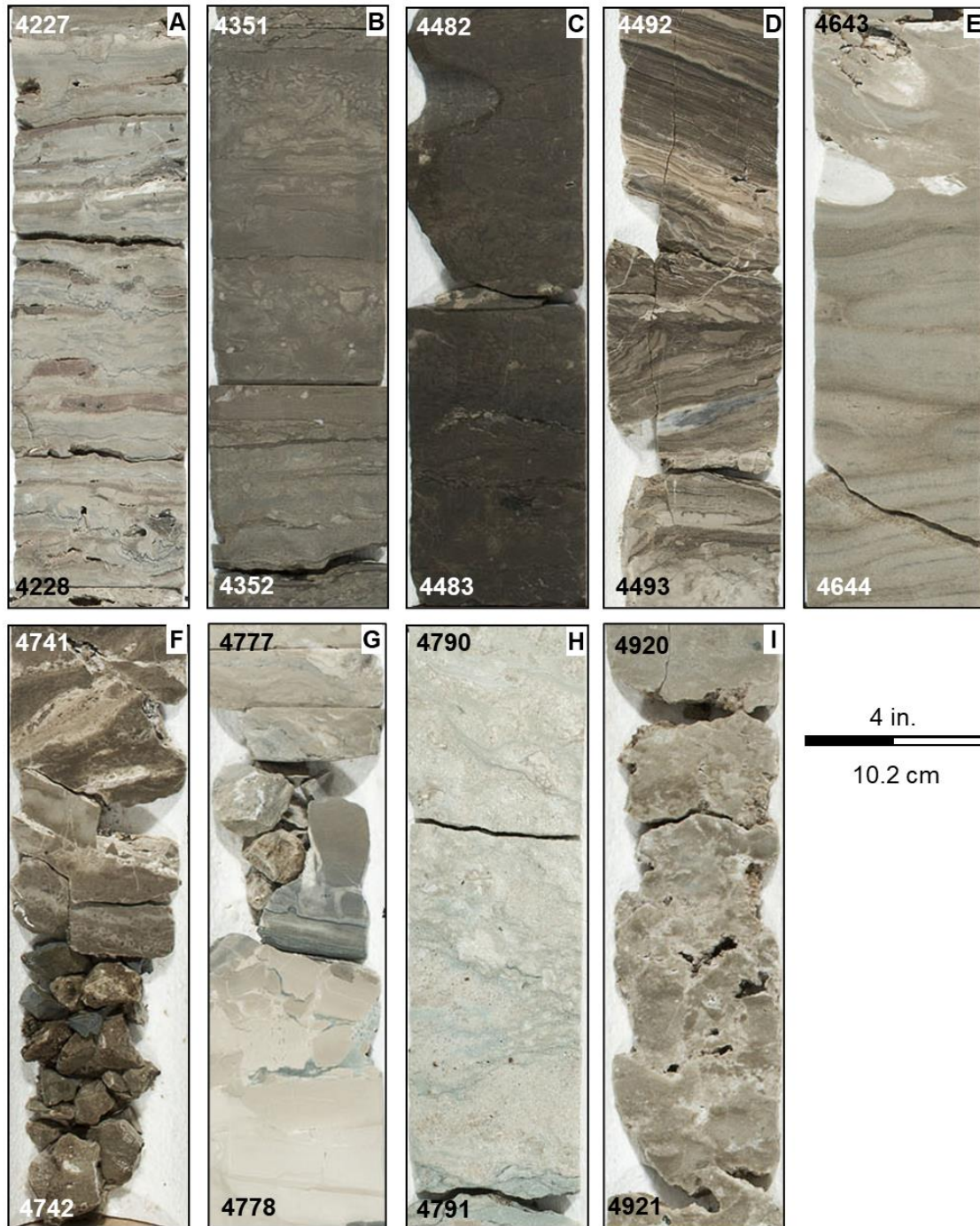
Figure 2.7: Core photographs of the identified Arbuckle lithologies in the study area: (A) Peloidal dolomitic packstone, (B) Argillaceous dolomitic packstone, (C) Argillaceous micritic dolomite, (D) Crystalline dolomite, (E) Crystalline micritic dolomite, (F) Dolomitic breccia, (G) Dolomitic mudstone, (H) Fine-grained dolomitic packstone, (I) Medium-grained dolomitic wackestone.
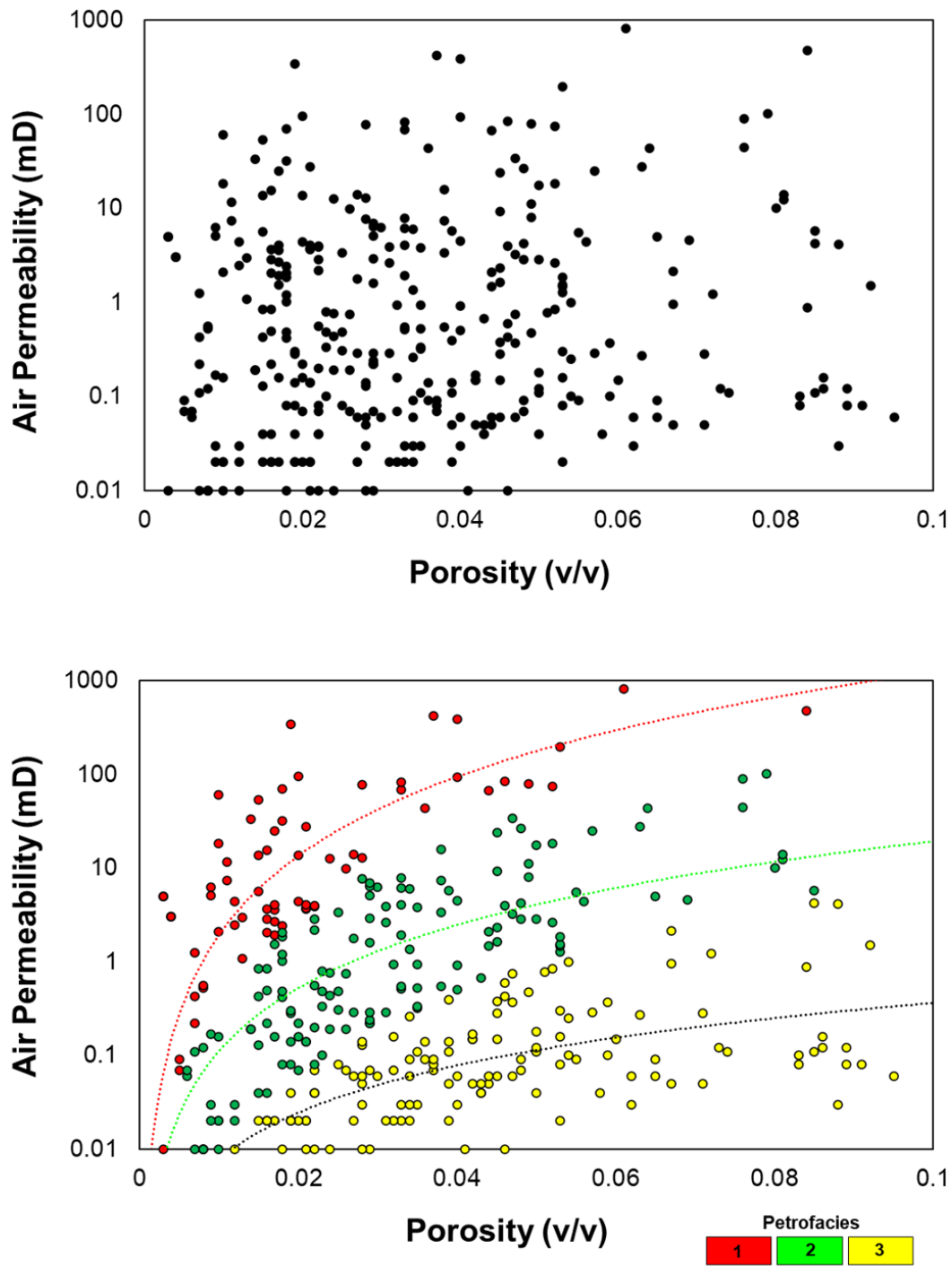
Figure 2.8: Petrofacies definition for the Arbuckle group. The upper image shows the cross-plot of core-measured permeability versus porosity. The lower figure shows the defined petrofacies using the FZI method.

96
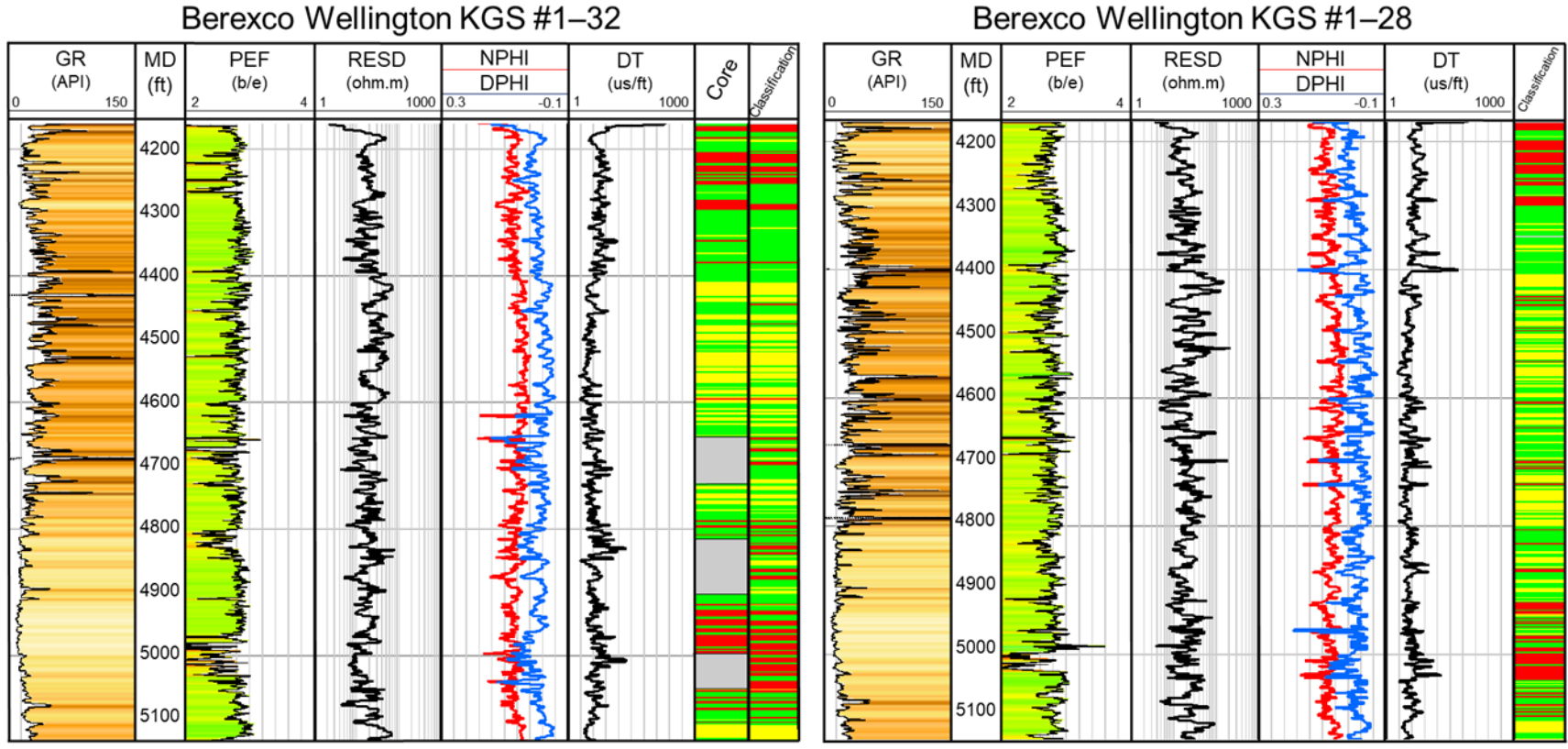
Figure 2.9: Core-defined petrofacies and the petrofacies classification from the ANN (right-most tracks) shown with a suite of well logs used in the ANN training (Gamma-ray (GR), photoelectric effect (PEF), deep resistivity (RESD), neutron porosity (NPHI) and density porosity (PHID), and P-wave sonic (DT)).
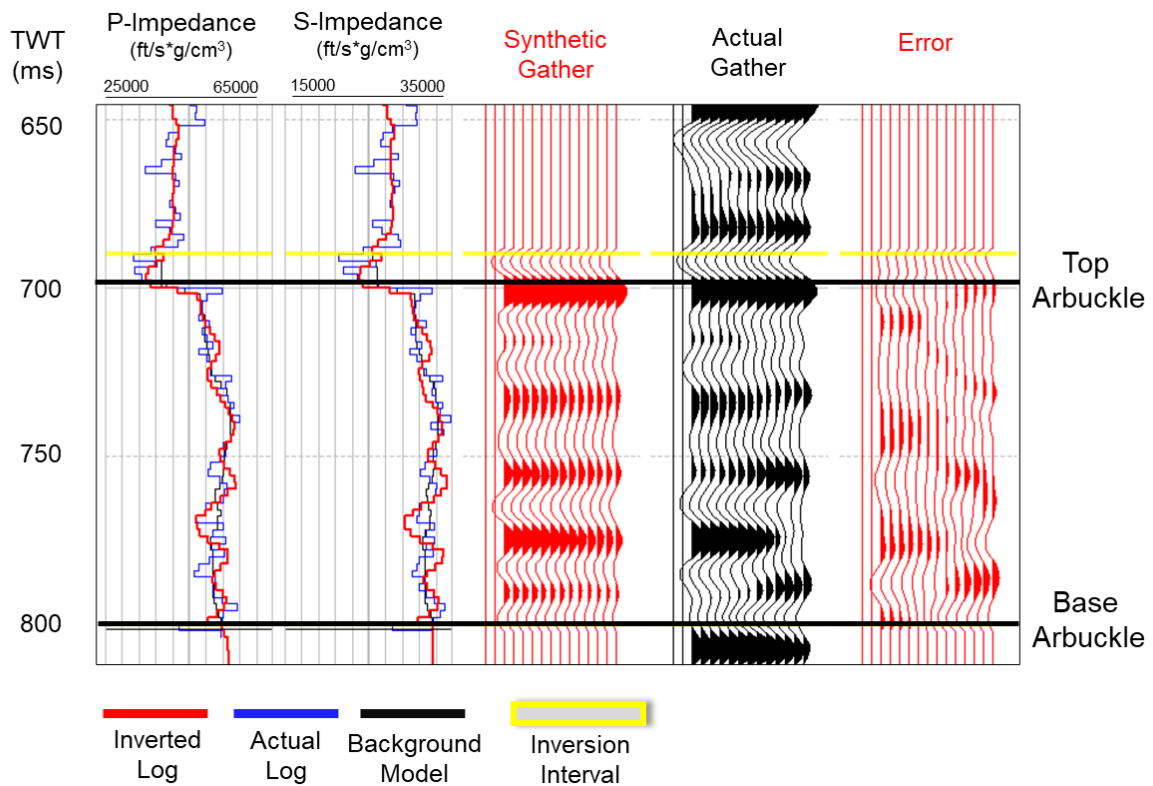
Figure 2.10: Quantitative Quality Control of the simultaneous pre-stack inversion results. The first two tracks show the overlay of low-frequency background models with actual and inverted impedance logs. Tracks 3-5 show the synthetic gather created by the inversion process, actual gathers used in the inversion, and the residual difference (error) in between, respectively. 89% correlation was achieved for the Berexco Wellington #1-32 well.
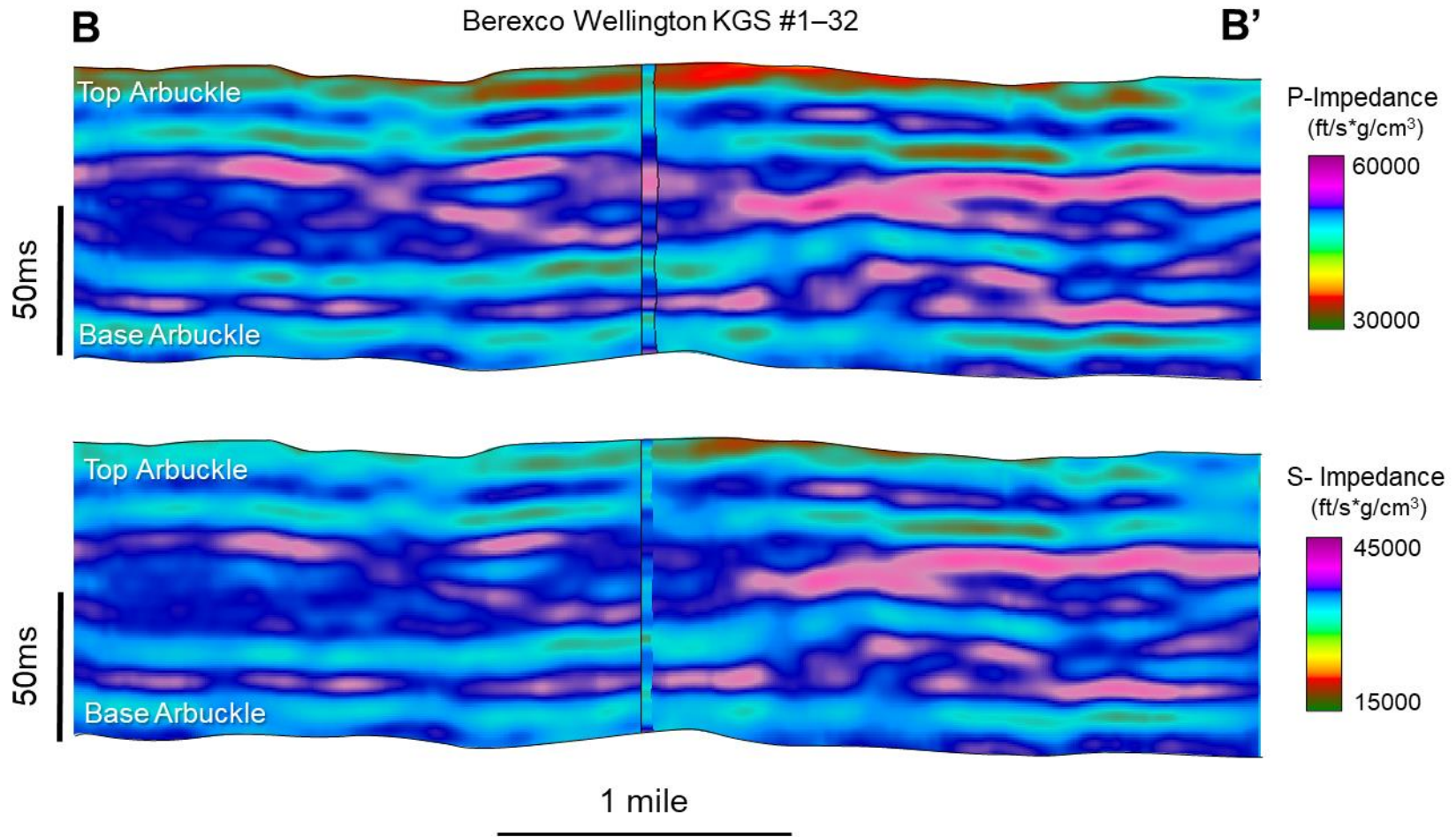
Figure 2.11: East-west arbitrary line (B-B') through Berexco Wellington KGS #1–32 showing the simultaneous pre-stack inversion results (Upper image: P-impedance, Lower image: S-impedance). High impedance values can be seen in the middle portion, while relatively lower values of impedances are primarily located in the Arbuckle Group's lower and upper parts of the Arbuckle Group.
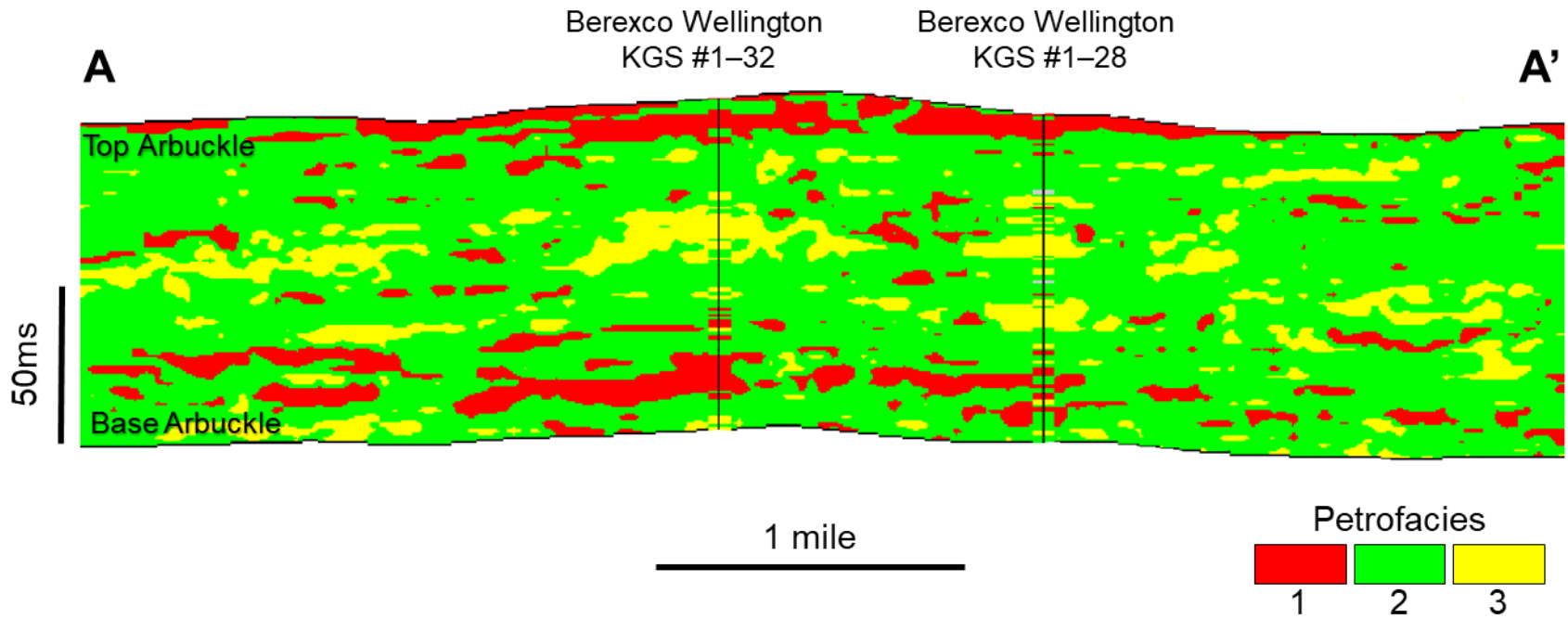
Figure 2.12: West-East arbitrary line (A-A') passing through the wells Berexco Wellington KGS #1–32 and #1-28 showing the random forest petrofacies prediction result. A good match between actual and predicted petrofacies at the well locations can be observed. Note that petrofacies 1 is mainly abundant in the lower Arbuckle, while petrofacies 2 and 3 are at the middle Arbuckle interval. The location of the arbitrary line is shown in Figure 2.
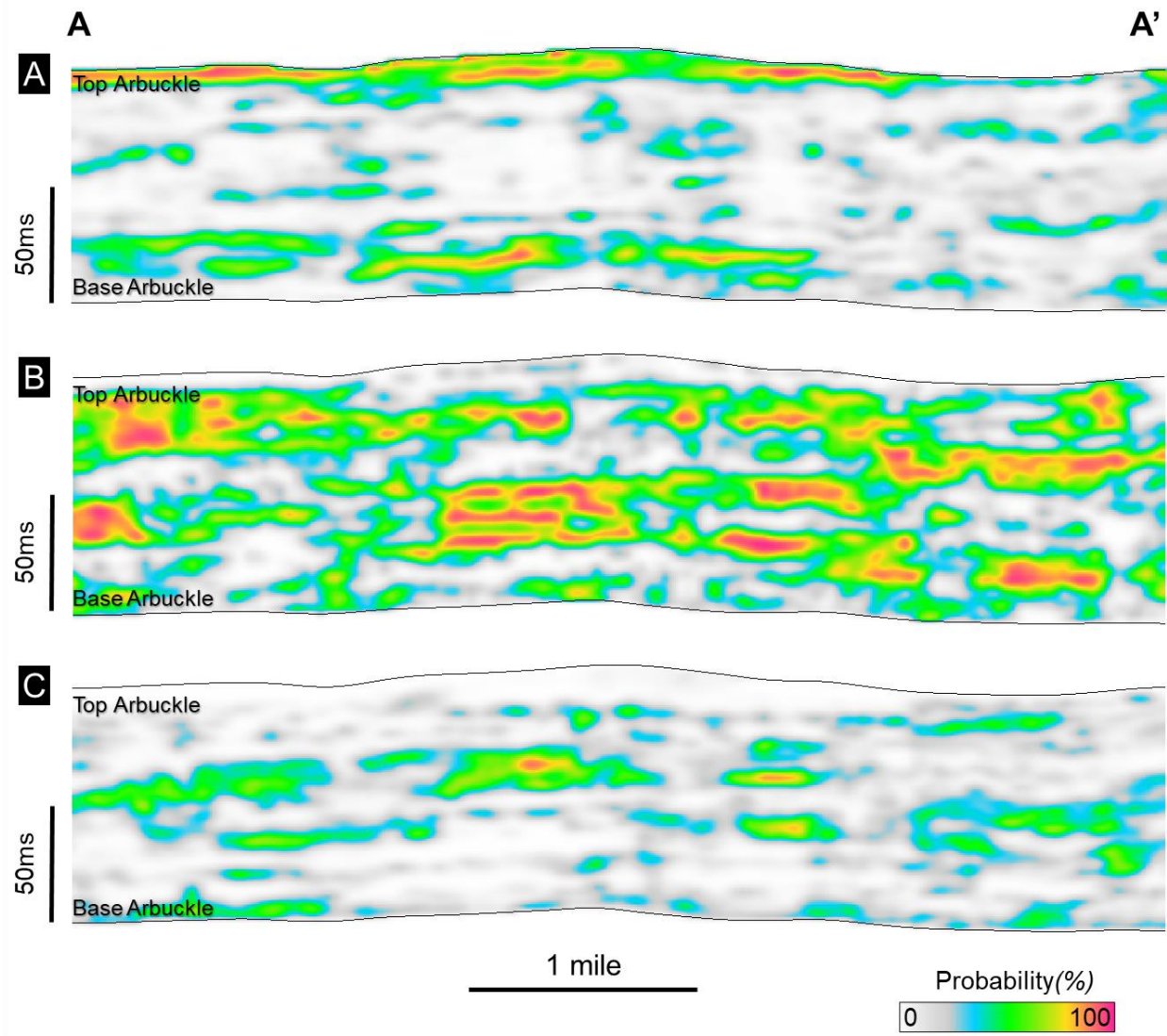
Figure 2.13: Southwest-northeast arbitrary line (A-A') showing the individual probability of prediction for each petrofacies: (A) probability of petrofacies 1, (A) probability of petrofacies 2, (A) probability of petrofacies 3. Location of the arbitrary line is shown in Figure 2.

Figure 2.14: Petrofacies volume values extracted on various stratal slices between the top and the base of the Arbuckle horizons. (A) Petrofacies volume values extracted from 20 ms above the base Arbuckle horizon. This interval mainly consists of petrofacies 1. (B) Petrofacies Horizon slice extraction 50ms above the base Arbuckle horizon. This interval is dominated by petrofacies 2 and 3. (C) Horizon slice extracted 15ms below the top Arbuckle horizon. Petrofacies 1 and 2 are prevalent in this interval. Heterogeneous distribution of petrofacies is observed throughout all the maps.

Chapter 2 Tables

	Classified Petrofacies		
		1	2	3
Actual Petrofacies 1	**84.2%**	15.5%	0.3%
2	5.6%	**87.1%**	7.3%
3	0.4%	12.9%	**86.7%**
Overall Accuracy	**87%**		

Table 2.1: Confusion matrix displaying the accuracy for the ANN petrofacies log classification in Berexco Wellington #1-32 using a log suite of the photoelectric effect (PEF), deep resistivity (RESD), total porosity (PHIT), and P-wave sonic (DT).

	Classified Petrofacies		
	1	2	3
1	**83.3%**	15.0%	1.7%
2	0.5%	**87.0%**	12.5%
3	5.2%	16.0%	**84.5%**
Overall Accuracy	**86%**		

Table 2.2: 3D seismic scale petrofacies prediction results. Confusion matrix showing the match between the actual petrofacies (logs) and the predicted petrofacies values from the supervised random forest classifier.

Chapter 3: Seismic-constrained reservoir modeling and simulation for CO₂ sequestration potential assessment of the Arbuckle Group: Wellington Field, Kansas*

*This chapter was presented in an invited talk at the 2nd International Meeting for Applied Geoscience and Energy (IMAGE) conference in 2022:

Abstract

The Arbuckle Group in the Wellington field in Kansas has recently been a focal point for CO_2 geosequestration feasibility studies, mainly through petrophysical, geophysical, and geostatistical modeling methods. The limited well control and the geological complexity of the study area add uncertainty to mapping the subsurface property variability. Therefore, the spatial variability of petrofacies and corresponding petrophysical properties of the Arbuckle Group are further addressed by integrating seismic-scale 3D petrofacies and petrophysical-property trends with well-log and core data to generate 3-D seismic-constrained petrofacies, porosity, and permeability models of the Arbuckle Group via geostatistical modeling. The seismic-constrained models reveal the lateral and stratigraphic heterogeneity of petrofacies, porosity, and permeability. Low permeability petrofacies of the middle Arbuckle interval act as baffles and barriers to fluid flow. Relatively higher porosity and permeability petrofacies in both the lower and upper Arbuckle are candidate injection zones. We calculated the theoretical CO_2 storage capacity using the DOE-NETL equation for saline aquifers. The theoretical CO_2 storage capacity for the study area is estimated between 0.95, 5.41, and 22.5 Mt for low-, mean-, and high-case scenarios. Using these static models, we performed dynamic CO_2 injection simulations to evaluate the subsurface behavior of a theoretical CO_2 plume for long-term carbon-storage potential. Dynamic simulation results show the CO_2 plume is dispersing laterally and contained within the injection zone during both injection and post-injection periods. The integrated workflow allows us to integrate supervised machine learning and seismic information to further constrain the geostatistical models. Compared to the previous studies, this workflow created 3D reservoir models that show

106

stratigraphic variability of subsurface properties in greater detail and further reduce the subsurface uncertainty in the study area.

Introduction

Carbon-storage technologies are crucial to reduce anthropogenic carbon dioxide (CO_2) emissions to help meet energy needs and alleviate climate impacts. Geologic carbon sequestration is one of the most effective carbon storage methods, given its efficiency, potential storage capacity, and cost. The process requires the injection and storage of CO_2 into a deep saline aquifer or a depleted hydrocarbon reservoir (Bachu, 2000; Gale, 2004; Friedmann, 2007; Breuning et al., 2013).

The Arbuckle Group saline aquifer has historically been used for various waste-water disposal operations. Recently, the Arbuckle Group in southern Kansas and Oklahoma has become a focus for CO_2 sequestration-related studies due to its proximity to significant sources of CO_2 emission and given its favorable geological properties (Watney and Rush, 2012; Holubnyak, 2017). To evaluate the CO_2 sequestration potential of the Arbuckle Group in the study area numerous studies with different levels of detail have been carried out (Carr et al., 2005; Holubnyak 2007 et al., 2007; Watney and Rush, 2012; Ohl and Raef, 2014; Gupta et al., 2017; Doveton and Watney, 2015).

Carr et al. (2005) used large-scale relational databases and geographic information system tools to integrate temperature, pressure, and water geochemistry data from numerous wells to create regional-scale hydrogeological models of the lower Paleozoic aquifer systems in Kansas and to evaluate their potential for geologic CO_2 sequestration. Holubnyak et al. (2007) developed

107

regional-scale subsurface models to assess the CO_2 storage capacity for the Arbuckle Group in southern Kansas and investigated potential candidate injection zones. Ohl and Raef (2014) performed seismic multi-attribute analysis to create 3D electrofacies clusters for seismic-scale characterization of the Arbuckle reservoir. Gupta et al. (2017) utilized S-wave amplitude variation with offset to evaluate fracture presence affecting the injectivity and CO_2 movement in the subsurface. Among these studies, the most notable work in the study area is by Watney and Rush (2012), whereby they utilized well logs, core measurements, and 3D seismic data to create porosity, permeability, rock-type models, and CO_2 plume simulations. They used the seismic reflection data to create a 3D pseudo-porosity attribute using an artificial neural network method. Then, they used the porosity attribute volume as a secondary 3D variable with co-Kriging to create a 3D porosity model via sequential Gaussian simulation (SGS). Watney and Rush (2012) used the 3D porosity model as a constraint (secondary variable) with SGS to create 3D models of horizontal, vertical, and maximum permeability. However, the 3D porosity and permeability models were created without any constraint to lithologies or facies information. Rather, Watney and Rush (2012) used the 3D porosity and permeability models to calculate a 3D reservoir quality index (RQI) model, and then arbitrarily defined rock types for the Arbuckle Group based on ranges of reservoir quality index (RQI cutoff values). Finally, Watney and Rush (2012) performed dynamic simulations to determine the potential pressure impact of 40,000 Mt of CO_2 injection and mapped the CO_2 plume extent. Their rock-type and petrophysical models illustrated that the lower portion of the Arbuckle Group is highly porous and permeable and therefore was the favorable interval for the injection. They also showed that, if injected, 40,000 tons of CO_2 could potentially reach a maximum lateral extent of 2150 ft (655 m) after 100 years of injection.

Watney and Rush (2012) and other previous studies mentioned here were conducted mainly with core and petrophysical property data, and they limited their integration of seismic data as a modeling constraint. Integrated studies that combine core lithologies (rock types), well logs, and 3-D seismic data and their attributes to 1) model rock types and associated petrophysical properties, 2) evaluate theoretical CO_2 storage capacity, and 3) assess the impact of seismic-constrained rock-type variability on CO_2 plume behavior have been limited.

To build upon this previous knowledge of the Arbuckle Group, we utilize seismic-constrained modeling that combines the Arbuckle Group stratigraphic and structural framework, core-and petrophysics-based rock-types (petrofacies), and seismic-based 3D petrofacies, and porosity trends. The aim is to model the 3D spatial variability of petrofacies, pore volume, theoretical CO_2 storage capacity, permeability, and CO_2 plume behavior using dynamic simulations. This study integrates data from different sources and scales to create 3D geological models to capture the detailed stratigraphic and spatial variability of petrofacies and corresponding petrophysical properties and assess the CO_2 storage potential in the study area.

The Wellington Field is in Sumner County, Kansas (Figure 3.1). Data for this study include a 3-D pre-stack time-migrated (PSTM) seismic survey covering a 12.6-mi^2 (~32.7-km^2) area. The seismic survey has a 2 ms sample rate and is processed with a bin size of 82.5 by 82.5 ft (25 by 25 m). The survey consists of 288 inlines and 178 crosslines and a record length of two seconds. The vertical seismic resolution (equal to one-fourth of a wavelength) at the interval of interest is 115 ft (~35 m). The dataset also includes two vertical wells, Berexco Wellington KGS #1–28 and #1-32 wells, with a full suite of open-hole logs, 800 ft (245 m) of core with petrophysical measurements and brine samples from the Berexco Wellington KGS #1–32 well (Figure 3.2).

109

The dataset also includes petrophysics-defined rock types (petrofacies) for the two wells (Figure 3), an acoustic impedance volume obtained from simultaneous pre-stack inversion, and seismic-scale 3D petrofacies and individual petrofacies probability volumes obtained via a supervised random forest algorithm. These data were obtained through the workflow shown in Chapter 2. The seismic and well data were used for seismic-to-well correlation and interpretation of key horizons to build the stratigraphic and structural framework (3D model grid). Acoustic impedance volume was used to create a 3D porosity probability volume to constrain the 3D porosity model. Petrofacies and individual petrofacies probability volumes were used as 3D probability trends to constraints for petrofacies model. The resulting 3D static models and the stratigraphic and structural framework were used as inputs for theoretical CO_2 storage capacity calculations and dynamic simulations to investigate CO_2 plume movement in injection and post-injection periods (Figure 3.3).

Geological Setting

The Wellington Field is located at the southern portion of the major pre-Desmoinesian to post-Mississippian-aged, shelf-like, southerly plunging feature called the Sedgwick Basin. The main structural components surrounding the study area are Central Kansas Uplift to the west, the Nemaha uplift to the east, the Salina Basin to the north, and the Anadarko Basin to the south (Merriam, 1963). In the study area, The Arbuckle Group overlays the Precambrian granitic basement and the Reagan Sandstone and is overlaid by the Simpson Group (Figure 3.4). The Arbuckle Group consists of (bottom to top) the Eminence Dolomite, Gasconade Dolomite with basal Gunther Sandstone, Robidoux formation, and Jefferson City/Cotter Dolomite. These rocks are described as platform carbonates mainly deposited in ramp-style subtidal to peritidal

environments within a hyper-saline shallow continental sea (Meriam 1963, Franseen 2004). During the Cambrian- to Ordovician, relative changes in the sea level manifested themselves with cyclical shallow subtidal to intertidal environments bounded by major unconformities resulting from major relative sea-level fall and consequent subaerial exposure (Franseen, 2004; Sloss, 1963). The Arbuckle Group underwent post-depositional dolomitization due to mixing fresh waters rich in magnesium with local marine waters. This resulted in complex rock fabrics and diverse reservoir and non-reservoir lithologies distribution due to dolomitization, hydrothermal alteration, karstification, and fracturing (Franseen et al., 2004). With a variety of pore types, including intercrystalline, moldic, fenestral, and vuggy, these lithologies are mostly boundstones, grainstones, packstones, and mudstones (Doveton and Watney, 2015).

The Arbuckle Group is regionally extensive over Kansas, except for a few structurally high areas on the Central Kansas uplift and the Nemaha anticline, where the Arbuckle has been eroded (Carr, 1986; Franseen et al., 2004). The average thickness of the Arbuckle Group reaches approximately 1000- 1200 ft (304-360 m) and gets thinner towards the north. Depth to the top of the Arbuckle is approximately at 4000 ft (~1220 m) at the study area, and it ranges approximately from 500ft (~150 m) in the southeast and deepens towards to west up to 6000ft (~1800 m) below the surface (Keroher and Kirby, 1948).

Methods

Lithologies and petrofacies

This study builds on the lithology and petrofacies analysis results, as discussed in detail in Chapter 2. Arbuckle Group lithologies are from Watney et al. (2012) and based on core

descriptions of the Berexco Wellington KGS #1–32 well. Using core-derived porosity and permeability measurements from the Berexco Wellington KGS #1–32 well, three petrofacies were defined, and petrofacies logs were created by the Flow Zone Indicator (FZI) approach (Amaefule et al., 1993). Then, using an Artificial Neural Network (ANN) method, petrofacies logs were classified for the uncored Berexco Wellington KGS #1-28 well.

Stratigraphic and structural framework – 3D seismic horizon interpretation

The 3D seismic and well data were used to interpret the stratigraphic and structural framework of the Arbuckle Group. This framework was used to construct a 3-D reservoir model grid for 3D petrofacies and petrophysical property modeling. For this process, Berexco Wellington KGS #1-32 and #1-28 wells were tied to the time-migrated seismic volume, and the seismic reflectors corresponding to the top and base of the Arbuckle Group were identified (Figure 3.5). Because the internal reflectors of the Arbuckle Group are not of high enough resolution to distinguish internal stratigraphy, we incorporated the acoustic impedance volume derived from the simultaneous pre-stack inversion process to further subdivide the Arbuckle into three stratigraphic intervals, from deepest to shallowest, Arbuckle zones A through C, and mapped them throughout the study area (Figure 3.6). In previous studies of the Arbuckle Group in this area (e.g., Watney and Rush, 2012; Gupta et al., 2017), these Arbuckle Group stratigraphic zones were not defined, mapped with seismic data, and explicitly incorporated as part of the 3D grid and static and dynamic models. Importantly, Arbuckle Group A and Arbuckle C have relatively low impedance values, while Arbuckle B is characterized by continuous-high impedance values throughout the study area.

Velocity model

We created a velocity model to convert seismic horizons, the 3D petrofacies volume, individual 3D petrofacies probabilities volumes, and the acoustic impedance volume into the depth domain. This task was achieved by using the interpreted seismic horizons (bottom to top: Precambrian basement and the top of the Arbuckle) and their corresponding well tops. The model uses the instantaneous velocities from the wells with time-depth relationships (TDR) from the seismic-to-well tie process and the seismic time horizons allowing the model layer velocities to vary with depth and by stratigraphic zone, using a linear equation:

$$V(Z) = V_0 + k * Z \tag{1}$$

Where $V(Z)$ represents instantaneous velocity at depth Z, V_0 is the initial velocity, k is the time-to-depth relationship established from wells, and Z represents the depth.

Seismic-constrained 3D reservoir modeling

A 3D reservoir model grid was generated by incorporating the stratigraphic surfaces (structure-contour maps) created from the interpreted seismic horizons and well tops. The aerial cell dimensions of the 3D grid were set considering the horizontal resolution of the seismic data, while the vertical cell dimensions were set by analyzing the petrofacies, porosity and permeability logs, ensuring the resulting model captures the stratigraphic variability (Figure 3.7).

Vertical variograms were derived using the petrofacies logs. The petrofacies prediction volume and corresponding petrofacies probability volumes were resampled to the 3D model grid and converted into corresponding discrete and continuous property models, respectively (Figure

3.8). These models were then used to evaluate horizontal variogram ranges and estimate the major and minor range azimuths for each property by zone (Appendix-A).

The 3D petrofacies model was generated using sequential-indicator simulation (SIS). The model was constrained by 1) the stratigraphic and structural framework (3D grid), 2) upscaled petrofacies logs, 3) petrofacies variogram parameters by zone, 4) petrofacies fractions by zone, and 5) individual petrofacies probability volumes (Figure 3.9). The petrofacies logs were upscaled to the 3D model grid by assigning a single value for each cell based on the most abundant petrofacies within the cell. The petrofacies fractions by zone were obtained from the upscaled logs.

3D porosity and permeability models were generated to analyze the spatial distribution of total porosity and permeability. The porosity model was generated using sequential-Gaussian simulation (SGS), and it is constrained by the following: 1) 3D petrofacies model, 2) upscaled porosity logs biased to the petrofacies logs using arithmetic mean, 3) porosity histograms by zone and petrofacies, 4) variogram parameters by each zone and petrofacies, and 5) porosity trend volume computed using the relationship between p-impedance and porosity (Appendix-B)

A 3D horizontal permeability model was also generated using the SGS algorithm with collocated co-kriging using the porosity model as the secondary variable. Like the porosity model, the permeability model was also constrained by the petrofacies model, upscaled permeability logs, permeability histograms, variogram parameters by each zone and petrofacies, and the correlation coefficient between porosity and permeability. (Figure 3.10).

Theoretical CO₂ storage capacity estimation

To evaluate the CO_2 storage capacity of the Arbuckle Group in the study area, we calculated the theoretical storage capacity for low, median, and high cases using the methodology developed by US-DOE. For saline formations, the theoretical CO_2 storage capacity is calculated using the formula below (Goodman et al., 2011):

$$G_{CO_2} = A_t * h_g * \emptyset_{total} * \rho * E_{saline} \tag{1}$$

Where A_t represents the total area, h_g Is the gross formation thickness, $\emptyset_{total}$ is the total porosity (v/v), ρ is the density of the CO_2. E_{saline} is the efficiency factor corresponding to the fraction of the total pore volume that will be taken by the injected CO_2 (Goodman et al., 2011). For the area calculation, we used the total area of the reservoir model grid, and for the gross thickness, we used the minimum, median, and 90th percentile thickness values taken from the modeling grid isopach maps for the Arbuckle zone A and the entire Arbuckle group. We have used the 10th, 50th, and 90th percentiles of total porosity values taken from the porosity model. For the CO_2 density value, we used the average value calculated by Watney and Rush (2012) and Holubnyak (2017) based on the average depth, temperature, and pressure values of the Arbuckle Group in the study area. For the efficiency factor values (E_{saline}) we used the P10, P50, and P90 values developed for dolomites established by Goodman et al. (2011). The summary of the input values can be seen in Tables 3.1 and 3.2.

Dynamic flow simulation

We performed dynamic simulation using commercial reservoir simulation software to investigate CO_2 plume dynamics in injection and post-injection periods within the study area. For

this process, we input the 3D petrofacies, porosity, and permeability models, 3D models of ion concentrations in the brine, and additional parameters such as relative permeability and capillary pressure curves (Appendix- C). Isotropic horizontal permeability (i- and j-orientations) was used, and vertical permeability (k-orientation) was scaled to 10% of the horizontal permeability. Separate models of dissolved ions were created by creating a linear vertical function from ion concentration samples versus depth values and assigning them to the entire model grid.

Due to limitations in computational power and associated run time, the fine-scale geologic models were upscaled prior to flow simulation. The critical element in this process is the assurance of maintaining the essential small-scale stratigraphic variability that potentially affects fluid flow while coarsening the model grid adequately to achieve computationally efficient flow simulation. Therefore, we upscaled the static models using the volume-weighted averaging approach to upscale the model to a larger grid size of 110 ft by 110 ft (33.52 m) aerially and to 10 ft (3.04 m) vertical resolution (Appendix D). The base-case simulation scenario considered a 100-year injection period and a post-injection period of 100 years. For this scenario, CO_2 is injected through the Berexco Wellington KGS #1-28 well with a 140 ft (42.6 m) perforation interval within the Arbuckle A interval. The base-case scenario includes a target injection rate of 100 Mt/year and a bottom-hole injection pressure of 2538 psi (175 bar) corresponding to 90% of the estimated fracture gradient to avoid injection-induced fracturing (Watney and Rush, 2012).

Results

Structural and stratigraphic framework

In terms of the seismic signature, the top of the Arbuckle exhibits a strong peak, while the base of the Arbuckle (Precambrian Basement) corresponds to a very continuous and high amplitude, well-defined trough. The Arbuckle interval in the study area dips toward the southeast, and thickness ranges from approximately 800 to 1020 ft (243.84 to 310.89 m). The Arbuckle is thicker in the central and southern parts of the area and thins toward the northwest (Figure 3.11). Schwab et al (2017) indicated that there are faults interpreted within the study area. However, based on the seismic attribute analysis we did not observe any seismically resolvable faults were within the Arbuckle; therefore, no faults were incorporated into the structural and stratigraphic grid.

3D grid

The 3-D reservoir model grid integrates the stratigraphic surfaces created from interpreted seismic horizons and corresponding well tops. The grid contains three zones (from base to top, Arbuckle A, B, and C) and represents the structural and stratigraphic framework of the Arbuckle Group. The 3D grid covers an area of approximately 10.4 mi^2 (26.9 km^2). The grid size was defined based on 1) the bin size of the seismic volume for the horizontal cell size to preserve the horizontal seismic resolution and 2) the vertical thickness of layers to represent the vertical variations observed in the petrofacies, porosity, and permeability logs. The grid comprises 179 x 289 x 450 cells in the I, J, and K directions, resulting in 23,278,950 cells with a proportional layering scheme (Figure 3.12).

Spatial distribution of petrofacies and reservoir properties

The petrofacies vertical variogram ranges vary from 5.6-13.7 ft (1.7-4.1 m). Horizontal variogram minor and major ranges vary from 2014-5600 ft (614-1707 m) for petrofacies 1, 2194 to 5900 ft (668. to 1798 m) for petrofacies 2, and 2950 to 7100 ft (899 to 2164 m) for petrofacies 3 respectively. Major axis orientations range from 34 to 337 degrees from the north (Appendix A). Zones A and C are mainly composed of petrofacies 1 and 2, while Zone B is dominated by petrofacies 2 and 3 (Figures 13 and 14). Regarding individual petrofacies percentages, the Arbuckle zone A contains 26.9% of petrofacies 1, 54.2% of petrofacies 2, and 18.9% of petrofacies 3. The Arbuckle zone B is mainly composed of petrofacies 2 and 3 (57.7% and 37.8%, respectively), with a small fraction of petrofacies 1 (4.5%). Like zone A, petrofacies 1 and 2 also comprise the highest petrofacies fractions (27.6% and 59.9%, respectively) of zone C. In terms of spatial variability, petrofacies 1, which are made up of vuggy and coarse-grained dolomites are distributed somewhat uniformly throughout zones A and C. Fine-grained and argillaceous packstones and mudstones of petrofacies 2 is mainly concentrated in the northwestern portion of zone A and the central and southeastern portions of zones B and C. Lowest permeability argillaceous dolomudstones and crystalline dolomites of petrofacies 3 is mainly concentrated in the central and northeastern portions of zone B, while showing a similar trend with petrofacies 2 by having a southwest-northeast linear trend (Figure 15).

The total porosity model displays values that range from 2 to 12% (Figures 3.13 and 3.14). The porosity model vertical variogram ranges from 4.4-11.1 ft (1.3-3.4 m). Horizontal minor and major ranges vary from 2960-6900 ft (902-2103 m). Major axis orientations are approximately from 4.8 to 348 degrees from the north. (Appendix A). The porosity model shows an upward

decrease in total porosity moving up section zone A to zone B, then increasing again at zone C (Figure 13). Zones A and C exhibit high average porosity values (up to 8%). High porosity values are often associated with porous and permeable petrofacies 1. In contrast, zone B has low average porosity values of up to 4%, as fine-grained argillaceous petrofacies 2 and micritic and crystalline low permeability rocks of petrofacies 3 mainly dominate this zone (Figure 3.16).

The Arbuckle permeability model ranges from 0.001 to 1000 mD (Figures 3.13 and 3.14). Similar to the average porosity trends, high average permeability values are observed for zone A and C (250 to 300 mD, respectively). In comparison, zone B has comparatively low average permeability of approximately 37 mD (Figure 3.17).

CO_2 storage capacity

Using the DOE methodology (Goodman et al., 2011), we estimated the theoretical storage capacity of the Arbuckle zone A and the entire Arbuckle stratigraphic interval for the area covering the modeling boundary Based on the low, median, and high range cut-offs for gross thickness, porosity, and efficiency factor values, the theoretical CO_2 storage capacity of the Arbuckle Group in the study area is estimated between 0.95, 5.41 and 22.5 Mt for low, median, and high cases, respectively. For the Arbuckle Zone A, the theoretical CO_2 storage capacity is estimated between 0.4, 2.2 and 8.9 Mt for the low, median and the high cases. These results provide estimates of the available space for CO_2 injection in the study area and only consider the scenario that the injected CO_2 will be trapped physically without dissolution and precipitation, and the in-situ formation fluid will be displaced away from the injected aquifer.

Using the dynamic simulation, we analyzed the CO_2 plume movement based on the injection parameters defined in the base-case scenario. To delineate the spatial extent, we used a similar approach as Zapata et al. (2020), where we considered all grid cells with a CO_2 aqueous mole-fraction larger than a threshold of 1×10^{-5} as the part of the plume within the model framework. The injected CO_2 can be seen entirely contained within the porous and permeable Arbuckle zone A due to the tight, impermeable characteristics of the Arbuckle zone B, acting as a baffle. Due to the presence of stratigraphic baffles, the average lateral propagation of the plume is larger than the vertical dispersion during both injection and post-injection periods (Figures 3.18, 3.19, 3.20). At the end of 100 years of injection and 100 years of the post-injection periods, the maximum lateral extent of the plume is 4450 ft (1356 m), and the greatest vertical axis of the plume body reaches up to 340 ft (103 m) (Figure 3.21).

Discussion

The integration of core-derived lithologies and petrofacies with 3D seismic data were useful to identify the spatial variability of petrofacies and corresponding petrophysical properties of the Arbuckle Group.

Compared to the previous work of Watney and Rush (2012), this study has several differences in the workflow, modeling parameters, and data integration. Watney and Rush (2012) did not identify stratigraphic zones within the Arbuckle Group but created their 3D model grid using a single top of Arbuckle structure-contour map and defined the base of the 3D grid using the "follow-the-top" approach. Their model consists of 706 x 654 x 79 cells in the I, J, and K directions

(total = 36,476,196 cells) and covers an area of 1.56 mi^2 (4.04 km$_2$). We defined our 3D grid using

the interpreted seismic horizons for 3 zones that were interpreted for the Arbuckle Group based on

the distinct differences in acoustic impedance. The 3D grid defined in this study spans a larger

area of approximately 10.4 mi^2 (26.9 km^2) and comprises 179 x 289 x 450 cells in the I, J, and K

directions, resulting in 23,278,950 cells (Figure 22)

Watney and Rush (2012) created their rock-type model by first creating porosity and

permeability models, calculating reservoir quality index (RQI), and then defining rock types by

arbitrarily binning RQI values. Therefore, their porosity and permeability models are not

constrained to lithologies. In this study, we first created the 3D petrofacies (rock-type) model using

the upscaled petrofacies logs (linked to core-based rock types) and the seismic-based 3D

petrofacies trend volumes. Because porosity and permeability are often related to rock types (e.g.,

lithologies and facies), the 3D petrofacies model was subsequently used to constrain the spatial

distribution of porosity and permeability. Petrofacies logs were created based on the core-derived

porosity and permeability measurements using the FZI method, where each petrofacies is directly

related to the lithofacies defined in core. 3D petrofacies trend volumes provided spatial variability

information to guide the distribution of petrofacies away and between the wells, reducing the

uncertainty caused by the inherent subsurface heterogeneity and the limited control in the study

area (Figures 3.23 and 3.24).

Watney and Rush (2012) created their porosity model without any constraint to a facies

model and used a single isotropic variogram of 5000 ft (1524 m) for the horizontal range. They

used the ANN-based porosity volume as a secondary variable with co-kriging, with an arbitrary

correlation coefficient of 0.75. In comparison, our porosity model is biased to the petrofacies

model, and each petrofacies has defined variogram parameters for each zone. To provide the spatial trend information, we created a porosity trend volume based on the relationship between the acoustic impedance and the total porosity. Horizontal variogram parameters were defined based on the trend volume. To create horizontal and vertical permeability models, Watney and Rush (2012) used the porosity model as the secondary variable with collocated co-kriging with a 0.70 correlation coefficient. Like the porosity model, Watney and Rush (2012) also used a single isotropic variogram for the entire model. In this study, we created a horizontal permeability model using a similar approach, using the porosity model as a secondary variable with collocated co-kriging. However, we used different variogram parameters per petrofacies and per zone (using the same values as the porosity variogram) and estimated correlation coefficients separately for each petrofacies and each zone (Figures 3.25 and 3.26).

For the CO_2 plume simulations, our scenario involved 100 t/day injection rate for 100 years (total of 3.6 Mt) and 100 years post-injection periods. The amount of simulated CO_2 injection is well within the range of our theoretical storage capacity estimates and nearby analog fields with similar average porosity, area, and thickness calculated by Holubnyak et al. (2017). In comparison, Watney and Rush (2012) simulated nine months of CO_2 injection with the rate of 150 Mt/day (a total of 40,000 Mt) and 100-year post-injection periods based on the permit that the operating company is seeking for the intended small-scale field test. In terms of the plume migration, the simulated plume from Watney and Rush (2012) axis reaches up to 2150 feet (655 m) laterally and vertically stays within the perforated zone (140 ft-42.6 m). In this study, the horizontal axis of the plume horizontal reaches 4450 ft (1356 m), and the vertical axis reaches up to 340 ft (103 m).

These differences are due to the differences in the injection amount and in the static models of porosity, permeability and the rock type.

Conclusions

In this study, we successfully applied seismic-constrained reservoir modeling and simulation workflows to characterize the subsurface heterogeneity of the Arbuckle Group by investigating the fine-scale stratigraphic and spatial variability of petrophysically defined facies and corresponding petrophysical properties.

The resulting 3D models showed that the Arbuckle group is made up of three stratigraphic intervals (Zones A, B, and C) with distinct petrophysical and fluid flow characteristics. The lowermost and the uppermost zones have high average porosity and permeability values, showing a high potential for CO_2 injection and storage. The middle Arbuckle zone shows the lowest average porosity and permeability values, displaying the characteristic of a fluid-flow barrier. The distribution of the petrophysical properties is directly correlated to the petrofacies, where petrofacies 1, having the highest permeability for a given porosity, is mainly at Arbuckle's lower and upper zones. In contrast, petrofacies 3, with the lowest porosity and permeability, is concentrated at the middle Arbuckle interval. Based on the DOE's methodology, theoretical CO_2 storage capacity ranges from 1 to 22Mt at the Arbuckle group in the study area.

Dynamic simulation results illustrate the subsurface plume evaluation as a function of hydrogeological, petrophysical, and operational parameters. Simulation results also revealed that a theoretical injection of 3.6 million tons of CO_2 would be contained within the injected zone A due to the low permeability characteristics of zone B. Additionally, the lateral propagation of the

plume is larger than the vertical dispersion during both injection and post-injection periods due to the internal stratification and baffles. Moreover, the lateral propagation of the plume is larger than the vertical dispersion during both injection and post-injection periods due to the internal stratification and baffles.

The integration of seismic data in this study added value to the accuracy of the reservoir models by helping to define the structural and stratigraphic framework of the area through the incorporation of interpreted horizons. Additionally, seismic-scale 3D petrofacies and probability volumes aided the modeling process by adding a lateral constraint to the spatial distribution of petrofacies between and away from the wells. The seismic data also add a lateral constraint to the distribution of petrophysical properties by using the acoustic impedance volume to guide the porosity distribution within the model framework. Overall, incorporating the seismic data into the reservoir modeling helps fully constrain the model spatial constraints improving the analysis of the Arbuckle structure, stratigraphy, and distribution of petrophysical properties, and fluid flow behavior within the study area. The workflow applied in this study provided geologically sound results by bridging the gap between wells and reducing the uncertainty where the well control is limited.

Acknowledgments

References

Amaefule, J., M. Altunbay, D. Tiab, D. Kersey, and D. Keelan, 1993, Enhanced reservoir description: Using core and log data to identify hydraulic (flow) units and predict permeability in un-cored intervals/wells: Proceedings of SPE Annual Technical Conference and Exhibition, doi:10.2523/26436-ms.

D.L. Baars, W. Lynn Watney, Don W. Steeples, and Erling A. Brostuen 2001, Petroleum: a primer for Kansas, Kansas Geological Survey, http://www.kgs.ku.edu/Publications/Oil/ primer09.html

Bachu, S., 2000, Sequestration of CO2 in geological media: criteria and approach for site selection in response to climate change. Energy Convers. Manag., 41 (9), 953–970, doi: 10.1016/S0196-8904(99)00149-1.

Campbell, J. A., C. J. Mankin, A. B. Schwarzkopf, and J. J. Raymer, 1988, Habitat of petroleum in Permian rocks of the Midcontinent region; in, Permian Rocks of the Midcontinent, W. A. Morgan and J. A. Babcock, eds.: Midcontinent Society of Economic Paleontologists and Mineralogists, Special Publication No. 1, 13–35.

Carr, J., E., H. E. McGovern, T. Gogel, and J. H. Doveton, 1986, Geohydrology of and potential for fluid disposal in the Arbuckle Aquifer in Kansas. U.S. Geological Survey open-file report, 86-491, doi: 10.3133/ofr86491

Carr, T. R., D. F. Merriam, and J. D. Bartley, 2005, Use of relational databases to evaluate regional petroleum accumulation, groundwater flow, and CO2 sequestration in Kansas, AAPG Bulletin, 89 no. 12, 1607–1627, doi:10.1306/07190504086

Doveton, J., and L. Watney, 2015, Textural and pore size analysis of carbonates from integrated core and nuclear magnetic resonance logging: An Arbuckle study, Interpretation 3, SA77-SA89, doi: 10.1190/INT-2014-0050.1.

Dutton, S. P., 1984, Fan-Delta Granite Wash of the Texas Panhandle: Oklahoma City Geological Society, Short Course Notes, 1–44.

Franseen, E. K., Byrnes, A. P., Cansler, J. R., Steinhauff, D. M., and T. R. Carr, 2004, The geology of Kansas – Arbuckle group: Current Research in Earth Sciences, Kansas Geological Survey Bulletin 250, part 2.

Goodman A., Hakala, A., Bromhal, G., Deel, D., Rodosta, T., Frailey, S., Small, M., Allen D., Romanov, V., Fazio, Huerta, N., McIntyre, D., Kutchko, B., and G. Guthrie, 2011, U.S. DOE methodology for the development of geologic storage potential for carbon dioxide at the national and regional scale, International Journal of Greenhouse Gas Control, vol. 5, 4, 952-965, doi: 10.1016/j.ijggc.2011.03.010.

Gupta, M., and B. Hardage, 2017, Improved reservoir delineation by using SV-P seismic data in Wellington field, Kansas, SEG Technical Program Expanded Abstracts, 5182-5186, doi: 10.1190/segam2017-17559574.1

Gupta, M., K. Spikes, and B. Hardage, 2017, Characterization of naturally fractured Arbuckle Group in the Wellington Field, Kansas, using S-wave amplitude variation with offset, Interpretation 5, T49-T63, doi: 10.1190/INT-2016-0061.1.

Holubnyak, Y., E. Williams, L. Watney, T. Bigdoli, J. Rush, M. Fazelalavi, and P. Gerlach, 2017, Calculation of CO2 Storage Capacity for Arbuckle Group in Southern Kansas: Implications for a Seismically Active Region, Energy Procedia, 114, 4679-4689, doi: 10.1016/j.egypro.2017.03.1599.

Johnson, K. S., and K. V. Luza, 2008, Earth sciences and mineral resources of Oklahoma: Oklahoma Geological Survey, Educational Publication 9, 1–22.

Keroher, R. P., and Kirby, J. J., 1948, Upper Cambrian and Lower Ordovician rocks in Kansas: Kansas Geological Survey, Bulletin 72, 140 p.

LoCricchio, E., 2012, Wash Play Overview, Anadarko Basin: Stratigraphic framework and controls on Pennsylvanian granite wash production, Anadarko Basin, Texas and Oklahoma: AAPG Search and Discovery Article #110163.

McConnell, D. A., M. J. Goyda, G. N. Smith, and J. P. Chitwood, 1989, Morphology of the frontal fault zone, southwest Oklahoma: Implications for deformation and deposition on the Wichita Uplift and Anadarko Basin: Geology, 18, no. 7, 34–637.

Merriam, D., F., 1963, The geologic history of Kansas: Kansas Geological Survey Bulletin, v. 162, 317 p.

Northcutt, R. A., and J. A. Campbell, 1995, Geology provinces of Oklahoma: Oklahoma Geological Survey Open-File Report 5–95.

Scheffer, A., 2012, Geochemical and microbiological characterization of the Arbuckle saline aquifer, a potential CO2 storage reservoir; Implications for hydraulic separation and caprock integrity: M.S. thesis, University of Kansas.

Schwab, D. R., Bidgoli, T. S., and Taylor, M. H., 2017, Characterizing the potential for injection-induced fault reactivation through subsurface structural mapping and stress field analysis, Wellington Field, Sumner County, Kansas. Journal of Geophysical Research: Solid Earth, 122, 10,132– 10,154, doi:10.1002/2017JB014071.

Sloss, L. L., 1988, Tectonic evolution of the craton in Phanerozoic time; in, Sedimentary Cover—North American Craton—U.S., L. L. Sloss, ed.: The Geological Society of America, The Geology of North America Volume D-2, p. 25-51.

Watney, W. L., and J. Rush, 2012, Small scale field test demonstrating CO2 sequestration in Arbuckle Saline Aquifer and by CO2-EOR at Wellington Field, Sumner County, Kansas: DOE Project Number DE-FE0006821, 28.

Zapata, Y., M.R. Kristensen, N. Huerta, C. Brown, C.S. Kabir, and Z. Reza, 2020, CO2 geological storage: Critical insights on plume dynamics and storage efficiency during long-term injection and post-injection periods, Journal of Natural Gas Science and Engineering, Vol 83, doi: 10.1016/j.jngse.2020.103542
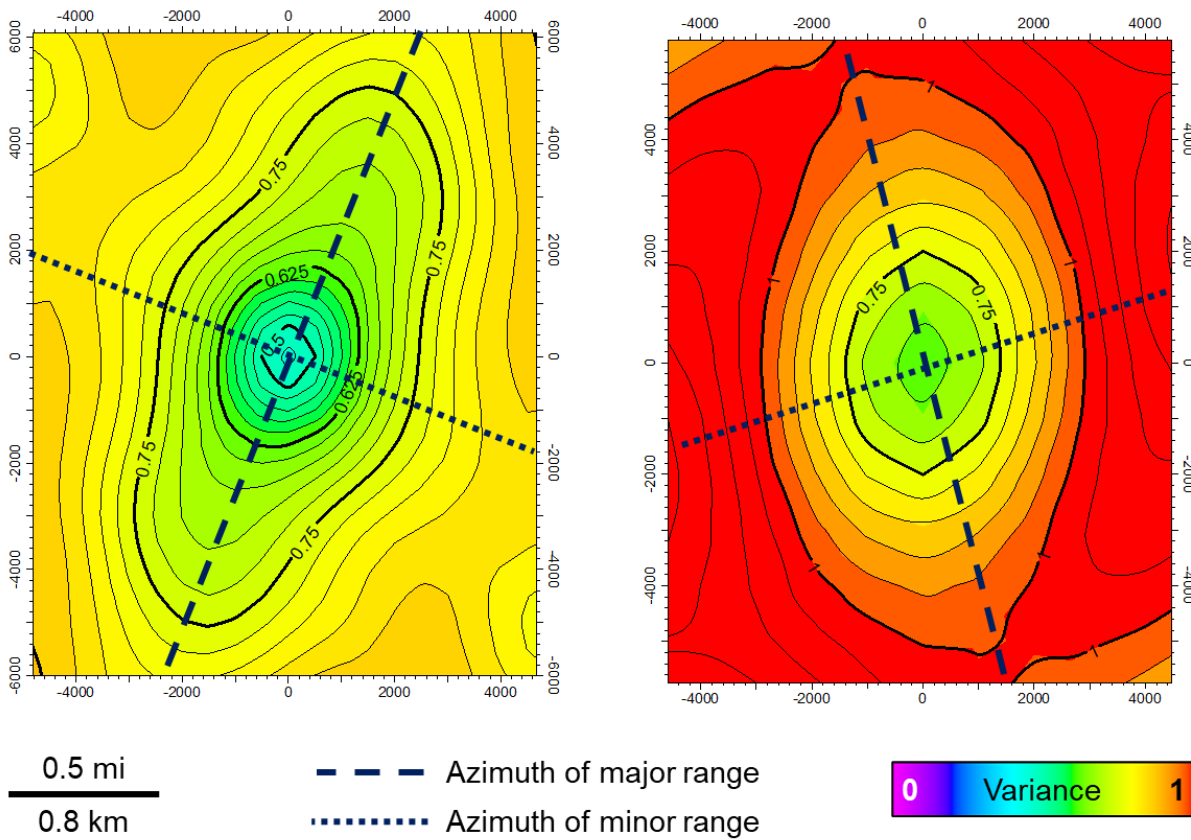
Appendix A

Figure 3-A. 1: Example variogram maps used to estimate the horizontal ranges and azimuth. The variogram map on the left is created from the petrofacies 1 probability volume for the Arbuckle zone C. The map on the right is extracted from the porosity trend volume and is used for estimating the ranges for the porosity modeling for the petrofacies 1. Maps show the greatest lateral continuity (azimuth of the major range) and the direction of the greatest lateral heterogeneity (azimuth of the minor range) for the particular petrofacies or porosity, shown by dashed and dotted lines, respectively.

Variogram Parameters for Petrofacies Modeling (Petrofacies 1)

Zone	Major (ft)	Minor (ft)	Vertical (ft)	Major Azimuth (Degrees from N)
Arbuckle C	5600	4041	8.46	23.7
Arbuckle B	5400	2260	5.61	13.2
Arbuckle A	3400	2014	6.64	34.3

Variogram Parameters for Petrofacies Modeling (Petrofacies 2)

Zone	Major (ft)	Minor (ft)	Vertical (ft)	Major Azimuth (Degrees from N)
Arbuckle C	5700	2400	8.52	-11
Arbuckle B	5413	2194	11.69	-23
Arbuckle A	5900	3100	13.6	-21

Variogram Parameters for Petrofacies Modeling (Petrofacies 3)

Zone	Major (ft)	Minor (ft)	Vertical (ft)	Major Azimuth (Degrees from N)
Arbuckle C	6700	2950	7.07	26.7
Arbuckle B	7100	2980	8.8	17
Arbuckle A	5600	4100	6.51	19.7

Appendix A-2: Variogram ranges and azimuth for the petrofacies model separated by zone. Horizontal and vertical ranges were defined for each zone and each petrofacies. Vertical ranges were estimated from the petrofacies logs. The horizontal ranges and azimuth were estimated from the variogram maps.

Variogram Parameters for Porosity Modeling (Petrofacies 1)

Zone	Major (ft)	Minor (ft)	Vertical (ft)	Major Azimuth (Degrees from N)
Arbuckle C	5300	2960	6.73	-12
Arbuckle B	4700	4000	4.49	4.8
Arbuckle A	6900	4500	6.13	-4

Variogram Parameters for Porosity Modeling (Petrofacies 2)

Zone	Major (ft)	Minor (ft)	Vertical (ft)	Major Azimuth (Degrees from N)
Arbuckle C	5300	2960	5.64	-12
Arbuckle B	4700	4000	6.12	4.8
Arbuckle A	6900	4500	11.17	-4

Variogram Parameters for Porosity Modeling (Petrofacies 3)

Zone	Major (ft)	Minor (ft)	Vertical (ft)	Major Azimuth (Degrees from N)
Arbuckle C	5300	2960	5.35	-12
Arbuckle B	4700	4000	7.75	4.8
Arbuckle A	6900	4500	8.1	-4

Appendix A-3: Variogram ranges and azimuth for the total porosity model separated by zone. Horizontal range and azimuths were extracted from the variogram maps created from the porosity trend volume. The vertical ranges were estimated through variography for each zone by petrofacies.

Variogram Parameters for Permeability Modeling (Petrofacies 1)

Zone	Major (ft)	Minor (ft)	Vertical (ft)	Major Azimuth (Degrees from N)
Arbuckle C	5300	2960	5.79	-12
Arbuckle B	4700	4000	6.06	4.8
Arbuckle A	6900	4500	5.03	-4

Variogram Parameters for Permeability Modeling (Petrofacies 2)

Zone	Major (ft)	Minor (ft)	Vertical (ft)	Major Azimuth (Degrees from N)
Arbuckle C	5300	2960	6.03	-12
Arbuckle B	4700	4000	6.06	4.8
Arbuckle A	6900	4500	5.73	-4

Variogram Parameters for Permeability Modeling (Petrofacies 3)

Zone	Major (ft)	Minor (ft)	Vertical (ft)	Major Azimuth (Degrees from N)
Arbuckle C	5300	2960	4.85	-12
Arbuckle B	4700	4000	5.73	4.8
Arbuckle A	6900	4500	5.98	-4

Appendix A-4: Variogram ranges and azimuth for the permeability model separated by zone. Horizontal range and azimuths were extracted from the variogram maps created from the porosity trend volume. The vertical ranges were estimated through variography for each zone by petrofacies.

Appendix B
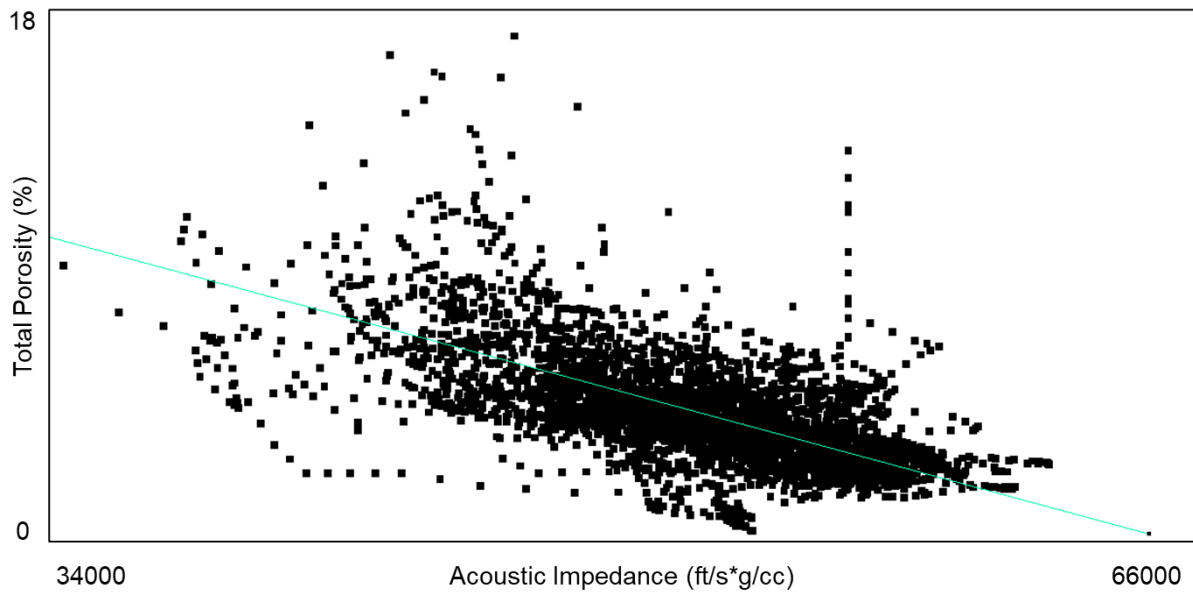
$$\text{Total Porosity} = -3.45798{*}\,10^{-4} * \text{Acoustic Impedance} + 22.7636$$

Figure 3-B. 1: Linear relationship used to generate porosity trend volume for porosity modeling.

Appendix C

DEPTH (ft)	Na (mg/l)	Ca (mg/l)	Mg (mg/l)	Br (mg/l)	Cl (mg/l)	S04 (mg/l)
4147	31500	5030	880	120	65800	99
4390	17400	2150	460	75.9	32000	2524
4512	15900	1500	347	79.7	30500	590

Appendix C-1: Table showing the ion concentrations used for brine speciation of Arbuckle aquifer. Brine samples were collected from Berexco Wellington KGS #1-32 well at various depths within the Arbuckle group. (Taken from Kansas Geological Survey KGS brine database, URL=http://www.kgs.ku.edu/Magellan/Brine/index.html, Accessed: March 2022).
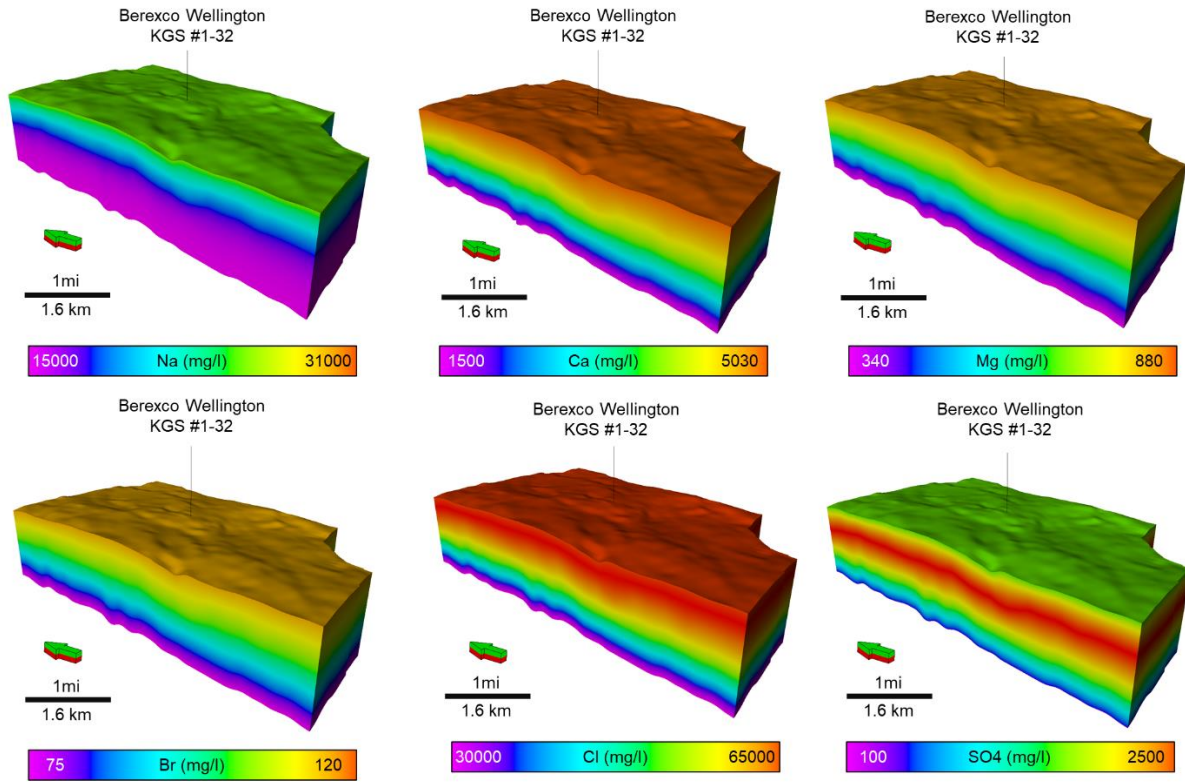
Figure 3-C. 1: 3D models of dissolved ion concentrations created by using the values shown in Appendix C-1.

Parameters		Value
Pressure	At the datum depth of 4169 ft (1270m)	144 bar (2093 psi)
Temperature		60 deg C (140 degF)
Compaction	Reference Pressure	230 bar (3335.8 psi)
	Rock Compressibility	6e-5 1/bar (4.1e-6 1/psi)
Relative Permeability Parameters	Irreducible water saturation	0.017, 0.095, and 0.19 for each petrofacies 1,2 and 3
	CO2 Corey exponent	4.5, 3.9, and 3.45 for each petrofacies 1,2 and 3
	Water Corey exponent	1.91 for all petrofacies

Appendix C-2: Summary of parameters used in dynamic simulation. Relative permeability values

for CO_2-brine system were taken and modified from Watney and Rush (2012).

Appendix D
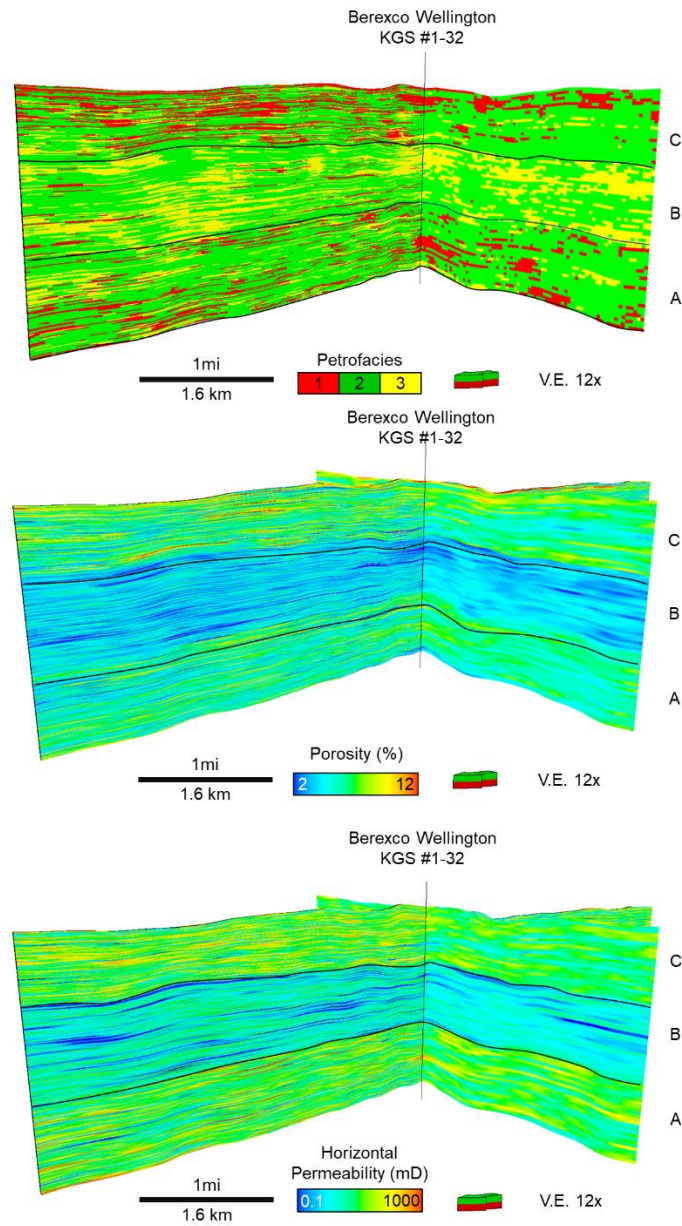
Figure 3-D. 1: Original petrofacies, porosity and permeability models with side-by-side comparison with the upscaled version used for the dynamic simulation.

137
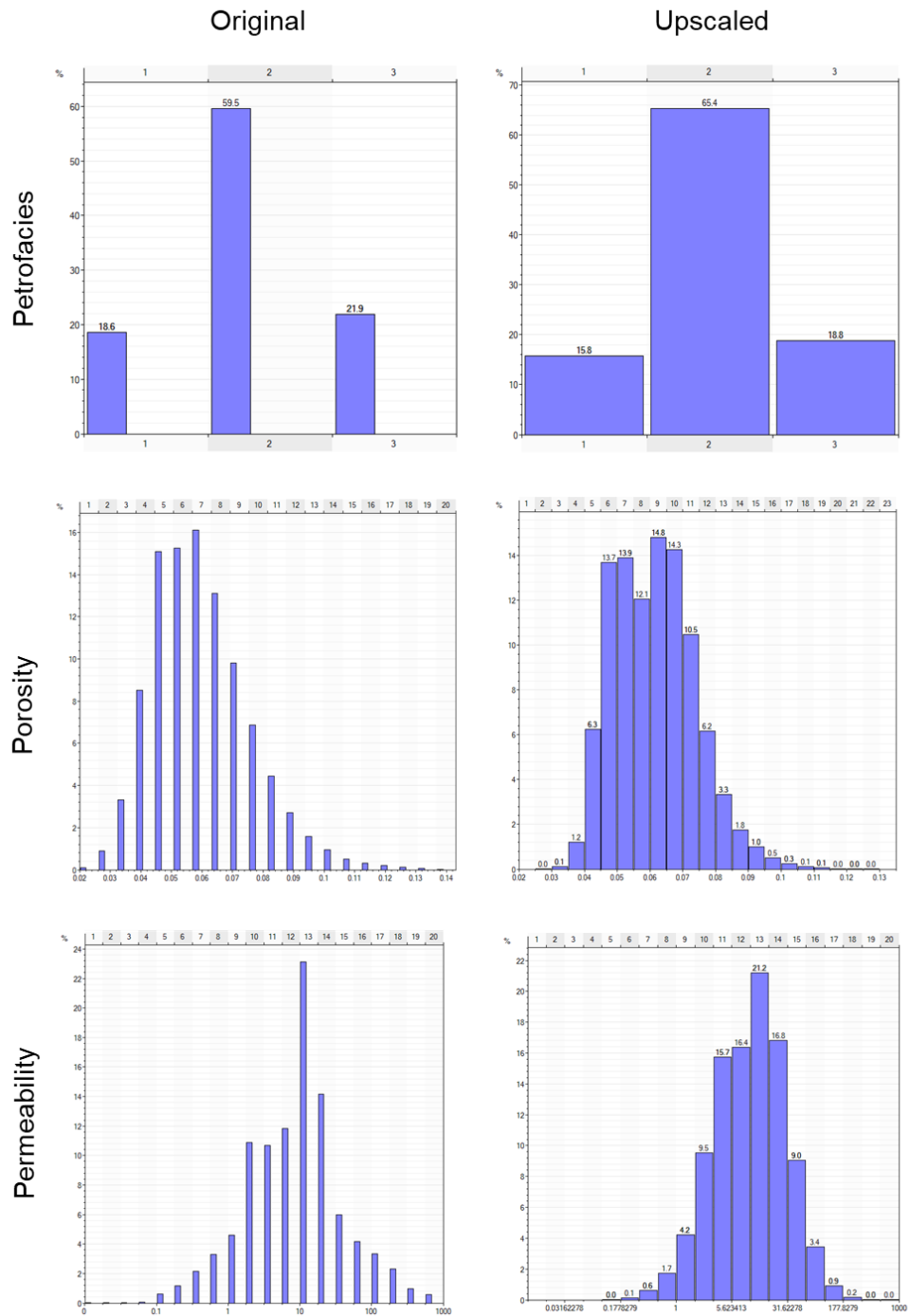
Figure 3-D. 2: Petrofacies, porosity and permeability model histograms for the original and upscaled models.
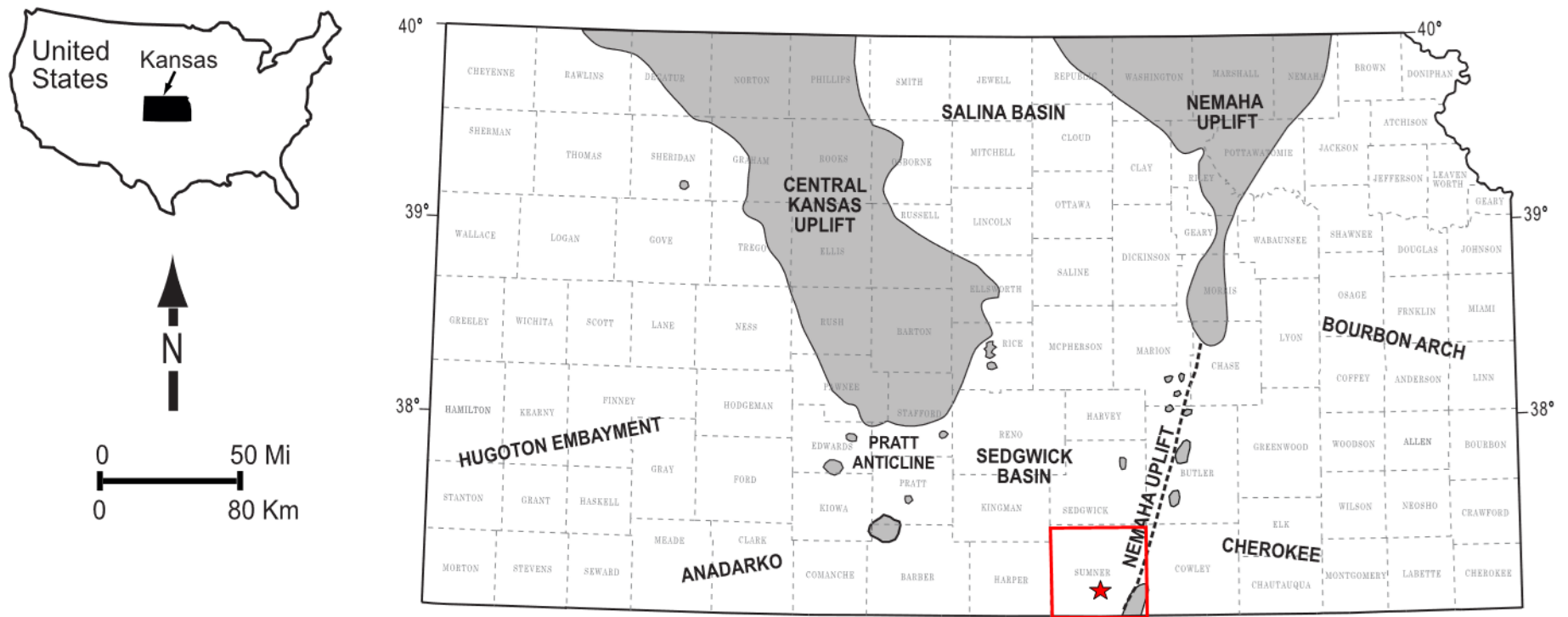
Chapter 3 Figures

Figure 3.1: Regional map showing the subsurface structural features of Kansas. The study area is located in Sumner County, Kansas (Red square). The approximate location of the study area is denoted by the red star (Modified after Dutton, 1984; Campbell et al., 1988; McConnell, 1989; Northcutt and Campbell, 1995; Johnson and Luza, 2008; LoCriccho, 2012).
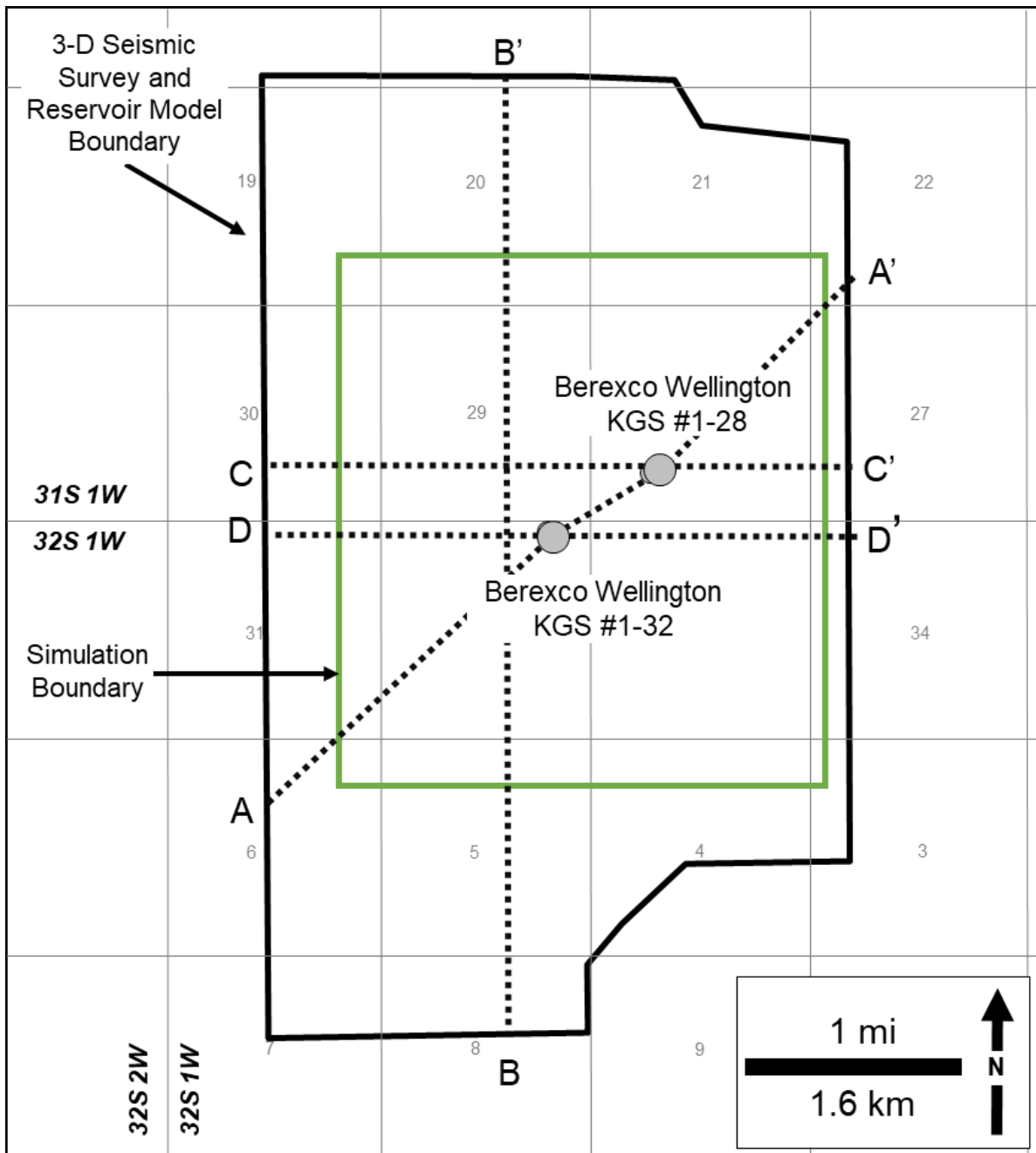
Figure 3.2: Study area base map showing well locations, seismic survey, modeling and simulation boundaries, and cross sections of interest. Seismic section A-A' is shown in Figure 3. Impedance and 3D model grid cross sections B-B' is shown in Figures 5 and 11. Petrofacies prediction volume cross sections for C-C' are shown in Figure7. Reservoir model cross sections D-D' are shown in Figure13. The map location is shown in Figure 1.
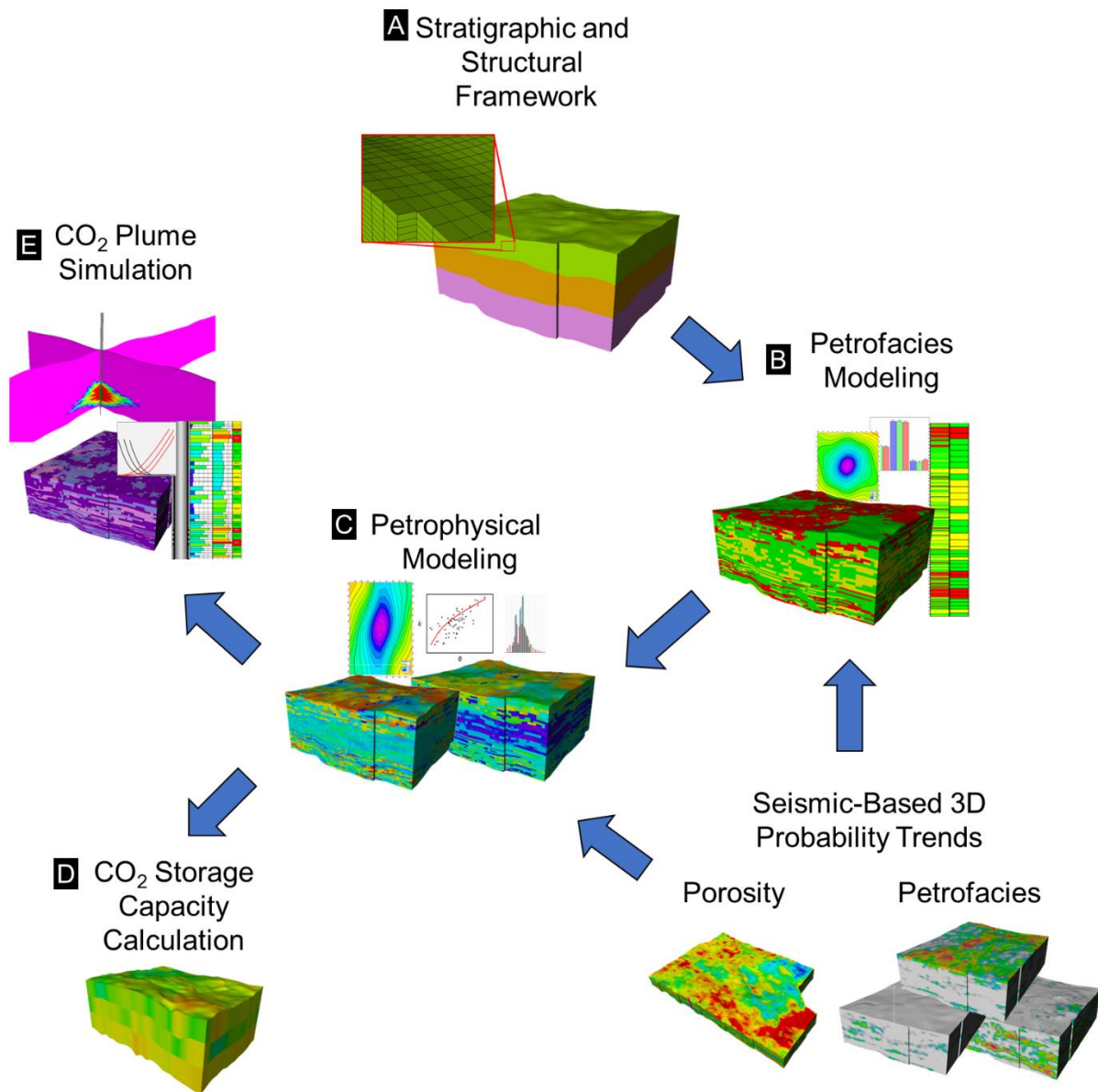
Figure 3.3: Generalized Workflow showing the main steps followed in this study. A) Structural and stratigraphic framework (3D Grid) generation, B) Petrofacies modeling, C) Porosity and permeability modeling, D) CO2 storage capacity estimation, and E) Dynamic simulations for plume mapping.
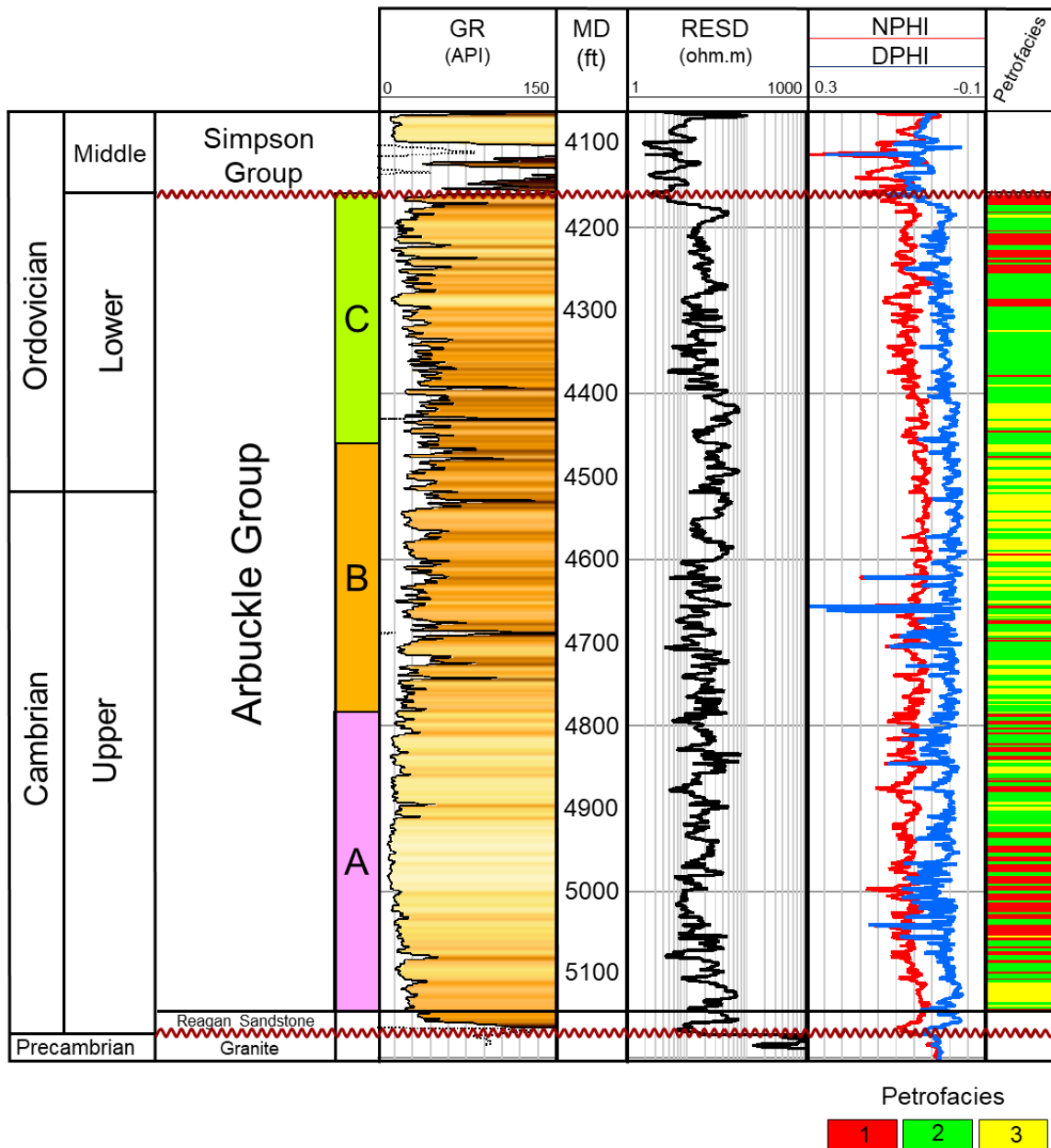
Figure 3.4: Generalized stratigraphic column tied to Berexco Wellington KGS #1-32 type log. (Stratigraphic column is modified After Baars et al., 2001 and Schwab et al.,2017). Three Arbuckle intervals (A, B, and C) are present. Gamma Ray (GR), Deep Resistivity (RESD), Neutron Porosity (NPHI), and Density Porosity (DPHI) are shown. The right-most track shows the petrofacies log used in the seismic-constrained modeling.
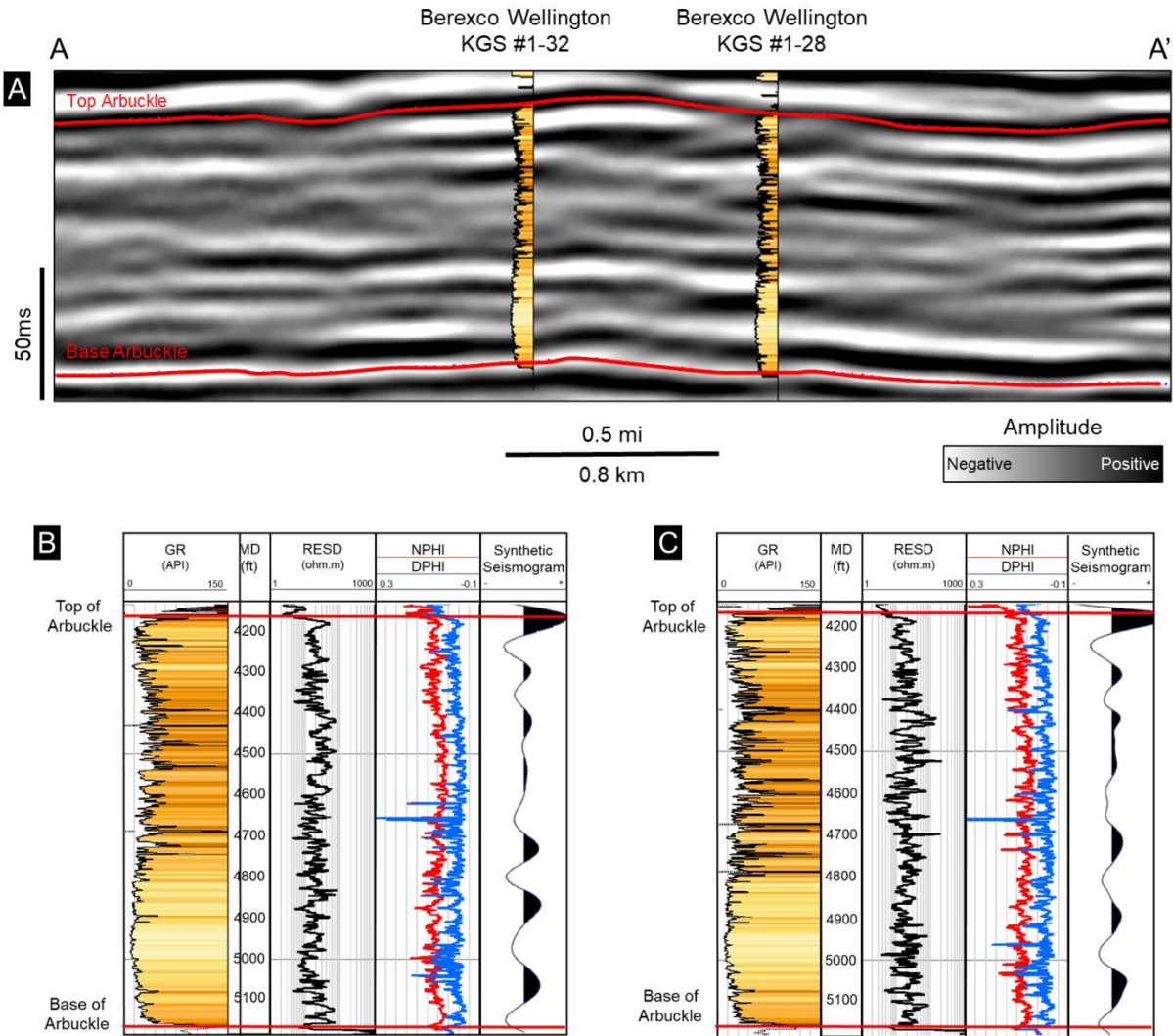
Figure 3.5: (A) Southwest-Northeast arbitrary line (A-A') showing the seismic amplitude volume and wells with gamma-ray logs used in the horizon interpretation of the Arbuckle interval. (B and C) type logs showing the well log and synthetic seismogram responses of the study interval, where the top of the Arbuckle shows a strong positive (peak) and the base of the Arbuckle shows a strong negative (trough) seismic response. The location of the cross-section is shown in Figure 2.
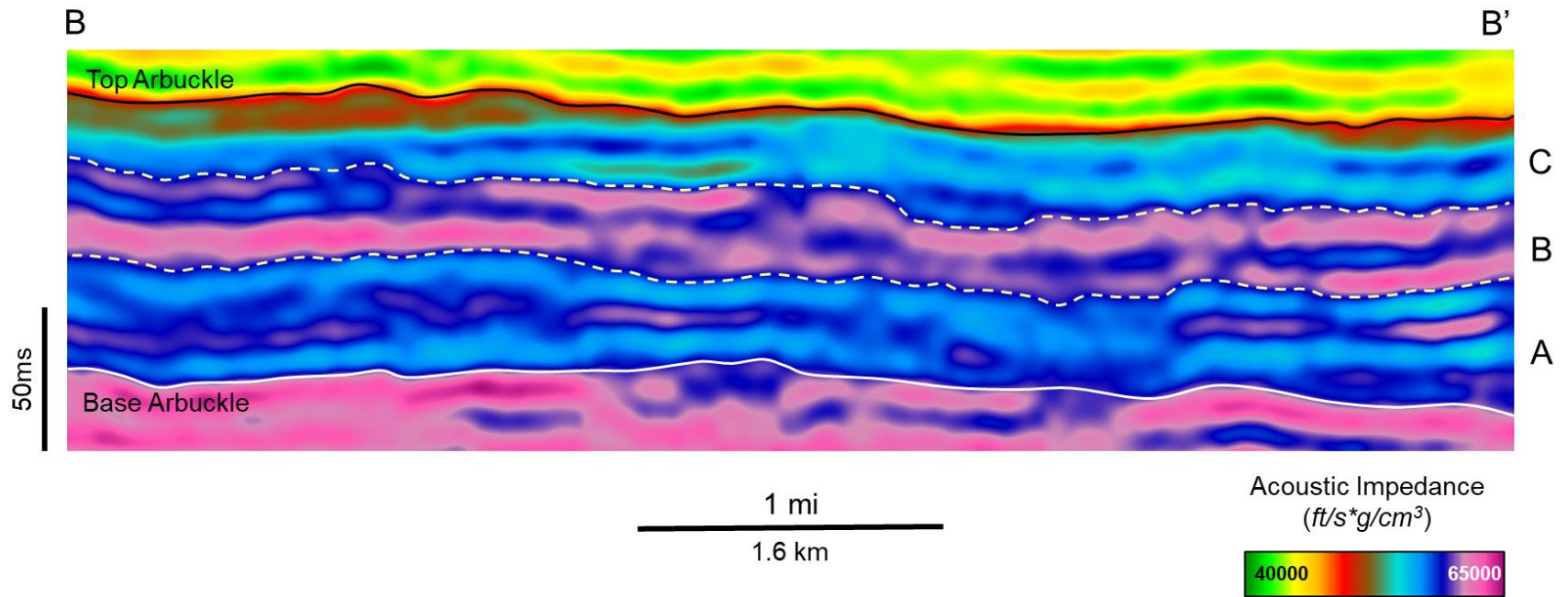
Figure 3.6: South-North oriented cross-section (B-B') from the acoustic impedance volume. Impedance volume was used to help the interpretation of surfaces that subdivide the Arbuckle group (zones A, B and C) for the structural and stratigraphic framework. The location of cross section is shown in Figure 2.
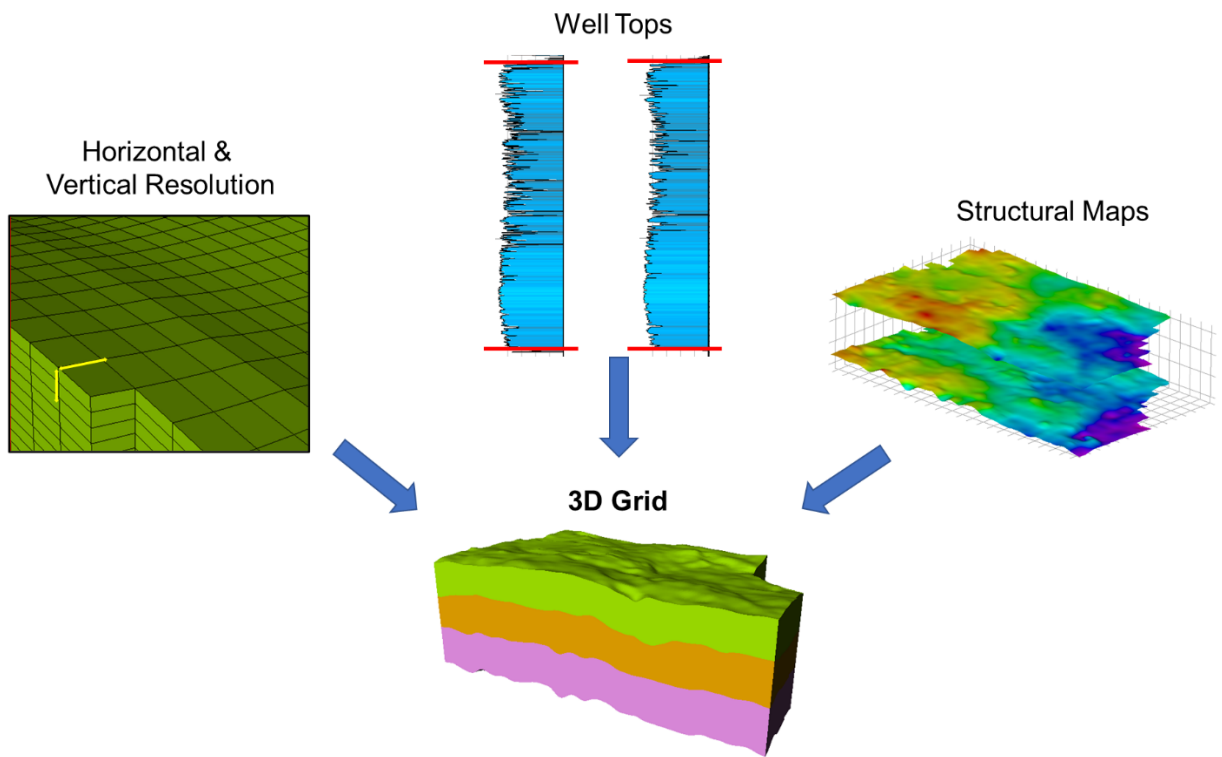
Figure 3.7: Schematic diagram showing elements used to constrain the construction of the three-dimensional grid.
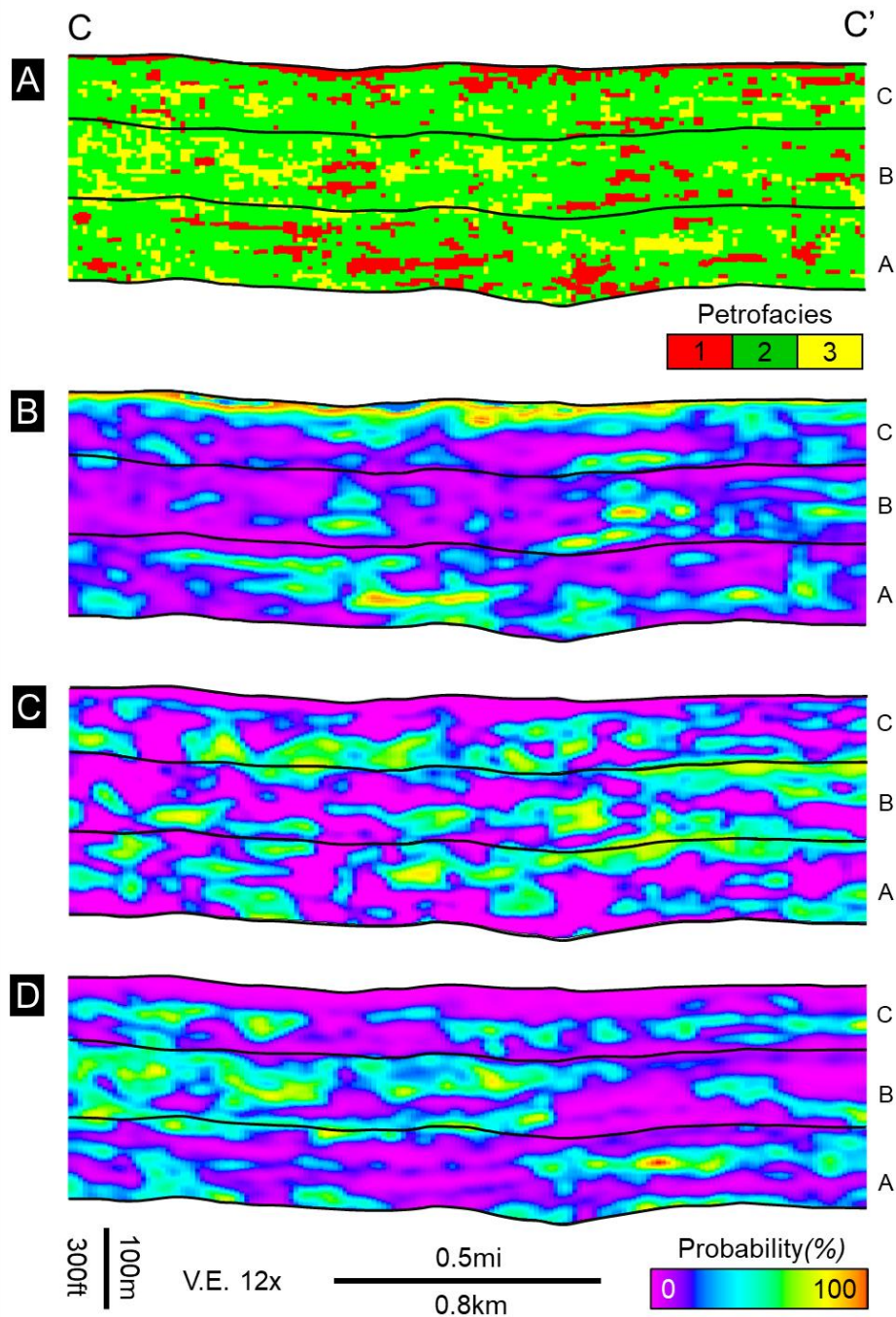
Figure 3.8: East-West oriented cross-sections (C – C') from the random forest petrofacies prediction volumes re-sampled on the 3D grid. A) Most likely petrofacies prediction, B) Probability of petrofacies 1, C) Probability of petrofacies 2, and D) Probability of petrofacies 3. The location of cross section is shown in Figure 2
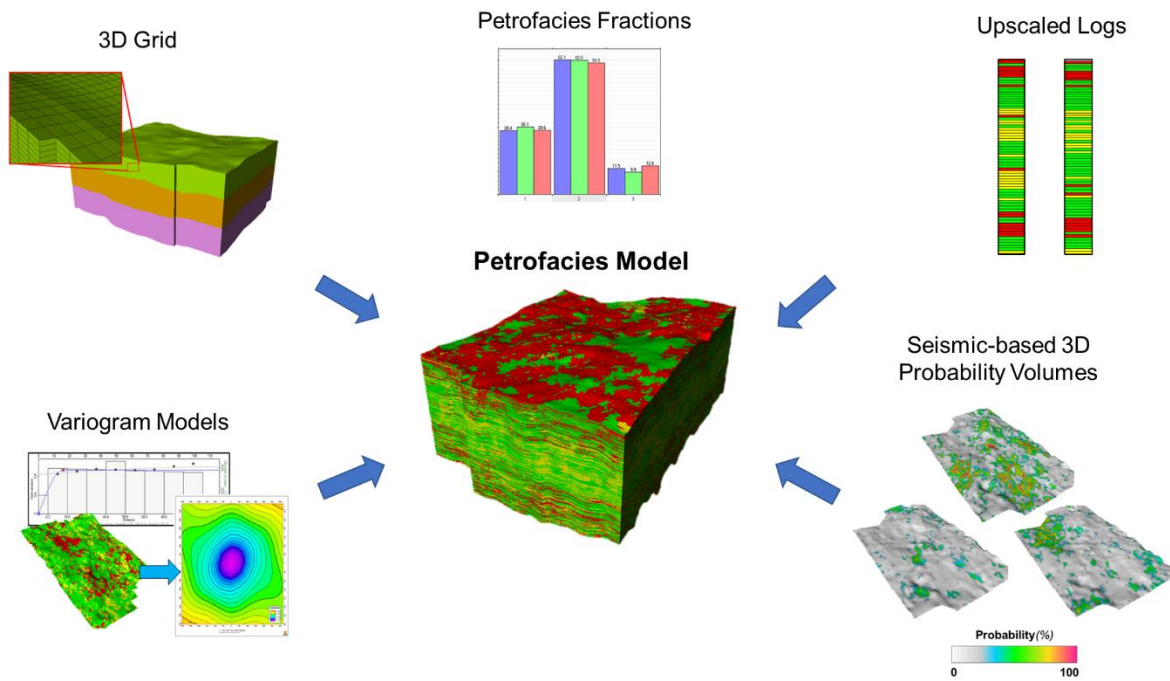
3D Grid

Petrofacies Fractions

Upscaled Logs

Petrofacies Model

Variogram Models

Seismic-based 3D
Probability Volumes

Probability *(%)*

0   100

.

Figure 3.9: Schematic diagram showing the various data used to constrain the generation of the three-dimensional petrofacies model.
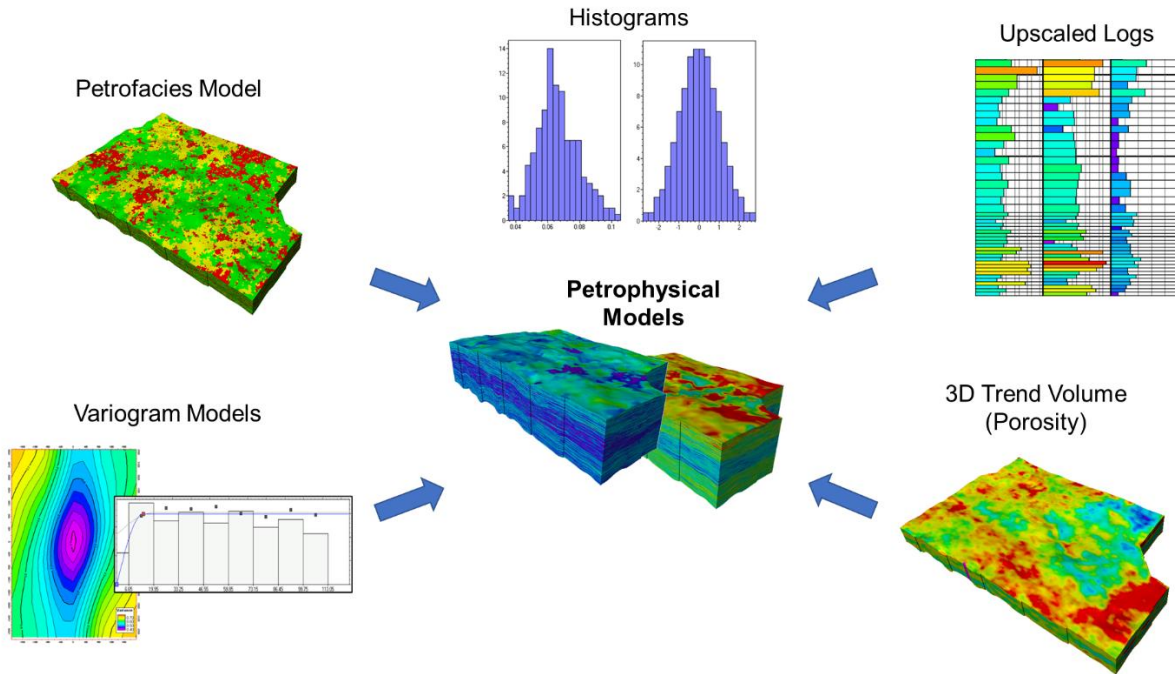
Figure 3.10: Schematic diagram showing the data for constraining the three-dimensional porosity and permeability models.
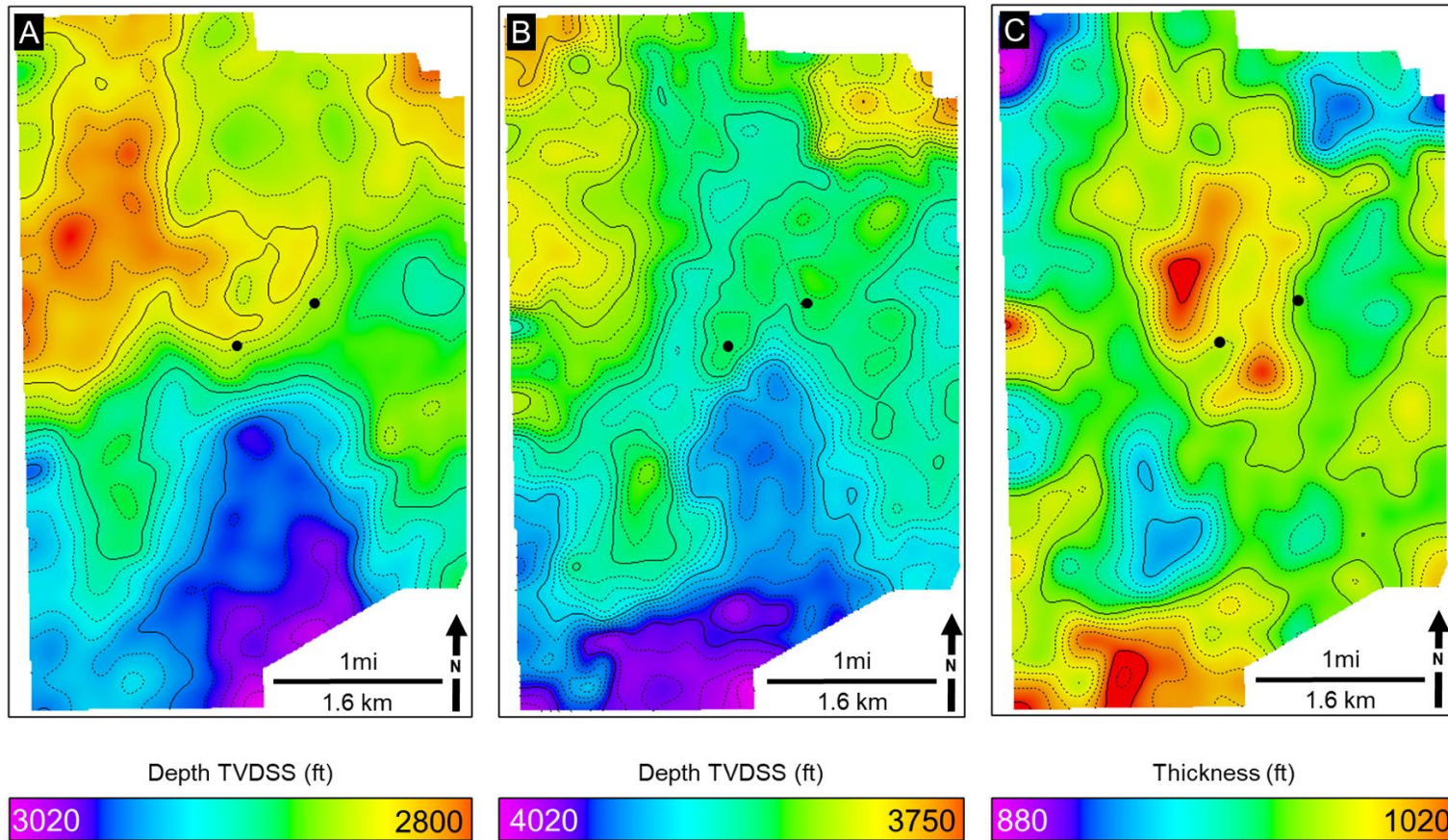
Figure 3.11: Structure maps for (A) the Top of the Arbuckle and (B) the Base of the Arbuckle as picked from the seismic volume and depth converted from tops picked in wells. (C) Arbuckle Isopach Map. Arbuckle interval can be seen structurally shallowing towards the north and northwest. In the study area, the Arbuckle thickness varies between 880-1020 ft (268 to 310 m) and thickens towards the center and the southern edge. The contour interval is 10 ft (3.04 m).
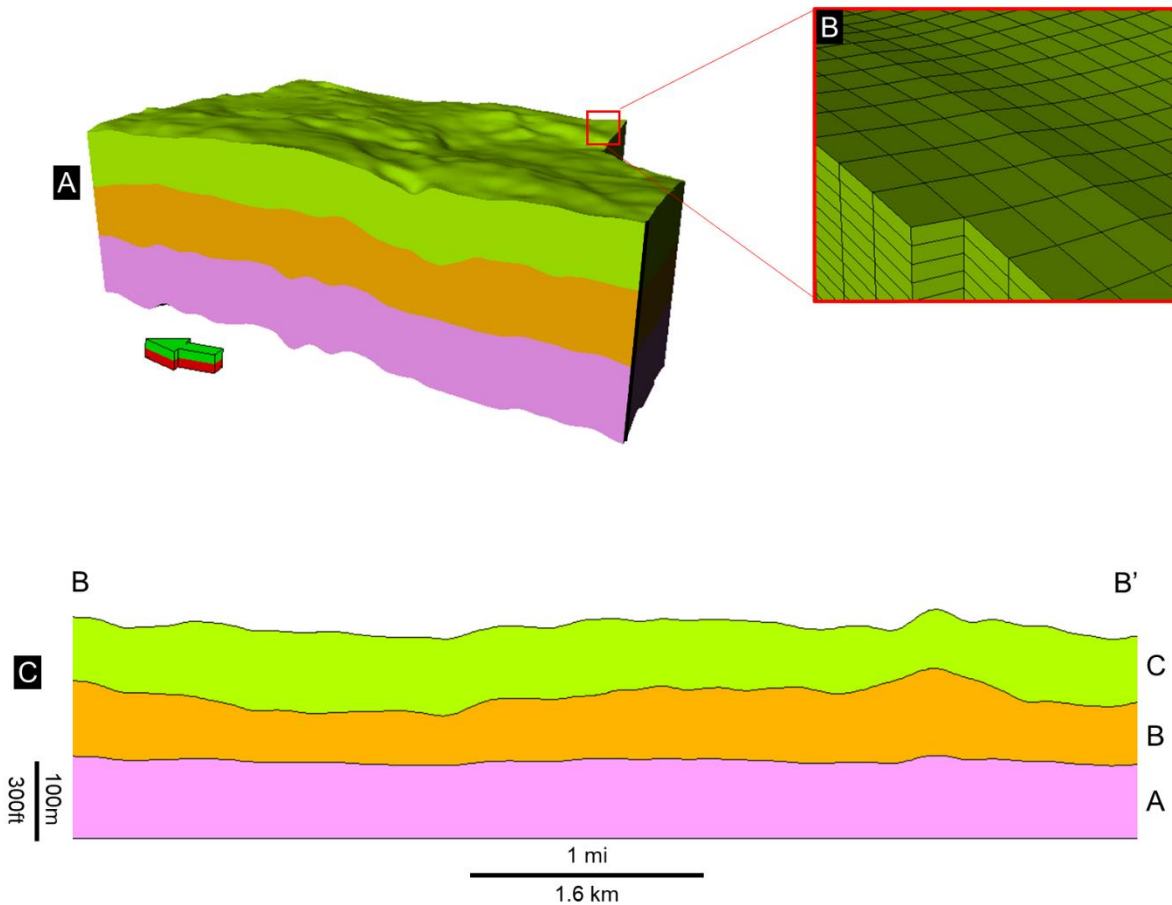
Figure 3.12: (A) Three-dimensional model representing the structural and stratigraphic framework of the Arbuckle group. The 3D grid covers an area of 10.4 mi2 (26.9 km2). (B) The aerial cell dimensions correspond to the seismic bin size of 82.5 × 82.5ft (25 × 25 m) with an approximate cell/layer thickness of 2 ft (0.6 m). The grid is comprised of 179 x 289 x 450 cells in the I, J, and K directions, respectively, resulting in 23,278,950 cells with a proportional layering scheme. (C) South-North oriented cross-section (B-B') through the 3D grid flattened on the basement with 3X vertical exaggeration. The location of cross section is shown in Figure 2.
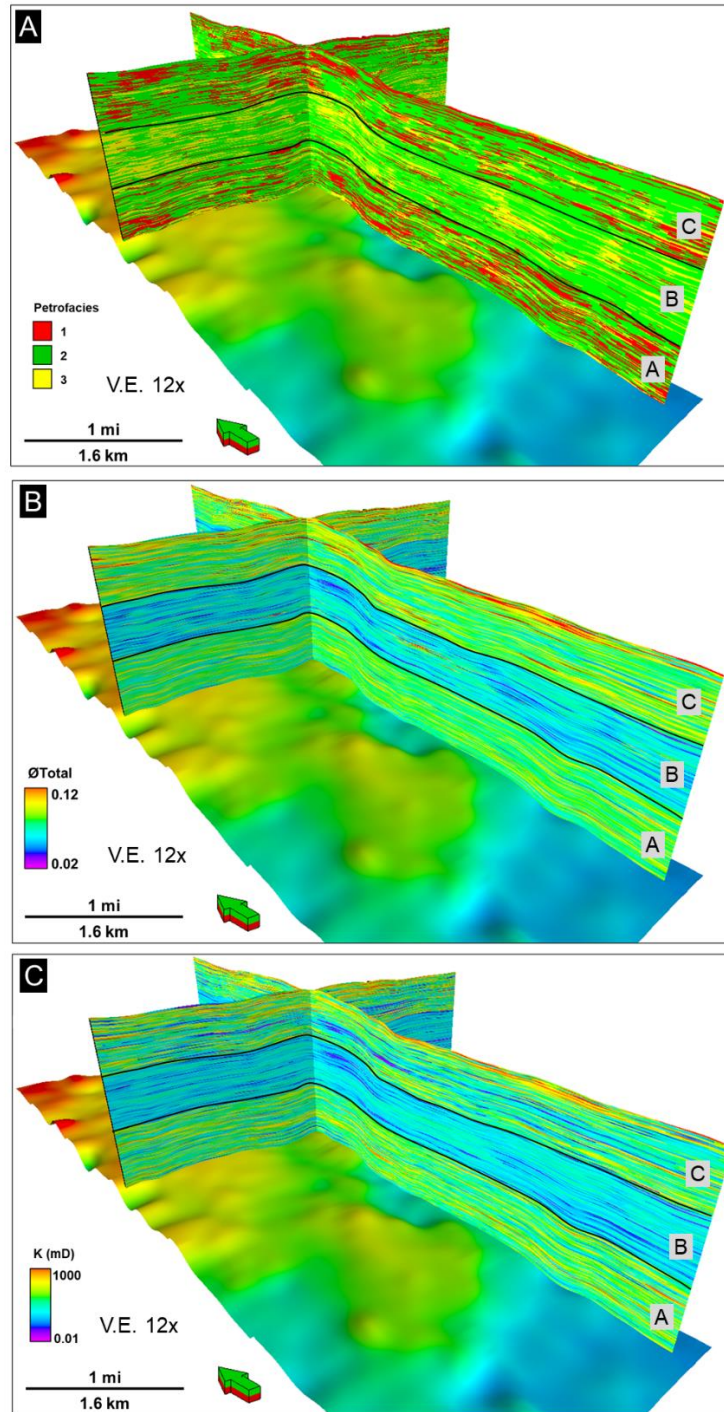
Figure 3.13: Perspective views of 3D model sections showing the spatial distribution of A) Petrofacies, B) Porosity, and C) Permeability. Base Arbuckle horizon is displayed.
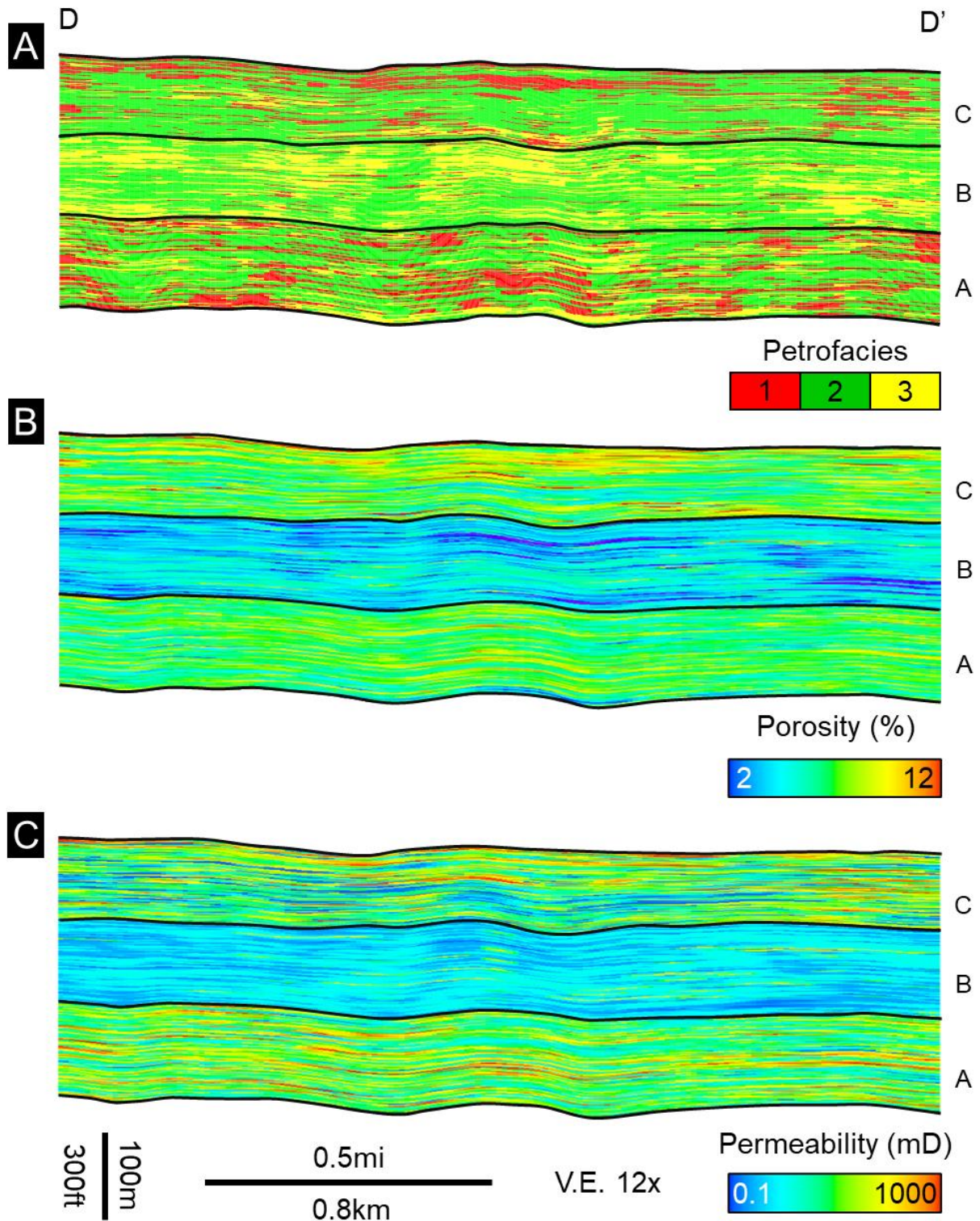
Figure 3.14: East-west oriented cross-sections (D – D') taken from the reservoir models showing the distribution of petrofacies and corresponding petrophysical property distribution. A)

Petrofacies distribution shows that the Arbuckle Zones A and C are mainly composed of petrofacies 1, while Zone B can be seen as abundant with petrofacies 2 and 3. B) Porosity distribution. High porosity values are observed at zones A and C, correlating with the high concentrations of the petrofacies 1. In contrast, Zone B has lower porosity values coinciding with the abundance of petrofacies 2 and 3. C) Permeability distribution shows a similar trend with the porosity, in which the high permeability values can be seen at zones A and C, and low permeability values are observed at Zone B as petrofacies 2 and 3 become more prominent. The location of cross section is shown in Figure 2.
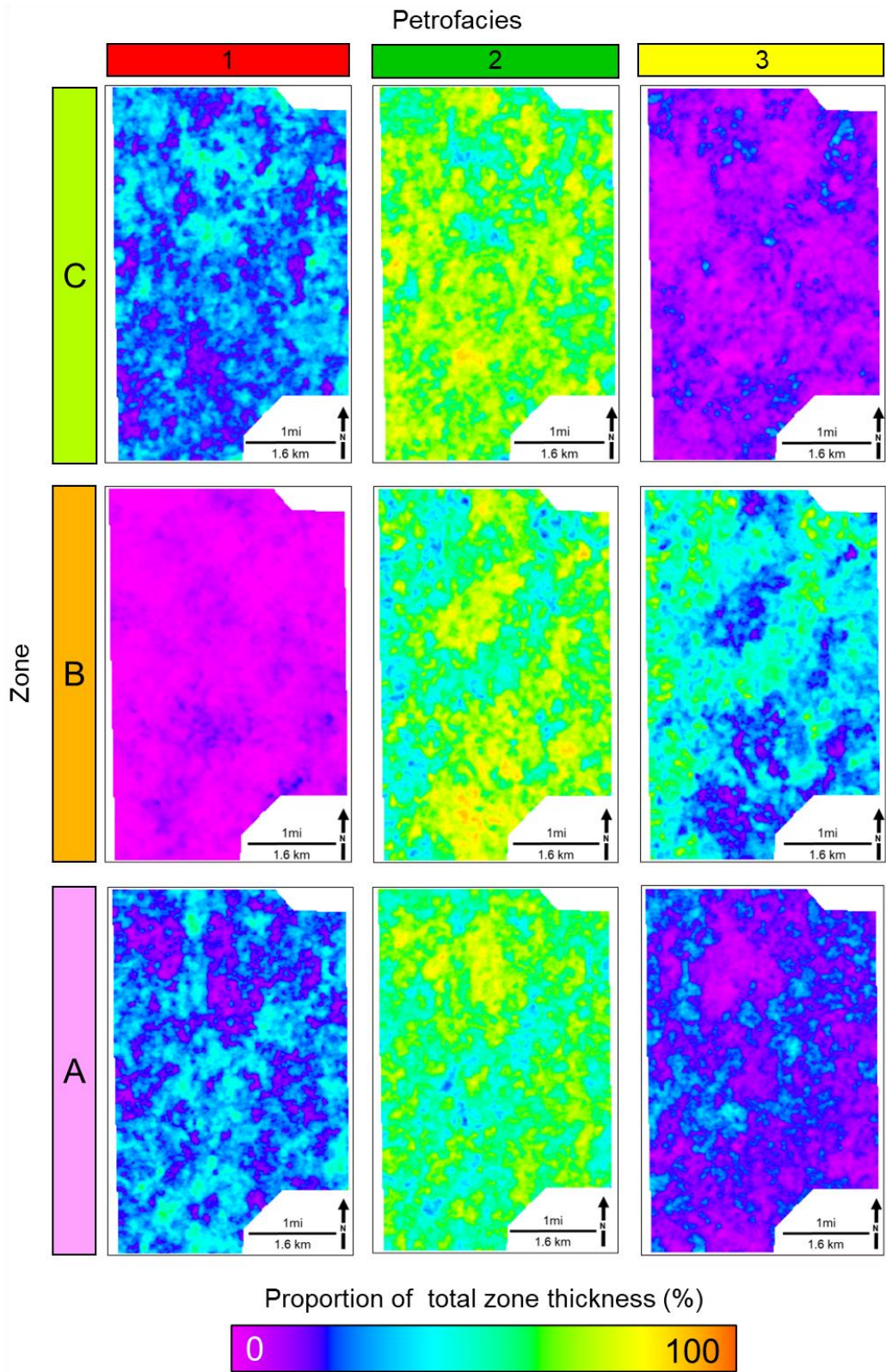
Petrofacies

154

Figure 3.15: Petrofacies proportion maps showing thickness of each petrofacies proportional to the individual zone thickness. Petrofacies 1 is mostly abundant at zones A and C, with a homogeneous spatial distribution. Petrofacies 2 and 3 can be seen dominating the Arbuckle zone B, and mainly concentrated on the central and the southeastern sections of the study area, showing northeast-southwest linear trend.
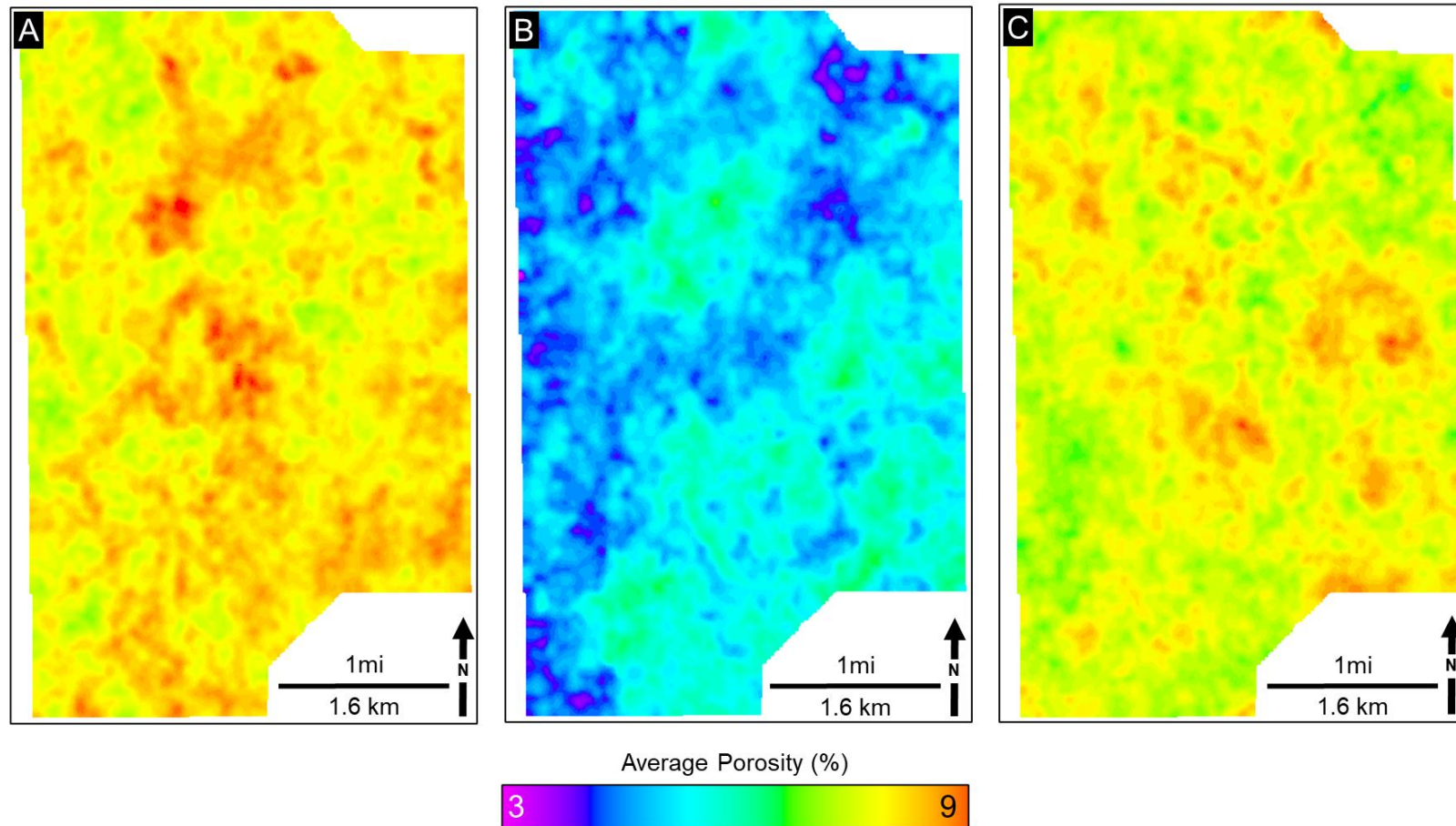
Figure 3.16: Average porosity maps for the Arbuckle zones A-C. Zones A and C exhibit high average porosity values (up to 8%). In contrast, Zone B has low average porosity values of up to 4%. Heterogeneous distribution of porosity values can also be observed.
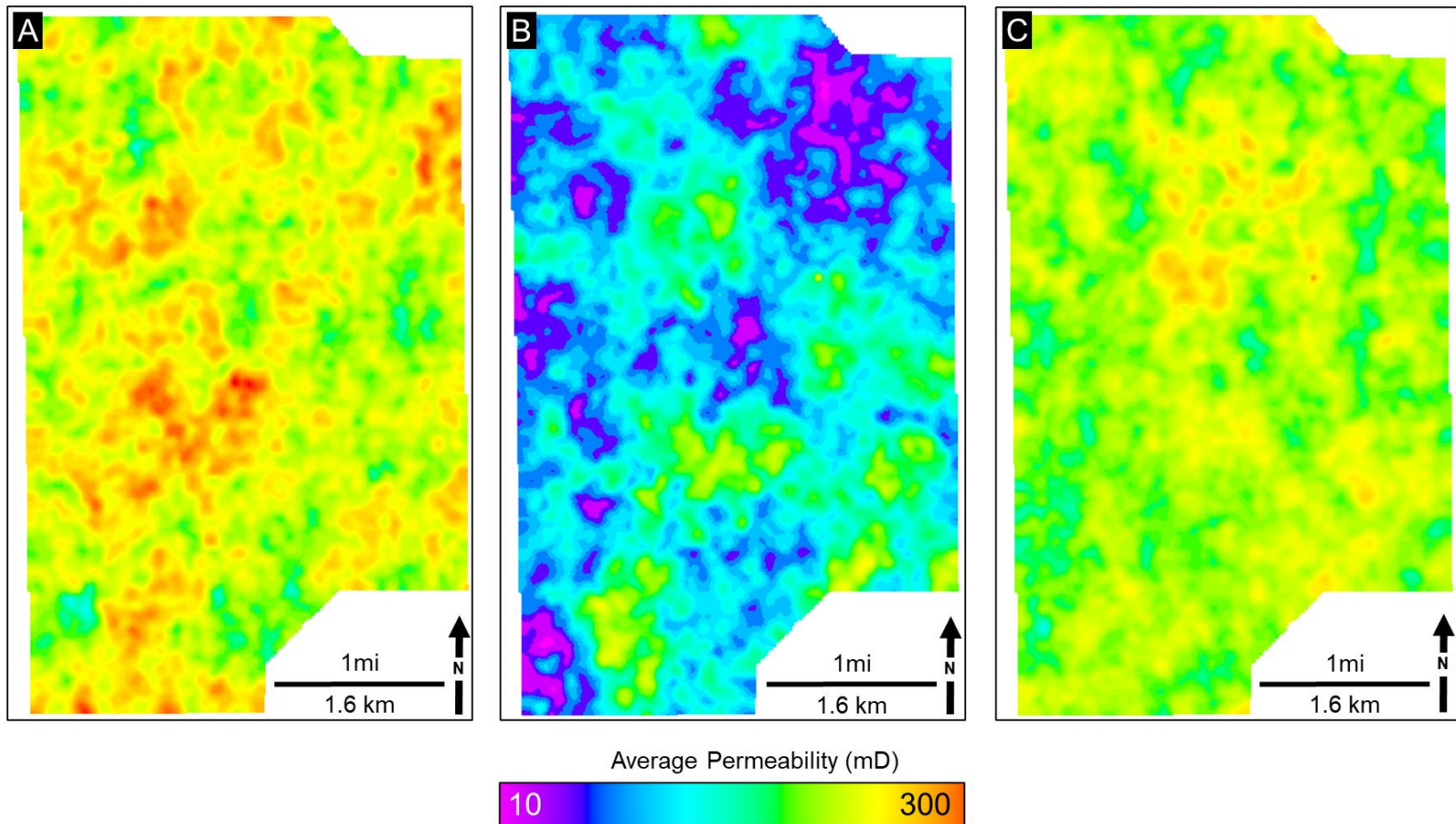
Figure 3.17: Average permeability maps for the Arbuckle zones A-C. Zones A and C exhibit high average permeability values (up to 300 mD). Zone B can be seen as having lower average permeability values up to 20mD.
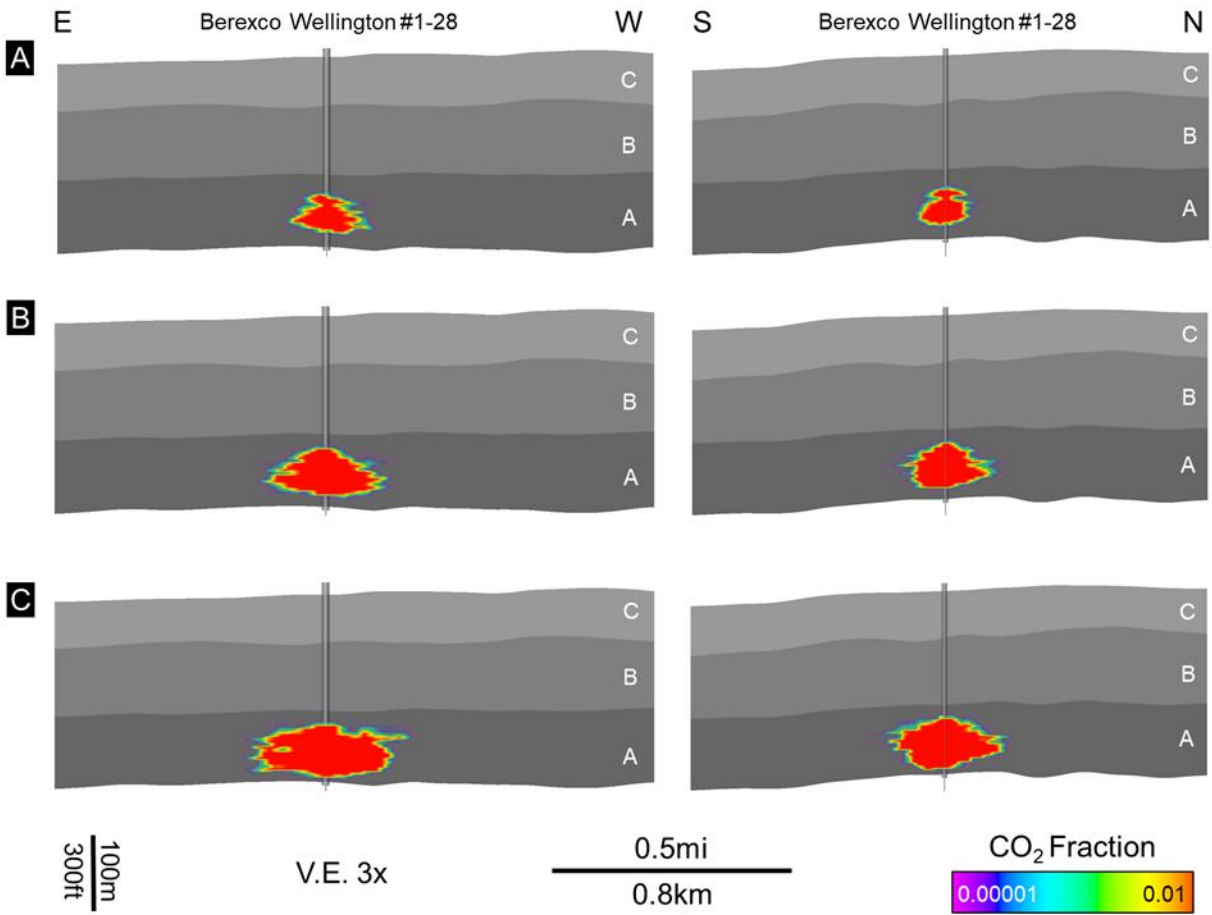
Figure 3.18: East-West and South-North oriented cross-sections from the dynamic simulation results showing the subsurface plume evolution during (A) 10, (B) 50, and (C) 100 years of CO_2 injection.
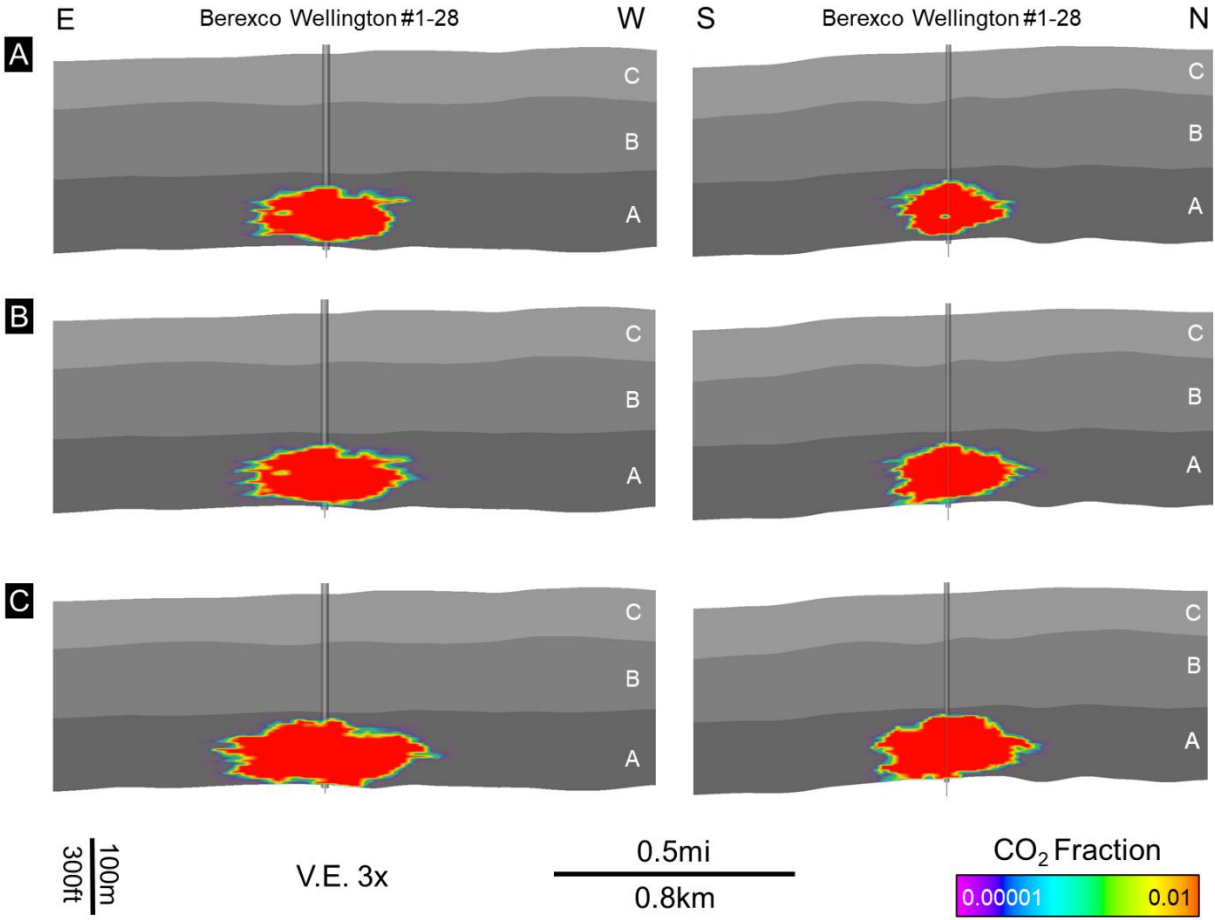
Figure 3.19: East-West and South-North oriented cross sections from the dynamic simulation results showing the subsurface plume evolution during (A) 10, (B) 50, and (C) 100 years of CO_2 post-injection periods.

CO₂ Fraction

0.5mi
0.8km
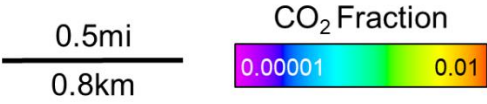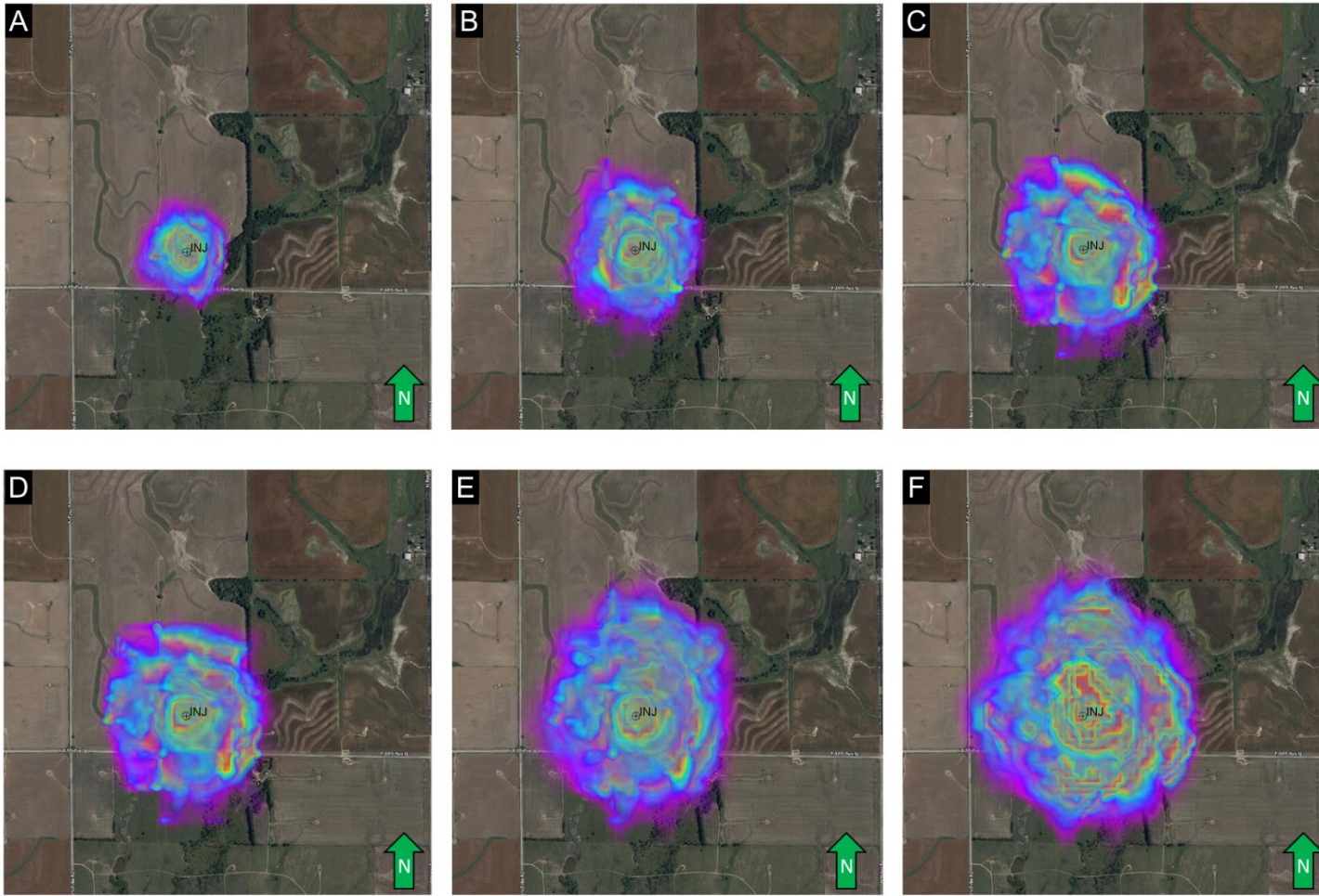
CO_2 Fraction
0.00001   0.01

Figure 3.20: Map views of subsurface CO_2 plume migration during 100-year injection and 100-year post-injection periods. Maps A through C show 10, 50, and 100 years of the injection period. Maps D through F show the plume migration at 10-, 50-, and 100-years post-injection periods, respectively.
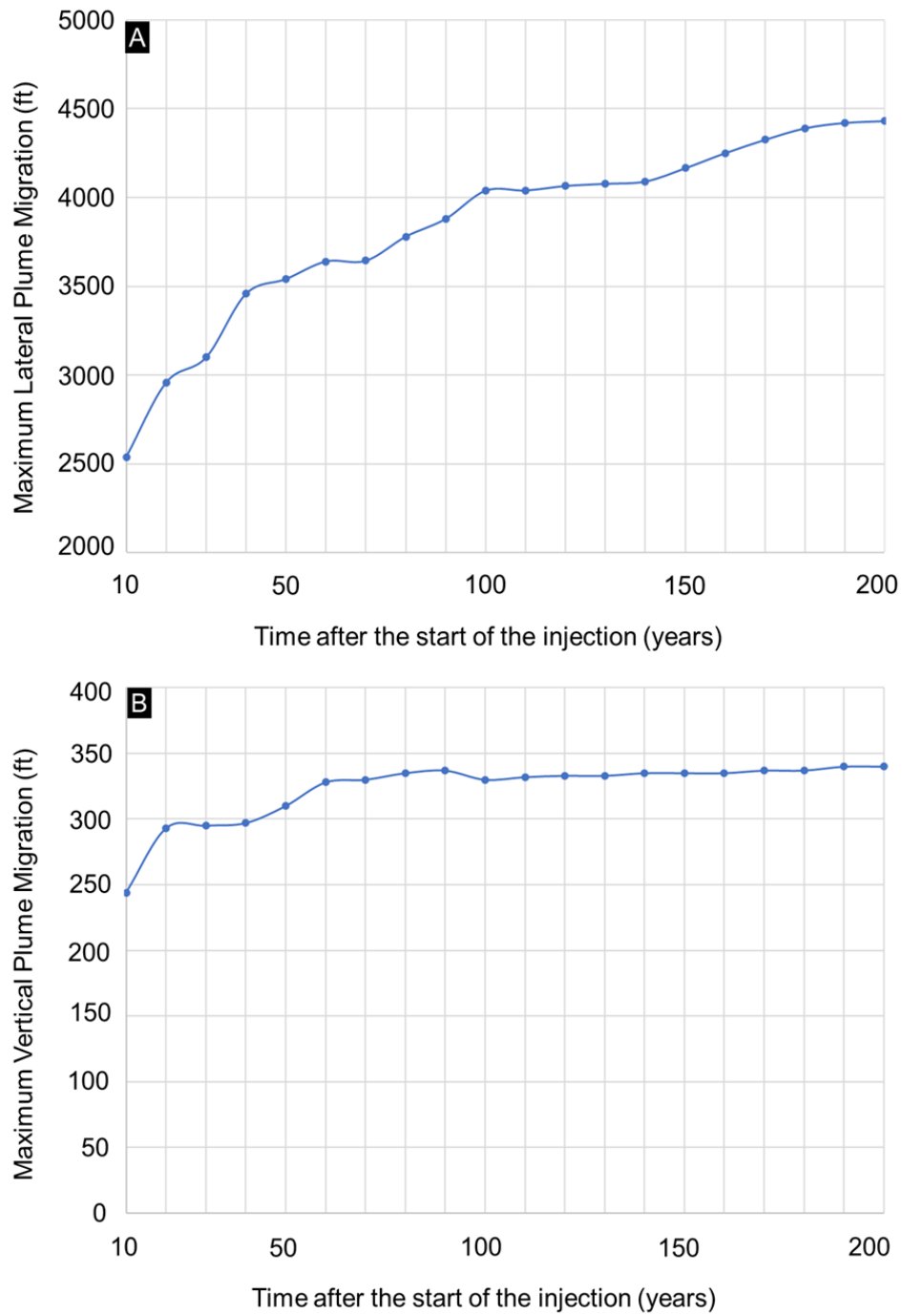
Figure 3.21: Maximum lateral and the vertical extent of the CO_2 plume through injection and post-injection periods. (A) The maximum lateral extent of the plume reaches 4450 feet (1356.36), and (B) the greatest vertical radius reaches up to 340 feet (103.63 m).
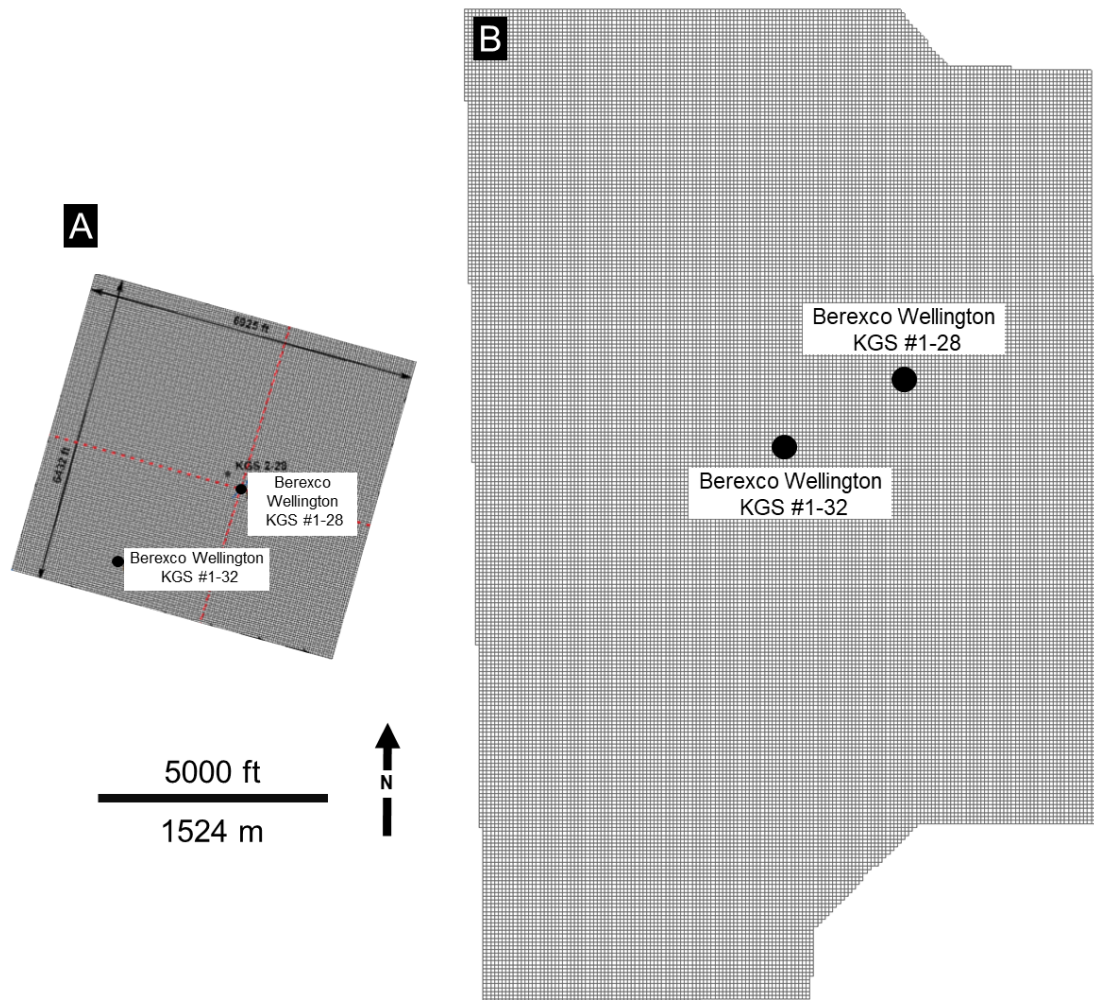
Figure 3.22: Map view comparison of 3D grids used in A) Watney and Rush (2012), and B) this study. The grid defined by Watney and Rush (2012) covers an area of 1.56 mi^2 (4.04 km^2)and made up of 706 x 654 x 79 cells in I, J, and K directions (total of 36,476,196 cells). The 3D grid defined in this study spans an area of approximately 10.4 mi^2 (26.9 km^2) and comprises of 179 x 289 x 450 cells in the I, J, and K directions, resulting in 23,278,950 cells.

163

Figure 3.23: East-west cross sections transecting through the Berexco Wellington KGS #1-28 Well showing the comparison of rock type models created by A) Watney and Rush (2012) and B) this study.

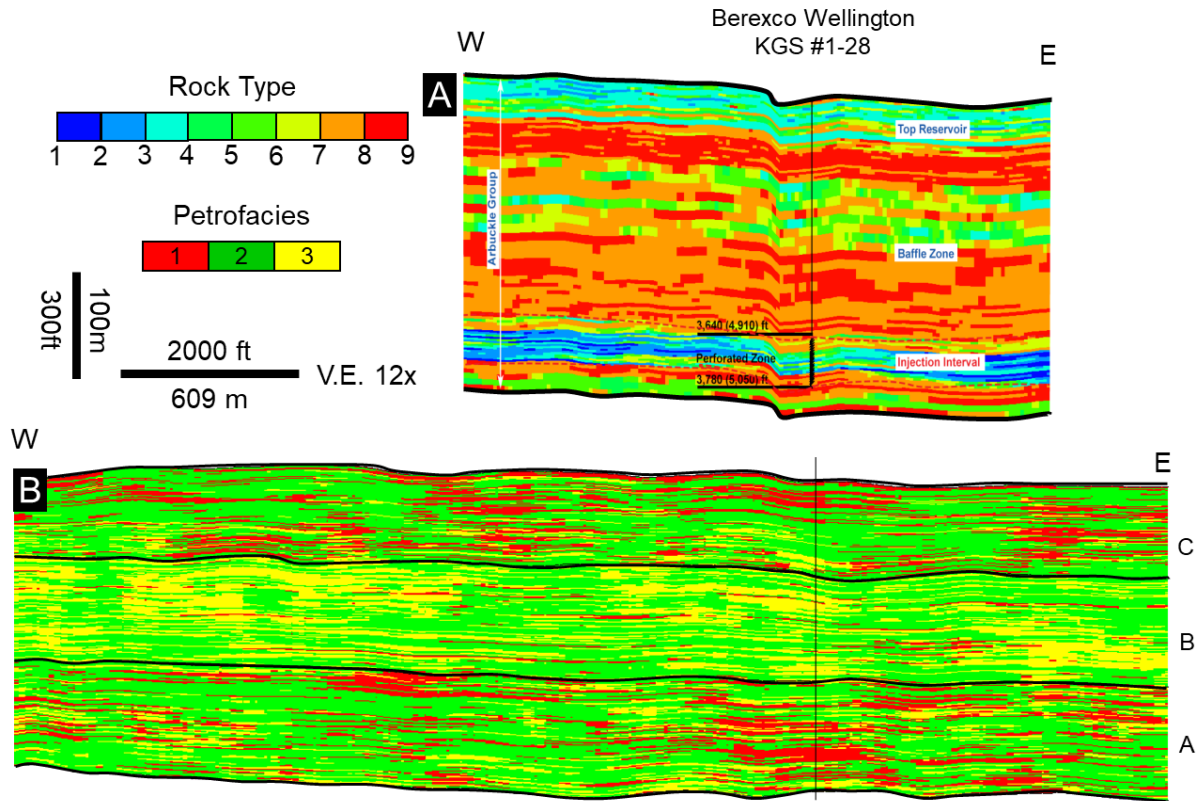**Figure 3.24:** North-south cross sections transecting through the Berexco Wellington KGS #1-28 Well showing the comparison of rock type models created by A) Watney and Rush (2012) and B) this study.

Figure 3.25: East-west cross sections transecting through the Berexco Wellington KGS #1-28 Well showing the comparison of horizontal permeability models created by A) Watney and Rush (2012) and B) this study.
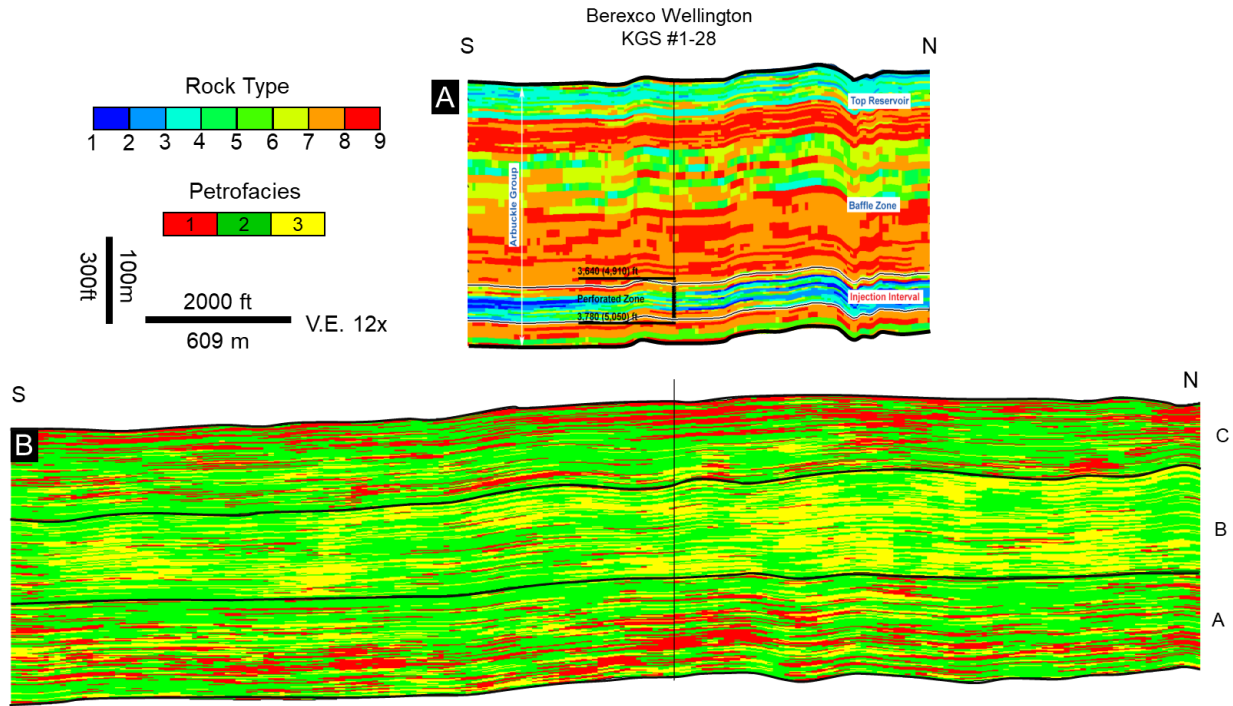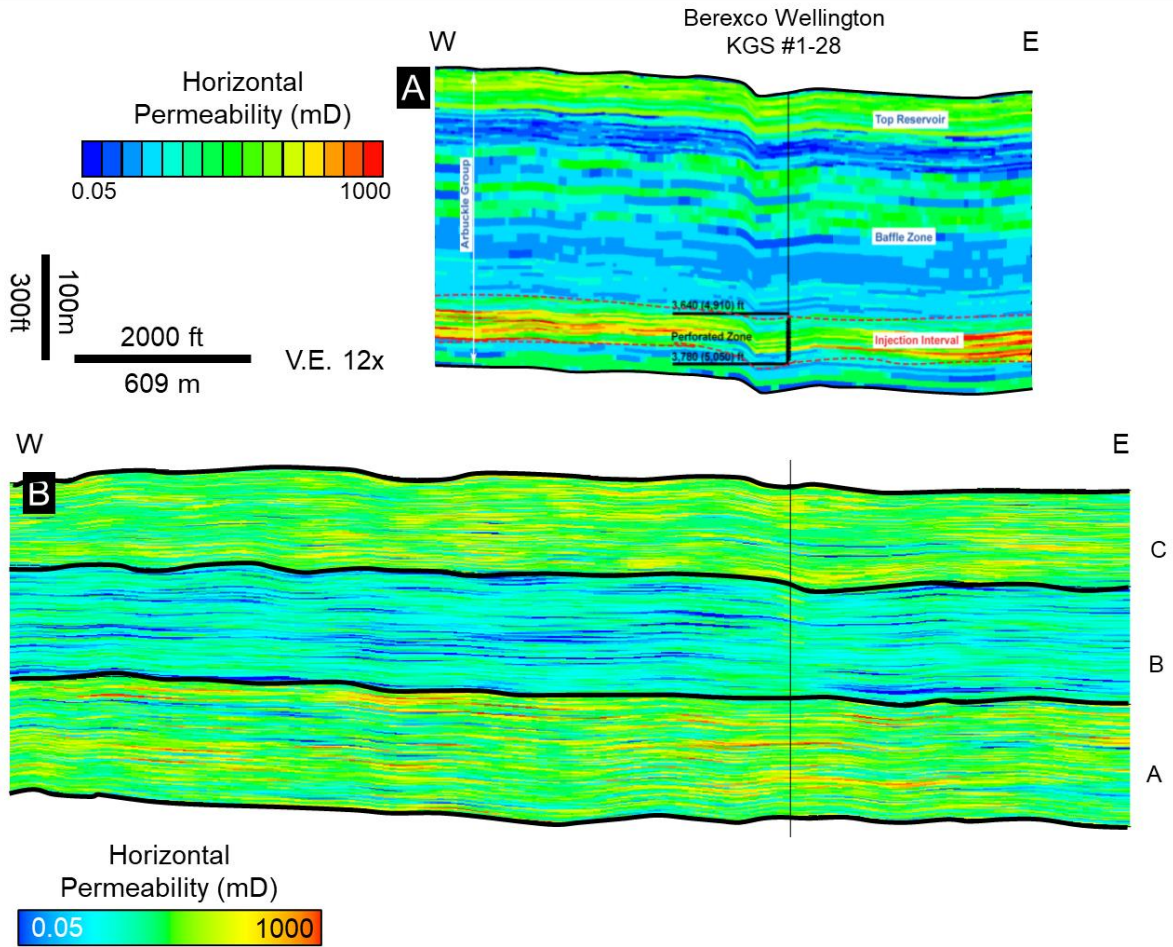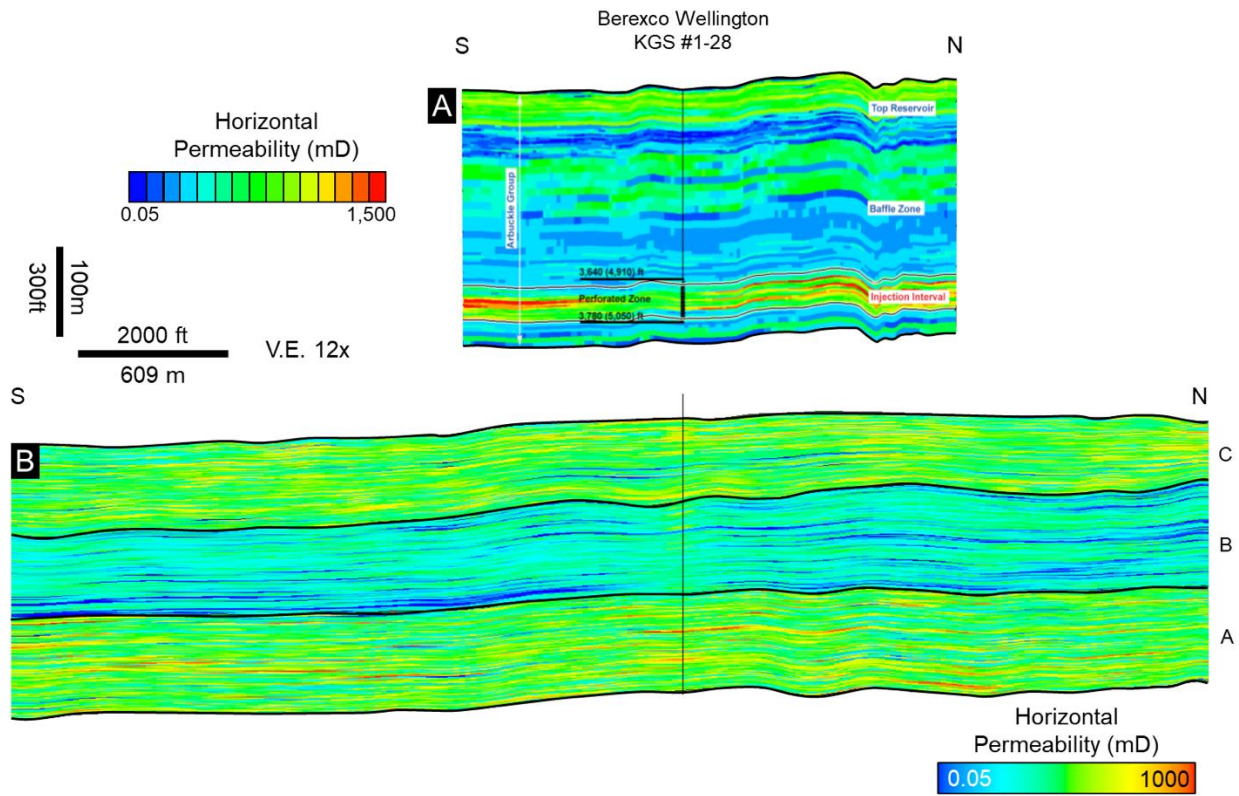
Figure 3.26: North-south cross sections transecting through the Berexco Wellington KGS #1-28 Well showing the comparison of horizontal permeability models created by A) Watney and Rush (2012) and B) this study.

Chapter 3 Tables

Parameters	Low	Most likely	High
Porosity (fraction)	0.045	0.065	0.1
Area	2.90E+08 ft^2 2.69E+07 m^2	2.90E+08 ft^2 2.69E+07 m^2	2.90E+08 ft^2 2.69E+07m^2
Gross thickness	337.9 ft 103 m	315 ft 107 m	360.8 ft 110 m
CO2 Density (kg/m^3)	547	547	547
Efficiency Factor	0.64	2.2	5.5
Bulk Volume	9.78E+10 ft^3 2.77E+09 m^3	1.02E+11ft^3 2.88E+09 m^3	1.02E+11 ft^3 2.96E+09 m^3
Pore Volume	4.40E+09 ft^3 1.25E+08 m^3	6.61E+09 ft^3 1.87E+08 m^3	1.04E+10 ft^3 2.96E+08 m^3

Table 3.1: Summary of the values used for the theoretical CO_2 storage capacity calculation for the Arbuckle zone A.

Parameters	Low	Most likely	High
Porosity (fraction)	0.038	0.06	0.09
Area	2.90E+08 ft^2 2.69E+07 m^2	2.90E+08 ft^2 2.69E+07 m^2	2.90E+08 ft^2 2.69E+07m^2
Gross thickness	893 ft 268 m	915 ft 279 m	1017 ft 310 m
CO2 Density (kg/m^3)	547	547	547
Efficiency Factor	0.64	2.2	5.5
Bulk Volume	9.78E+10 ft^3 2.77E+09 m^3	1.02E+11ft^3 2.88E+09 m^3	1.02E+11 ft^3 2.96E+09 m^3
Pore Volume	4.40E+09 ft^3 1.25E+08 m^3	6.61E+09 ft^3 1.87E+08 m^3	1.04E+10 ft^3 2.96E+08 m^3
CO2 Storage Capacity (Mt)	0.9	5.4	22.5

Table 3.2: Summary of the values used for the theoretical CO_2 storage capacity calculation for the entire Arbuckle Group in the study area.

General Conclusions

In this dissertation, I studied the combination of quantitative seismic interpretation methods and supervised machine learning approaches to create seismic-scale distributions of subsurface rock properties. I also applied seismic-constrained reservoir modeling workflows to combine seismic-scale property trends with well log and core data to create detailed subsurface models. In the first chapter, I showed that the combination of supervised Bayesian classifier and the Probabilistic Neural Network (PNN) methods showed the regional reflux dolomitization, and corresponding reservoir quality in the Clearfork and Wichita formations in the Midland Basin can be mapped on seismic scale with sparse well control. My results agreed with the regional dolomitization model, in which the porosity increases from the shelf to the slope concomitant with the decreasing dolomitization on the periplatform responding to variations in sea level.

In Chapter 2, I utilized the supervised random forest classification method and integrated core-derived petrophysics-based rock types (or petrofacies) information with the seismic data to investigate seismic-scale CO_2 injectivity and storage potential of the Arbuckle Group in Wellington Field in southern Kansas. Seismic-scale 3D petrofacies analysis provided a heterogeneous distribution indicating a corresponding fluid flow characteristics within the study area. Results also showed that the lower portion of the Arbuckle group is dominated mainly by permeable facies with potentially higher injectivity and storage potential, while the middle Arbuckle is primarily made up of tight facies that show baffle-like properties.

In Chapter 3, I applied seismic-constrained modeling and simulation methods that integrate seismic-based facies and petrophysical property trends with well-log and core data to model

170

stratigraphic and spatial variability of petrofacies and petrophysical properties to further investigate the Arbuckle group for CO_2 injectivity and storage potential. For this workflow, I used the 3D petrofacies volume and individual probability volumes that I created in Chapter 2 to further constrain my reservoir models. Results demonstrated that the integration of multi-scale sources could reveal the fine-scale variability of porosity, permeability, and fluid-flow characteristics. Dynamic simulation results illustrate the subsurface plume movement as a function of hydrogeological, petrophysical, and operational parameters.

This dissertation shows that the supervised machine learning methods can be used with traditional quantitative interpretation (QI) workflows to accurately map subsurface properties and corresponding reservoir quality and provide spatial information for a more robust geostatistical modeling, where the rocks are too complex for traditional seismic methods to work, and the well control is limited.